CENTRIFUGE MODELING OF STRAIN DISTRIBUTIONS IN ENERGY FOUNDATIONS

by

Melissa A. Stewart

B.C.E., University of Delaware, 2010

A thesis submitted to the

Faculty of the Graduate School of the

University of Colorado in partial fulfillment

Of the requirement for the degree of

Master of Science

Department of Civil, Environmental and Architectural Engineering

2012

This thesis entitled:

Centrifuge Modeling of Strain Distributions in Energy Foundations

written by Melissa A. Stewart

has been approved by the Department of Civil, Environmental, and Architectural Engineering

_____

Professor John S. McCartney (committee chair)

_____

Professor Dobroslav Znidarcic

_____

Professor Richard Regueiro

Date_____

The final copy of this thesis has been examined by the signatories, and we
Find that both the content and the form meet the acceptable presentation standards
Of scholarly work in the above mentioned discipline.

Stewart, Melissa A. (M.S. Civil Engineering, Department of Civil, Environmental, and Architectural Engineering)

Centrifuge Modeling of Strain Distributions in Energy Foundations

Thesis directed by Professor John S. McCartney

ABSTRACT

In the recent push for sustainable engineering design, integration of ground-source heat exchange systems into foundations (energy foundations) have emerged as an energy efficient solution to reduce the cost of heating and cooling systems for buildings. Although full-scale energy foundations have been used in several buildings throughout the world, quantification of the effects of temperature changes on their mechanical response has not be systematically investigated. The objective of this study is to evaluate the impact of the mechanical boundary conditions and cyclic heating and cooling on the thermo-mechanical response of energy foundations. The approach used in this study to reach the objectives is to evaluate the loading, heating and cooling of scale-model energy foundations within a soil layer in a geotechnical centrifuge. Centrifuge physical modeling facilitates the characterization of carefully controlled soil-foundation systems with dense instrumentation arrays, and permits parametric evaluations of variables which may affect the behavior of energy foundations.

The boundary conditions considered in this study are an "end-bearing" condition, where the tip (bottom) of the foundation is resting on a rigid base and a constant load is applied to the foundation head (top), and a "semi-floating" condition where the tip of the foundation is resting on a layer of soil and a constant load is applied to the foundation head. Both foundation boundary conditions were evaluated in a layer of unsaturated silt compacted around the model foundation. Instrumentation was embedded in the foundation as well as into the surrounding soil

mass to characterize soil-structure interaction and heat flow phenomena during heating and cooling cycles. Specifically, variables monitoring during testing include changes in axial strain and temperature in the foundation, movement of the foundation head, movement of the soil surface and changes in temperature and volumetric water content of the soil at different depths and radial locations.

The results obtained in this study agree well with strain distribution data collected from full-scale energy foundations. The results from this study will be useful for validation and calibration thermo-mechanical soil-structure interaction models. The effects of the foundation boundary conditions were substantial in the sense that the magnitude of thermal strains was larger for the end-bearing foundation than for the semi-floating foundation. In addition, the location of the maximum strain along the length of the foundation depended on the foundation boundary conditions. The maximum strain was located near the top of the foundation for the semi-floating foundation and near the base of the foundation for the end-bearing foundation. Heating and cooling cycles led to cumulative decreases in compressive strains in both foundations after cooling in each cycle. This was attributed to changes in soil stiffness due to thermally induced drying of the unsaturated soil surrounding the foundation.

ACKNOWLEDGEMENT

The author wishes to thank her advisor, Professor John Scott McCartney, for his guidance, assistance and seemingly endless positive attitude through the completion of this project. Special recognition is given to the members of the thesis committee: Professors Dobroslav Znidarcic and Richard Regueiro. In addition, a special thank you is offered to the many geotechnical graduate and undergraduate students who helped keep this project moving forward with their enthusiasm and tireless work ethic: Kyle Murphy, Joseph Goode, Jonathan (Tate) Fairbanks and Anna Casady. Funding from NSF grant CMMI 0928159 is greatly appreciated.

TABLE OF CONTENTS

1. Introduction 1

1.1 Overview of Energy Foundations 1

1.2 Objective 2

1.3 Approach 3

1.4 Scope of Study 4

2. Literature Review 5

2.1 Energy Foundations 5

2.2 Response of Energy Foundations: A Simplified Approach 7

2.3 Field Performance of Energy Foundations 10

3. Experimental Setup 16

3.1 Centrifuge Modeling of Energy Foundations 16

3.2 Geotechnical Centrifuge Facilities 17

3.3 Model Foundation Fabrication 18

3.4 Model Foundation Instrumentation 20

3.5 Heat Control Systems 24

3.6 Temperature Control in Foundations 27

3.7 Testing Frame and Container 28

3.8 Soil Instrumentation 30

4. Material Properties 35

4.1 Soil Properties 35

4.1.1 Summary 35

4.1.2 Geotechnical Characteristics 35

4.1.3 Mechanical Properties 37
4.1.4 Hydraulic Properties 38
4.1.5 Thermal Properties 39
4.2 Foundation Properties 40
4.2.1 Summary 40
4.2.2 Mechanical Properties 41
4.2.3 Thermal Properties 43
5. Experimental Procedures 49
5.1 Specimen Preparation 49
5.1.1 Specimen Preparation 49
5.1.2 Installation of Instrumentation 52
5.2 Experimental Procedures 55
6. Experimental Results 58
6.1 Calibration 58
6.1.1 Thermocouple Calibration 58
6.1.2 Strain Gage Calibration 58
6.2 End-bearing Foundation Data 60
6.2.1 Temperature Data 60
6.2.2 Dielectric Sensors (Temperature and Vol. Water Content) 65
6.2.3 Load and LVDT Response 66
6.2.4 Strain Gages 68
6.3 Semi-floating Foundation 72
6.3.1 Temperature Data 73

6.3.2 Dielectric Sensors (Temperature and Vol. Water Content) 75

6.3.3 Load and LVDT Response 77

6.3.4 Strain Gages 79

7. Analysis 82

7.1 Thermal Strains for Different Boundary Conditions 82

7.2 Cyclic Heating and Cooling Effects 85

8. Conclusions 90

References 92

Appendix A 96

LIST OF TABLES

Table 2.1: Thermo-mechanical loading data for full-scale energy foundation tests 14

Table 3.1: Centrifuge scaling relationships (Ko 1988) 17

Table 3.2: Model-scale depths from top of foundation of strain gages and thermocouples in the end-bearing (length of 533.4 mm) and semi-floating (length of 381.0 mm) model foundations 24

Table 3.3: Locations of EC-TM® dielectric sensors in the tests on end-bearing and semi-floating model foundations 31

Table 4.1: Atterberg limits for Bonny silt 35

Table 4.2: Grain size distribution data for Bonny Silt 36

Table 4.3: Mechanical correction factors for strain gages embedded in end-bearing model based on 1g loading test results 43

Table 4.4: Thermal correction factors for strain gages embedded in the foundation 47

Table 4.5: Calculation of thermal conductivity using the line source equation 48

Table 5.1: As-built compaction conditions for soil specimens used to evaluate the effect of end-bearing and semi-floating foundation test 51

Table 5.2: Locations of thermocouples in the thermocouple profile probes for the end-bearing foundation test 54

Table 5.3: Radial locations of LVDTs for the tests on the end-bearing and semi-floating foundations 54

Table 6.1: Thermal output coefficients for the strain gages used in this study 59

Table 6.2: Timing of each of the phases in the test on the end-bearing foundation 60

Table 6.3: Timing of each of the phases in the test on the semi-floating foundation 73

LIST OF FIGURES

Figure 2.1: Photograph of U-tube heat exchangers attached to the reinforcement cage of a drilled-shaft energy foundation 6

Figure 2.2: Schematic of simplified representation of thermo-mechanical response of energy foundations (Bourne-Webb et al. 2009) 8

Figure 2.3: Plot of heat load applied to an energy foundation system shown with COP value throughout duration of test 10

Figure 2.4: Thermal strains in reinforced concrete as a function of temperature (Choi and Chen 2005; Bourne-Webb et al. 2009) 12

Figure 2.5: Strain profiles in energy foundations measured by Laloui and Nuth (2006) and Bourne-Webb et al. (2009): (a) Heating; (b) Cooling 14

Figure 2.6: Temperature-induced axial and radial displacements in an energy foundation (Laloui et al. 2006) 15

Figure 3.1 Figure depicting 400 g-ton geotechnical centrifuge being used at the University of Colorado Boulder: (a) Picture; (b) Schematic 18

Figure 3.2: Photograph of completed foundation; heat exchanger tubes and cables from embedded instrumentation are seen at top 20

Figure 3.3: Schematic of the end-bearing and semi-floating energy foundations showing the relative locations of embedded instrumentation 21

Figure 3.4: Picture showing instrumentation attached to the inside of the reinforcement cage 21

Figure 3.5: Typical linear pattern stress analysis strain gage 23

Figure 3.6: Strain gage attached to steel tab and covered with epoxy 23

Figure 3.7: Julabo F25-ME heat pump 25

Figure 3.8: Taco Model 009-F5 high velocity centrifugal pump (cartridge circulator) used in-series with Julabo heat pump to increase flow through system 26

Figure 3.9: Schematic of overall temperature control system, including heat pump, auxiliary pump and fluid transition into experimental setup 27

Figure 3.10: Loading frame for the 400 g-ton geotechnical centrifuge 28

Figure 3.11: Brushed DC motor used to apply building load to model foundation 29

Figure 3.12: Soil container within the load frame 30
Figure 3.13: Photograph of an EC-TM® dielectric sensor being placed during specimen compaction 31
Figure 3.14: Schematic showing approximate locations of instrumentation 32
Figure 3.15: Photograph of a thermocouple profile probe 33
Figure 3.16: Photograph of LVDT mounting bracket attached with C-clamps to container before testing, as well as an inset photograph of a typical LVDT used in testing 34
Figure 4.1: Grain size distribution curve for Bonny silt 36
Figure 4.2: Compaction curves for Bonny silt obtained using both standard and modified Proctor compaction efforts, plotted with the zero air void (ZAV) line. 37
Figure 4.3: Effective stress paths for compacted Bonny silt plotted for initial consolidation effective stresses of 100, 200 and 350 kPa 37
Figure 4.4: Changes in small-strain shear modulus with mean effective stress 38
Figure 4.5: Hydraulic conductivity as a function of void ratio for a variety of tests performed on Bonny silt 39
Figure 4.6: SWRC for Bonny silt specimens having an initial void ratio of 0.69 under a range of net stresses 39
Figure 4.7: Relationship between thermal conductivity and void ratio for Bonny silt 40
Figure 4.8: Mechanical characterization results: (a) Load, LVDT and Motor position; (b) Motor position strain with strain gage readings 42
Figure 4.9: Stress vs. strain diagram for model energy foundation indicating a total elastic modulus for foundation system of 7.17 GPa: (a) Uncorrected; (b) Corrected 42
Figure 4.10: Response of strain gage attached to steel tab during heating (positive strain implies compression): (a) Time series; (b) Temperature vs. strain 43
Figure 4.11: Time series of inlet, outlet and ambient temperatures during the 1g test 44
Figure 4.12: Time series of temperatures measured by thermocouples embedded in the model foundation during the 1g heating test 45
Figure 4.13: External measurements during heating for end-bearing model foundation under axial mechanical stress of 439 kPa: (a) Free theory) and restrained (measured) thermal axial strains; (b) Thermal and mechanical stresses 46

Figure 4.14: Strain measured during the 1g heating test: (a) Original; (b) Corrected 46
Figure 5.1: Compaction curves for Bonny Silt for standard and modified Proctor compaction, including the as-built compaction conditions for the soil in the tests on the end-bearing and semi-floating foundations 51
Figure 5.2: Photographic series depicting soil compaction procedures: (a) end-bearing foundation being centered pre-compaction; (b) placement of water content sensor during compaction (inset: dielectric sensor); (c) fourth loose lift distributed around centered foundation pre-compaction 52
Figure 5.3: Schematic of the 5 dielectric sensors arranged in a vertical array (1-2-3) and a horizontal array (3-4-5) 53
Figure 5.4: Schematic showing the approximate location of different instruments 55
Figure 5.5: Schematic of testing procedures for the tests on the model foundations 56
Figure 6.1: Thermal output curve specific to the strain gages used in this study 59
Figure 6.2: Inlet, outlet and ambient temperature data from end-bearing foundation test: (a) Entire testing sequence; (b) During centrifugation 61
Figure 6.3: Temperature data from thermocouples embedded within the end-bearing foundation: (a) Entire testing sequence; (b) During centrifugation 62
Figure 6.4: Temperature data in the soil at various radial locations from the end-bearing foundation: (a) 76 mm; (b) 140 mm; (c) 216 mm; (d) 292 mm 63
Figure 6.5: Temperature profiles for end-bearing foundation at different testing times 64
Figure 6.6: Temperature profiles in the soil at different radial locations from the end-bearing foundation: (a) 76 mm; (b) 140 mm; (c) 216 mm; (d) 292 mm 64
Figure 6.7: Data from the EC-TM dielectric sensors embedded in the soil layer for the end-bearing foundation test: (a) Volumetric water content varation from the sensors in the vertical array; (b) Temperature variation from the sensors in the vertical array; (c) Volumetric water content varation from the sensors in the horizontal array; (d) Temperature variation from the sensors in the horizontal array 66
Figure 6.8: Time series of temperature change and mechanical loading for the end-bearing foundation during centrifugation 67
Figure 6.9: Time series of settlement for various radial distances from foundation during centrifugation 67

Figure 6.10: Prototype-scale time series of vertical position inferred from the LVDT on the foundation head with: (a) Axial load; (b) Temperature at center of foundation 68
Figure 6.11: Comparison of motor position with LVDT measurement 68
Figure 6.12: All strain gage data for the pair of strain gages embedded at each depth: (a) 508 4m; (b) 387.9 mm; (c) 266.7 mm; (d) 146 mm; (e) 25.4 mm (Note: "t" designates that a thermocouple is next to the strain gage) 70
Figure 6.13: Strain data for end-bearing foundation collected from strain gauges embedded in model foundation (dimensions in prototype scale): (a) Raw measurements (tensile = positive); (b) Corrected thermo-mechanical strains; (c) Corrected thermal strains 72
Figure 6.14: Inlet, outlet and ambient temperature data from semi-floating foundation test: (a) Entire testing sequence; (b) During centrifugation 74
Figure 6.15: Temperature data for end-bearing foundation collected from thermocouples embedded in model: (a) Entire testing sequence; (b) During centrifugation 74
Figure 6.16: Temperature profiles for semi-floating foundation collected from thermocouples embedded in model foundation 75
Figure 6.17: Data from the EC-TM dielectric sensors embedded in the soil layer for the semi-floating foundation test: (a) Volumetric water content varation from the sensors in the vertical array; (b) Temperature variation from the sensors in the vertical array; (c) Volumetric water content varation from the sensors in the horizontal array; (d) Temperature variation from the sensors in the horizontal array 76
Figure 6.18: Time series of thermal and mechanical loading for semi-floating foundation: (a) Entire testing sequence; (b) During centrifugation 77
Figure 6.19: Time series of settlement for various radial distances from semi-floating foundation during centrifugation 78
Figure 6.20: Time series of vertical displacement from the LVDT on the semi-floating foundation head: (a) With mechanical stress; (b) With temperature change 79

Figure 6.21: All strain gage data for the pair of strain gages embedded at each depth: (a) 355.6 mm; (b) 273.1 mm; (c) 190.5 mm; (d) 108.0 mm; (e) 25.4 mm (Note: "t" designates that a thermocouple is next to the strain gage) 80

Figure 6.22: Strain data for semi-floating foundation collected from strain gages embedded in model foundation: (a) Uncorrected; (b) Corrected; (c) Corrected thermal strains 82

Figure 7.1: Time-series for energy foundations with different boundary conditions: (a) thermal strains for end-bearing foundation; (b) thermal strains for the semi-floating foundation; (c) temperature change and mechanical stress for the end-bearing foundation; (d) temperature change and mechanical stress for the semi-floating foundation; (e) head displacement for the end-bearing foundation; (f) head displacement for the semi-floating foundation 83

Figure 7.2: Thermal stress and strain profiles at different temperature increments (dimensions in prototype scale): (a) Strain in end-bearing foundation; (a) Stress in end-bearing foundation; (c) Strain in semi-floating foundation; (d) Stress in semi-floating foundation 85

Figure 7.3: Cyclic heating and cooling effects: (a) Change in thermal strains in the end-bearing foundation; (b) Change in thermal strains in the semi-floating foundation; (c) Change in axial displacement in the end-bearing foundation; (d) Change in axial displacement in the semi-floating foundation 87

Figure 7.4: Thermally driven water content changes observed using dielectric sensors installed at varying depths (model scale): (a) End-bearing foundation; (b) Semi-floating foundation 88

Figure 7.5: Thermally driven water flow collected from dielectric sensors at varying radial distances from foundations: (a) End-bearing foundation; (b) Semi-floating foundation 89

CHAPTER I
Introduction

1.1 Overview of Energy Foundations

Commercial and residential buildings are currently a major consumer of energy in the United States. The sum of the energy consumption of commercial and residential buildings is equal to 71% of the electricity and 53% of the natural gas in the United States (EIA 2008). Out of the different sources of energy demand by buildings, the heating and cooling systems account for 20% of the primary energy consumed by buildings, which is equal to 39% of the primary energy consumption in the United States. This high amount of energy usage by building heating and cooling systems has driven a recent push to develop and implement energy-efficient technologies to reduce the energy demand of these systems.

One technology that has been proven to be a feasible method for lowering the energy cost of indoor climate control is ground-source heat exchange (Hughes 2008). This technology uses the ground as a heat source or sink from which heat can be extracted or dumped, respectively, to maintain a building a desired temperature. At depths of approximately 3 meters below the ground surface, the ground temperature remains at a constant temperature of between 10 and 18 °C in most regions of the United States, which corresponds to the mean annual air temperature (in the absence of an upward geothermal gradient). The natural temperature regulation is employed in conventional ground-source heat exchange systems as a heat source/sink for building heating and cooling systems. Conventional ground source heat pumps exchange heat with the ground via heat exchange loops (vertical or horizontal) installed in direct contact with the ground. The primary cost of these systems is associated with earthwork (drilling small-diameter boreholes or digging trenches) and labor associated with placing the loops into

the ground. The up-front installation cost associated with drilling may be prohibitively high for a building developer, especially considering that the heat pump unit within the building may have a similar cost to a conventional heating and cooling system. The additional up-front cost of a ground-source heat exchange system has led to a lack of their widespread implementation in the United States (Hughes 2008)

The up-front cost of ground source heat exchangers can be minimized by installing heat exchanger tubing into holes already being drilled for the deep foundations of buildings (Brandl 2006). There has been a recent trend around the world to modify drilled shaft foundations to function as heat exchangers in an effort to make ground-source heat pumps a more financially feasible option for a wider variety of projects (Bourne-Webb et al. 2009, Böennec 2008). When building foundations are modified to include heat exchange loops they are referred to as "energy foundations." Energy foundations can be any type of foundation (deep, shallow, drilled) and, when used in this way, become an integral part of the building's heating and cooling system while still serving their original purpose of providing mechanical support to the building (Ooka et al. 2007). There are several installations of energy foundations in Europe and Japan, but there are currently only two fully operational energy foundation systems in the United states: the Art House in Seattle, WA, designed and constructed by Kulchin Drilling (Redmond Reporter 2010) and at the Denver Housing Authority Senior Living Center in Denver, CO (Zitz and McCartney 2011).

1.2 Objective

The objective of this study is to quantify strain distributions in energy foundations due to mechanical loading and temperature changes, and to use these strain distributions to understand the roles of foundation boundary conditions and heating and cooling cycles. The foundation boundary conditions of interest are the axial restraints at the tip and head of the foundation.

Although some studies have been performed to evaluate the strain distributions in full-scale energy foundations during combined thermo-mechanical loading (Laloui et al. 2006; Bourne-Webb et al. 2009), it was not possible to thoroughly evaluate the effects of foundation boundary conditions or cyclic heating and cooling. Their foundations involved changes in foundation geometry with depth and multiple soil layers surrounding the foundation with uncertain rigidity of the material at the toe of the foundations. Because of time constraints in the full scale tests, the impact of cyclic heating and cooling was not assessed, which is important to understand the long-term performance of energy foundations under seasonal and annual fluctuations in the thermal demand. Although full-scale testing is the best representation of the behavior of real energy foundations, centrifuge modeling permits better control (or knowledge) of the material properties of the foundation and soil , which is useful to obtain clear insight into the impact of soil behavior and soil-structure interaction on the strain distributions within energy foundations.

1.3 Approach

The approach used in this study is to evaluate the strain and temperature distributions in small-scale energy foundations during mechanical loading and controlled temperature changes in a soil layer within a geotechnical centrifuge. Specifically, two scale-model energy foundations were instrumented with embedded strain gages and thermocouples to measure distributions in strain and temperature during heating and cooling cycles. The centrifuge modeling approach permits careful control of the boundary conditions, material properties, and imposed temperature patterns in a soil-foundation system. Further, it permits the use of a dense instrumentation array to capture the thermo-mechanical effects in the foundation as well as the thermo-hydro-mechanical effects in the surrounding soil. Although the principle of scaling in the centrifuge does not apply to the flow of temperature in the energy foundation and surrounding soils, the

thermally-induced stress and strain distributions are expected to scale according to established relationships. Two different boundary conditions are presented in this study. The tip of the first foundation is resting on a rigid base and is referred to as an "end-bearing foundation," while the tip of the second foundation is resting on a soil layer and is referred to as "semi-floating foundation."

1.4 Scope of Study

This thesis is organized as follows: Chapter 2 provides a review of previous literature related to this topic, including thermo-mechanical response of previously tested full-scale energy foundation. Chapter 3 presents the experimental setup and instrumentation utilized for this research. The material properties of the soil and model foundations are presented in Chapter 4. Testing procedures are outlined in Chapter 5. Chapter 6 contains the results obtained from testing and the analysis of this data is presented in Chapter 7.

CHAPTER II
Literature Review

2.1 Energy Foundations

The use of building foundations as ground-source heat exchangers has been evaluated since the early 2000's. Ennigkeit and Katzenbach (2001) performed a series of laboratory physical modeling tests to evaluate heat flow around energy foundations, and developed simple analytical equations to use to estimate the temperature distribution around the foundations. Since this early study, there has been a significant amount of research in this area, involving element-scale tests on soil and concrete (Baldi et al. 1988; Cekeravac and Laloui 2004), development of thermo-hydro-mechanical models (Hueckel and Borsetto 1990; Cui et al. 2000; Laloui and Cekeravac 2001), and full-scale foundation tests to evaluate thermal response (Ooka et al. 2007; Adam and Markiewicz 2009; Wood et al. 2009) and thermo-mechanical response (Laloui et al. 2006, 2007; Bourne-Webb et al. 2009; Zitz and McCartney 2011). This study is part of a larger effort at the University of Colorado Boulder involving thermal modeling (Kaltreider 2011; Rouissi et al. 2012), element-scale testing (Coccia and McCartney 2012; Vega et al. 2012), and centrifuge modeling of soil-structure interaction (McCartney et al. 2010; McCartney and Rosenberg 2011; Stewart et al. 2012), and thermo-mechanical (Plaseied 2012) and thermo-poro-mechanical analysis (Regueiro et al. 2012).

It is possible to incorporate heat exchangers into many types of foundations (shallow vs. deep, driven vs. drilled) or subsurface structures (retaining structures, ground anchors, tunnel linings, etc.). The types of foundations being modeled in this study are drilled shaft foundations, and are referred in general as "energy foundations." Drilled shaft foundations differ from driven foundations in that the primary resistance to axial load comes from end bearing, although side

shear resistance still plays an important role in their performance (O'Neill and Reese 1986). An energy foundation is similar to a conventional drilled shaft except that closed-loop polyethylene heat exchanger tubing is attached to the inside of the reinforcement cage, as shown in Figure 2.1. The heat exchanger tubing is typically bent into a "U" shape so that fluid can be circulated from the top of the foundation, down to the bottom, and back up to the top of the foundation. Accordingly, the heat exchanger tubes are conventionally referred to as "U-tubes."

Figure 2.1: Photograph of U-tube heat exchangers attached to the reinforcement cage of a drilled-shaft energy foundation

A drilled shaft can be converted to an energy foundation without significant additional cost beyond the costs of drilling and placing the reinforcement cage. These costs include the materials for the U-tubes, the additional labor needed to attach the U-tubes to the reinforcement cage and the costs associated with testing and quality assurance of the heat exchanger system (Brandl 2006). Despite these additional costs, the financial gain from installing the heat exchangers is that they can be used to improve the efficiency of heat pump systems used to provide heating and cooling for buildings. Further by installing the heat exchanger into the foundation instead of into vertical boreholes like conventional ground-source heat pump (GSHP) systems, the additional earthwork costs associated with drilling boreholes can be avoided.

An issue which has been identified in the literature with energy foundations is the potential for thermal expansion and contraction during heating and cooling, or the associated changes in stress for different confining stresses (Laloui et al. 2006; Bourne-Webb et al. 2009). However, these studies have been based on field measurements, which are often affected by uncertainties in the soil stratigraphy. Centrifuge modeling was found to be a useful approach to characterize thermal soil-structure interaction for energy foundations in uniform soil layers (Stewart and McCartney 2012). An additional issue which has not been evaluated in previous studies is the potential for permanent changes in the mechanical response over a series of thermal cycles. Although energy foundation systems are ideally installed in rigid systems which behave in a thermo-elastic manner, it is possible that the flow processes involved with cyclic heating and cooling may lead to build-up of stress in the foundation (i.e., the soil surrounding the foundation is still heating while the foundation is being cooled, and vice-versa).

2.2 Thermo-mechanical Response of Energy Foundations: Simplified Explanation

Although soil-structure interaction analyses have been developed to consider the thermo-mechanical stresses in foundations for different boundary conditions (Knellwolf et al. 2011; Plaseied 2012; Regueiro et al. 2012), there is still a lack of validation data. To develop a simple understanding of thermo-mechanical soil-structure interaction, it is best to evaluate a simple case. Bourne-Webb et al. (2009) proposed a simplified model to describe the expected thermo-mechanical response of energy foundations with floating boundary conditions (no end bearing and resistance mobilized only due to side shear). In this simplified explanation Bourne-Webb et al. (2009) made several key assumptions. The first is that the side shear resistance along the length of the foundation is constant. Although this assumption is valid for some soil profiles under undrained loading conditions, it may not be relevant to drained loading conditions

encountered during heating and cooling of energy foundations. A second assumption is that the change in temperature in the foundation is constant with depth. The third assumption is that the foundation is offers no end bearing resistance and the head is free to move, which means that axial stresses will only be mobilized in the foundation due to the mobilized side shear resistance along the length of the foundation. A schematic of the expected thermo-mechanical response of an energy foundation with floating boundary conditions is shown in Figure 2.2.

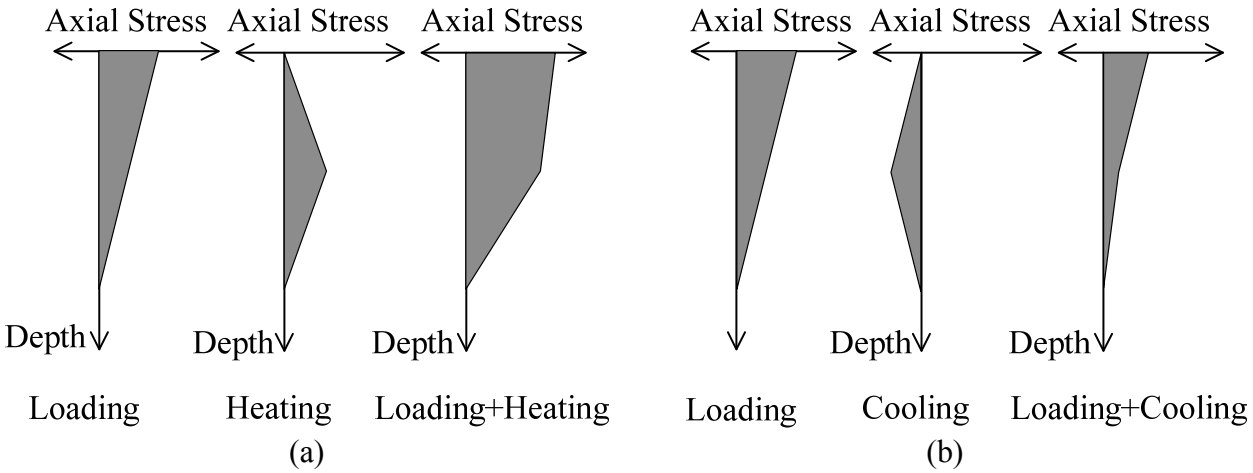

Figure 2.2: Schematic of simplified representation of thermo-mechanical response of energy foundations (Bourne-Webb et al. 2009)

Regardless of the temperature change in the foundation, a mechanical load applied to the head of the foundation will lead to compressive stresses in the foundation, with the largest stress near the head of the foundation, decreasing with depth as the side shear resistance is mobilized. The behavior during of the foundation during a heating cycle is shown in Figure 2.2(a). When the foundation is heated, it expands volumetrically. Not only will the side shear resistance mobilize in the opposite direction of foundation expansion, but the maximum side shear resistance may increase if the radial normal stress along the length of the foundation increases due to its radial expansion (McCartney and Rosenberg 2011). The resistance of the soil to axial movement of the foundation will cause additional compressive internal stresses to develop

beyond those developed during mechanical loading. The largest thermal compressive stresses will develop at the null point of the foundation, which is defined as the point where the foundation does not move upward or downward, with the foundation expanding around it on either side. The null point will occur at the center of the foundation for a floating foundation. The mechanical and thermal stresses in the foundation are additive and result in a stress profile with largest stresses near the head of the foundation. If the foundation begins to provide end bearing resistance, the null point will move downwards (Knellwolf et al. 2011; Plaseied 2012).

A schematic of the expected behavior during cooling for a floating foundation is shown in Figure 2.2(b). As the foundation cools, it tends to contract about the null point at the center of the floating foundation. As side shear resistance is mobilized it acts in the opposite direction. Depending on the magnitude of mechanical loading, it is possible for tensile axial strains to develop in the foundation during cooling.

The trends predicted by this simplified explanation of thermo-mechanical effects in energy foundations are for boundary conditions which are rarely encountered in drilled shaft foundations. Most drilled shafts are designed to be end-bearing foundations, where side shear resistance is often only a fraction of the total axial capacity. Accordingly, one of the goals of this study is to develop a centrifuge physical modeling approach to evaluate the changes in axial strain during thermo-mechanical loading for more realistic boundary conditions (end-bearing and semi-floating conditions). Semi-floating boundary conditions involve those where the material at the toe of the foundation may experience elasto-plastic deformations during loading (soil as opposed to rock).

2.3 Field Performance of Energy Foundations

The ability of energy foundation systems to provide a sustainable heat exchange solution for heating and cooling systems has been evaluated in several full-scale studies in different soil profiles (Ooka et al. 2007, Adam and Markiewicz 2009, Wood et al. 2009). The long-term performance of GSHP systems is characterized by establishing the ratio of thermal energy delivered by the system to the electrical input needed to operate the system, which is called the coefficient of performance (COP). A traditional GSHP system typically has a COP value of greater than 3, where an air-source heat pump system typically has a COP value of between 1 and 3 (Brandl 2006). Wood et al. (2009) performed a test where 21 10-meter energy foundations were fabricated and the system was subjected to the heat load of a typical 2-story residential building. The tests were continued for two different heating loads over an entire heating season. The total heating load applied is plotted with the COP for this testing and shown in Figure 2.3. The COP remained relatively consistent through the duration of the test and was equal to approximately 3.75, which is acceptable for heat pump systems.

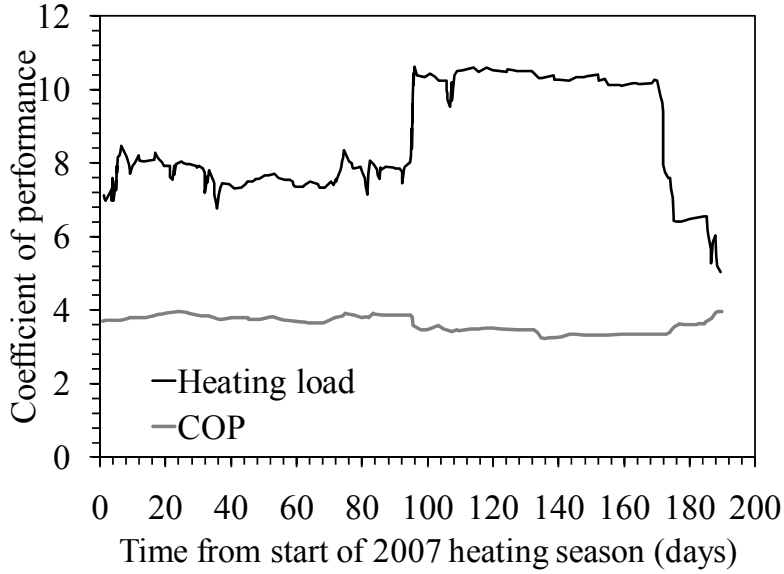

Figure 2.3: Plot of heat load applied to an energy foundation system shown with COP value throughout the duration of a test

In general, the thermal response and efficiency of energy foundations depends on many different factors. In order to implement the technology the designer must first look at the feasibility of the project. If a small building (few foundations utilized for heat exchange) was constructed in a climate that is colder or warmer than average the system would have a difficultly keeping up with the demand. In addition, introducing temperature fluctuations to the ground can change the previously constant ground temperatures. For example, if a GSHP system were installed in a region where the system would be constantly used as a heat source or constantly used a heat sink, the ground temperature could be raised or lowered to be closer to that of the ambient temperature and the system would become less efficient. Typically, energy foundations are designed to accommodate a fraction of the base heating or cooling load of a building to avoid overcooling or overheating of the ground. Although a conventional heating or cooling system may be necessary as a backup, the usage time for this system would be reduced significantly.

In addition to accounting for thermal response of energy foundations, design should also account for the thermo-mechanical response of the systems to ensure that deformations and stresses are within reasonable limits. Changes in temperature can induce additional stresses and strains in the foundation and some of these effects may change over multiple heating cycles.

The thermo-mechanical response of reinforced concrete has been quantified by Bourne-Webb et al. (2009) and Choi and Chen (2005) The results of these studies are plotted together in Figure 2.4 and indicate agreement between the data sets after correction of the data of Bourne-Webb et al. (2009) for errors associated with the fiber-optic cable measurement technique. The coefficient of thermal expansion in these two studies was found to vary between 8.5×10^{-6} and 9×10^{-6} m/m °C. This amount of thermal free expansion may be enough to cause either noticeable deformations or changes in stress in energy foundations.

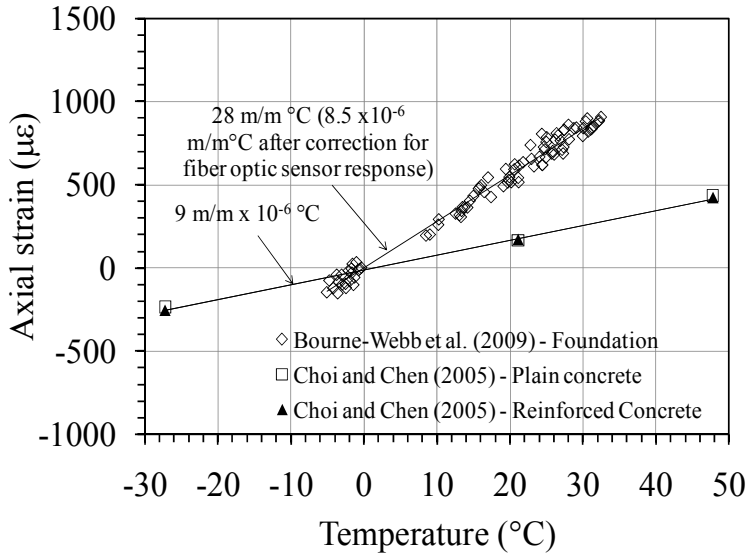

Figure 2.4: Thermal strains in reinforced concrete as a function of temperature (Choi and Chen, 2005; Bourne-Webb et al. 2009)

Laloui et al. (2006) and Laloui and Nuth (2006) describe the thermal and mechanical testing on a full-scale energy foundation in Switzerland. This field study was complimented by another performed by Bourne-Webb et al. (2009) on a full-scale energy foundation in England. Laloui and Nuth (2006) evaluated a drilled shaft foundation having a length of 25.8 meters and a diameter of 0.99 meters. The upper 12 meters of soil included alluvial deposits with the remainder of the foundation sitting in glacial moraine material. Bourne-Webb et al. (2009) evaluated a drilled shaft foundation having a length of 22.5 meters and a diameter of 0.56 meters. The first 4 meters of the soil was a frictionless fill with the remaining 18.5 meters of the foundation in London clay.

The strain profiles with depth for the foundations from both studies are shown in Figures 2.5(a) and 2.5(b). The sign convention used for this study was that a negative strain represented compressive strains. The mechanical behavior of the foundations was as expected, as a mechanical load caused compressive strain to develop throughout the foundation, decreasing with depth. An exception to the expected behavior occurred in the upper 5 meters of the

foundation which was likely due to both eccentric loading and the fact that the foundation diameter was larger in the uppermost 5 m (Bourne-Webb et al. 2009). During heating, the strain gages in the Bourne-Webb et al. (2009) foundation were found to indicate additional compressive strains in the foundation. Although it is expected that the stress in the foundation would increase during heating, the strain gages were expected to indicate expansion of the foundation during heating. This may indicate that the embedded strain gages actually reveal the stress distribution in the foundation. Subsequent cooling caused a reduction in strains throughout the foundation. Tensile strains were observed near the foundation tip at the end of the cooling cycle in the foundation of Bourne-Webb et al. (2009) because the thermal contraction during cooling was greater in magnitude than the compressive mechanical strains applied to the head of the foundation. The lack of change at the tip of the foundation of Bourne-Webb et al. (2009) is due to the fact that end resistance was not fully mobilized during mechanical loading of during heating. Comparison of the strain profiles during heating and cooling observed by Laloui and Nuth (2006) indicates a uniform shift in the strain profile with depth. This may indicate that tip resistance was mobilized during heating of the foundation and that the foundation had relatively stiff upper and lower boundary conditions.

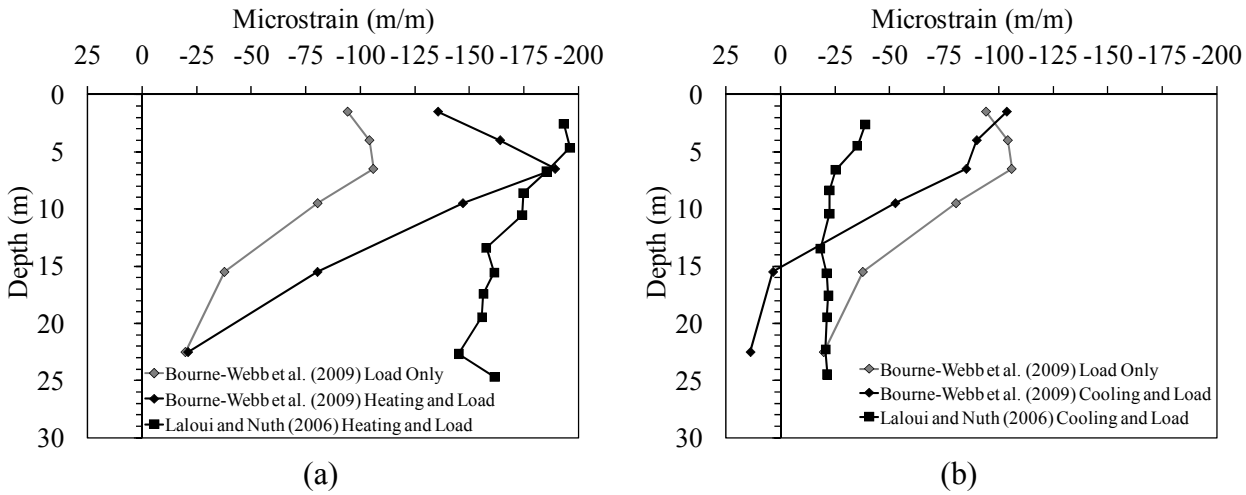

Figure 2.5: Strain profiles in energy foundations measured by Laloui and Nuth (2006) and Bourne-Webb et al. (2009): (a) Heating; (b) Cooling
(Note: Negative strains are defined as compressive)

The thermo-mechanical boundary conditions for the two field studies are presented in Table 2.1. One difference to note between the two studies is that Bourne-Webb et al. (2009) first cooled the foundation, and then heated it, while Laloui and Nuth (2006) heated their foundation first. It is unclear what kind of effect this might have had on the results as not enough data was available to assess the impact of cyclic heating and cooling. It is possible that plastic thermal strains may occur during the first instance of heating or cooling, which would affect the response during subsequent cooling or heating, respectively.

Table 2.1: Thermo-mechanical loading data for full-scale energy foundation tests

	Load (kN)	Heating Temperature (°C)	Cooling Temperature (°C)
Laloui and Nuth (2006)	2140	21 (above ground temperature)	3 (above ground temperature)
Bourne-Webb et al. (2009)	1200	40	-6

In addition to strains developing in the foundation, another issue that needs to be addressed is movement of the foundation top during cyclic heat exchange. A heave of almost 4 mm was

measured at the head of the foundation by Laloui et al. (2006) during heating of the foundation to 21°C, as shown in Figure 2.5. Although most of the heave was recovered during cooling, approximately 1 mm of permanent upward vertical displacement was observed at the end of the cooling phase. The mechanisms of this plastic thermal axial deformation of the foundation are not clear, but they may have important impacts on buildings.

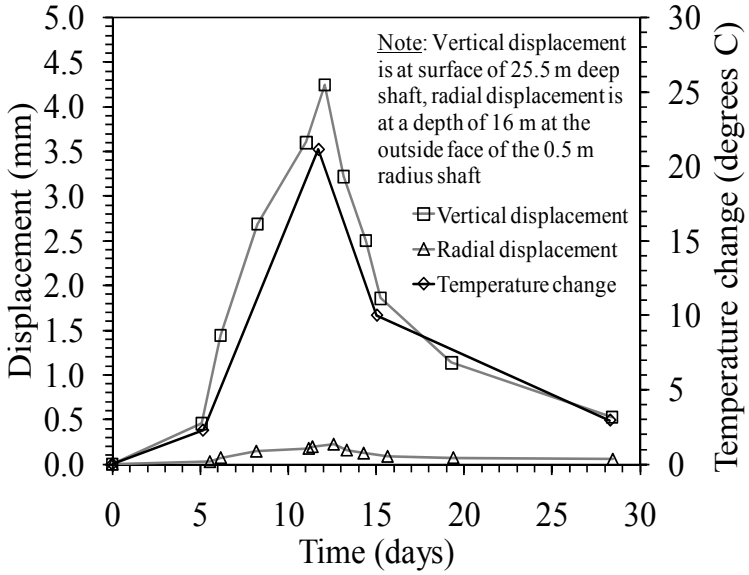

Figure 2.6: Temperature-induced axial and radial displacements in an energy foundation (Laloui et al. 2006)

CHAPTER III
Experimental Setup

3.1 Centrifuge Modeling of Energy Foundations

Field testing of energy foundations to quantify thermo-mechanically induced stresses and strains provides the most realistic response of these systems. However, field testing can be financially inefficient as well as time consuming. Further, the uncertainty about the properties of different soil layers may make analyses of field measurements complex (Laloui et al. 2006; Bourne-Webb et al. 2009). Accordingly, the 400 g-ton centrifuge at the University of Colorado Boulder was used to evaluate the response of small scale model energy foundations in carefully controlled soil layers for two different foundation boundary conditions encountered in drilled shaft foundations(end-bearing and semi-floating). Centrifuge testing permits experimental parametric evaluations with comparatively less effort, and also permits evaluation of failure conditions because the loads can be scaled and the structures are not permanent components of buildings (Rosenberg 2010).

Centrifuge modeling is based on the concept of similitude between a small-scale model in the centrifuge and a full-scale prototype in the field. The stresses and strains in a centrifuge model have a 1:1 relationship with those in the prototype structure. Other variables have different scaling relationships, which are listed in Table 3.1 (Ko 1988). Scaling relationships are only available for parameters which are dependent on gravity. This means that heat flow in soils does not scale between a centrifuge model and a full-scale prototype. Accordingly, the temperature distribution in an energy foundation-soil system during operation is not the same as that in a full-scale model. However, it is assumed that the thermal strains in the foundation induced by heating or cooling are representative of a prototype foundation.

Table 3.1: Centrifuge scaling relationships (Ko 1988)

Quantity	Prototype	Model
Acceleration	1	N
Length	1	1/N
Force	1	$1/N^2$
Stress	1	1
Strain	1	1
Stiffness	1	1
Displacement	1	1/N
Time (Diffusive flow processes)	1	$1/N^2$
Temperature	1	1

3.2 Geotechnical Centrifuge Facilities

A photograph of the 400 g-ton geotechnical centrifuge at the University of Colorado Boulder showing the beam and hanging basket is shown in Figure 3.1(a), and a schematic of the beam depicting the drive system is shown in Figure 3.1(b). For a more detailed description of the centrifuge facility, please see Ko (1988). A unique aspect of the centrifuge which is necessary for the long-term tests performed in this study is the cooling system, which consists of a series of pipes attached to the inner wall of the centrifuge chamber which cooling fluid can be pumped through. The movement of air induced by the spinning centrifuge will lead to an increase in temperature if not otherwise regulated. The cooling system is attached to the walls and consists of pipes wound in a spiral pattern that contain a cooling fluid. The pipes are exposed to allow for turbulent air flow and maximize the cooling potential of the system. Although slight variability in the chamber temperature occasionally occurred during testing, the cooling system was found to be suitable for maintaining a constant temperature in the centrifuge chamber.

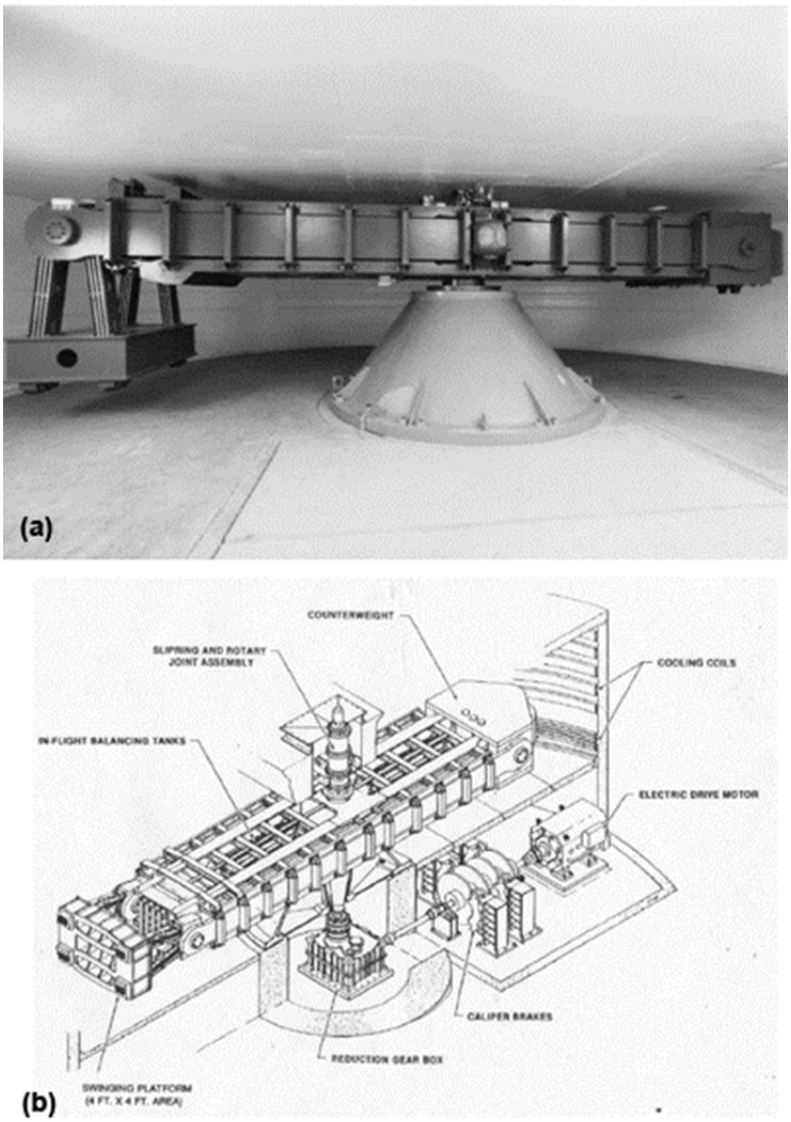

Figure 3.1: Figure depicting the 400 g-ton geotechnical centrifuge at the University of Colorado Boulder: (a) Picture; (b) Schematic

3.3 Model Foundation Fabrication

Two model energy foundations were constructed to evaluate the impact of boundary conditions, one with a length of 381 mm and the other with a length of 533 mm, both having the same diameter of 50.8 mm. Both are intended to be used in the same container of soil, and have their top (head) at the soil surface. Accordingly, the tip of the shorter foundation is intended to rest on a layer of soil, so it is referred to as a semi-floating foundation, while the tip of the longer

foundation is intended to rest on the rigid bottom of the container, so it is referred to as an end-bearing foundation. Despite the name designations, both foundations are expected to provide axial resistance to loading through a combination of end-bearing and side shear resistance.

The reinforcement of the foundations was constructed from a hoop of reinforced wire mesh having a uniform opening size of 6.35 mm and a diameter of 40.4 mm. The reinforcement cage had a concrete cover of 12.7 mm on top and bottom. Although drilled shafts are typically cast in place in the soil, the model energy foundations were precast outside of the soil layer due to the large amount of instrumentation, cables, and heat exchanger tubing within the assembly. This also permits the foundations to be reused in subsequent tests, and to be tested outside of the soil layer to characterize their thermal and mechanical properties (presented in Chapter 4). A cardboard tube having an inside diameter of 50.8 mm was used as the form for the concrete, and zip ties were used to provide spacing between the reinforcement cage and the cardboard tube.

A total of three heat exchanger loops (3 inlets and 3 outlets) were installed in each foundation. The heat exchanger tubes were constructed from 3.175 mm (1/8 inch) diameter polyethylene tubing having a working pressure of 2100 kPa at 24°C and a working pressure of 830 kPa at 65°C. The inlet and outlet branches of each tube were attached on the inside of the reinforcement cages, approximately opposite from each other. At the bottom of the foundation, the loop of tubing followed the inside perimeter of the reinforcement cage to avoid segregation of concrete during placement.

After assembly of the reinforcement cage and the attached heat exchanger tubing and instrumentation (discussed in the next section), it was inserted and centralized in the cardboard mold. Next, concrete having a mix ratio of 1:1.7:2.3:1 (water:cement:fine-aggregate:coarse-aggregate) was poured into the mold. No admixtures were included. The fine aggregate was

conventional concrete sand, while the coarse aggregate was gravel having a maximum particle size less than 6 mm (to permit flow through the reinforcement cage openings. After thorough mixing, the concrete was poured into the cardboard tube atop a shake table, and a rod was used to ensure even distribution of aggregates. The completed reinforced concrete foundation was placed in a curing room for 15 days, after which the cardboard tubing was removed. An example of a completed foundation is shown in Figure 3.2.

Figure 3.2: Photograph of a scale-model energy foundation; heat exchanger tubes and cables from embedded instrumentation are seen at top

3.4 Model Foundation Instrumentation

Embedded strain gages and thermocouples were attached to the reinforcement cage of the model foundations at varying depths before concrete placement in order to fully define the response of the foundation to thermo-mechanical loading. A schematic showing the locations of the strain gages and thermocouples is shown in Figure 3.3. A picture showing the reinforcement cage with the different instruments attached is shown in Figure 3.4.

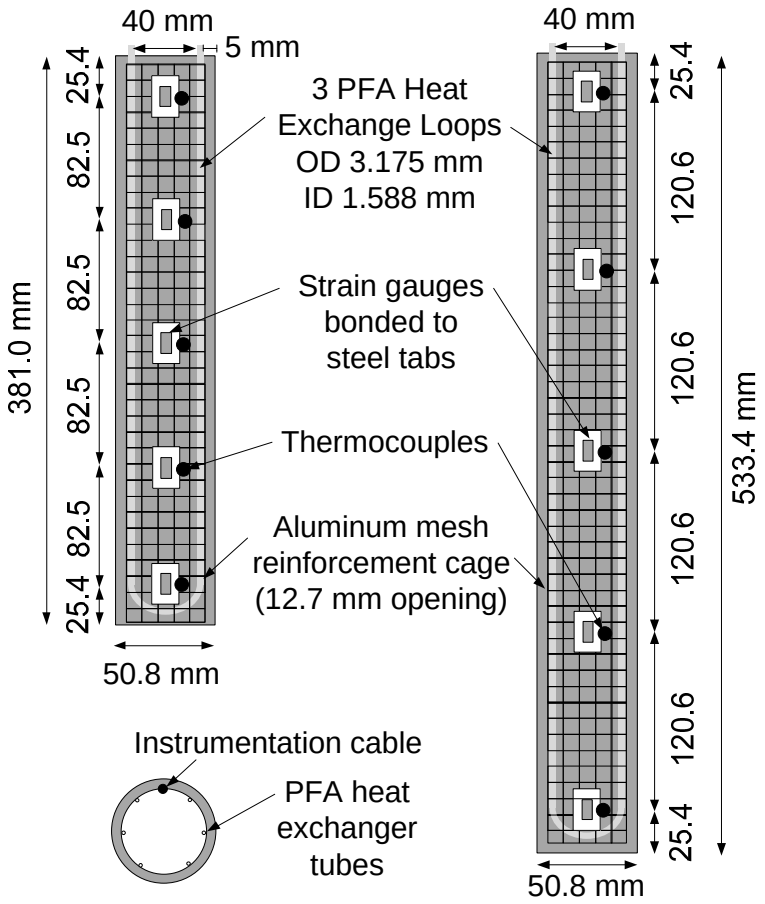

Figure 3.3: Schematic of the end-bearing and semi-floating energy foundations showing the relative locations of embedded instrumentation

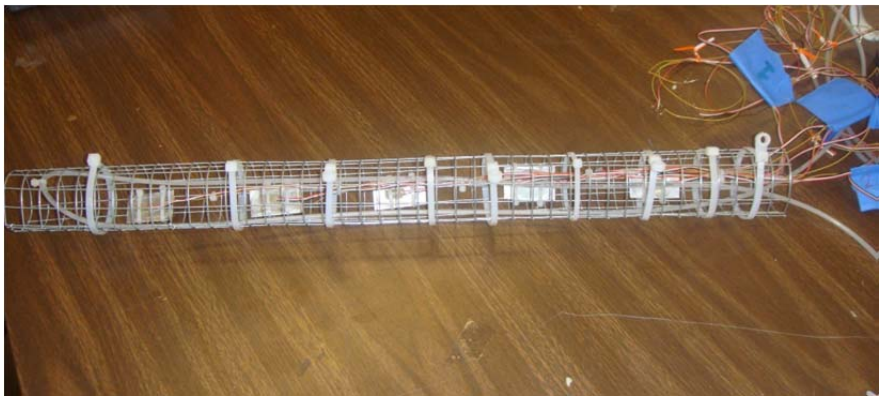

Figure 3.4: Picture showing instrumentation attached to the inside of the reinforcement cage

The strain gauges used in this study were model CEA-13-250UW-350 obtained from Vishay Precision Group – Micro-measurements®. These particular gages were selected based on their

coefficient of thermal expansion and their response to cyclic thermal loads, considering gage resilience and error due to variations in temperature (Vishay Precision Group, personal communication 2011). The coefficient of thermal expansion of the strain gages was important because if the value for the gage varied from the value of the value of the tab the gage was attached to there would be error associated with differential expansion of the gage system that would be difficult to quantify accurately. The gages have a resistance of 350 ohms ± 0.3% and operate in a temperature range of -75 to 175˚C. The gages were first attached to small steel tabs, which were then attached to the wire reinforcement cage in the model foundation. Holes were drilled in the tabs to avoid slippage between the strain gage mounts the concrete. The holes were circular to avoid large differences in strain distribution across the tab as the steel tabs are elongated.

An image of the strain gage is provided in Fig. 3.5 as well as a photograph depicting the manner in which the gages are attached to the frame in Fig 3.6. The adhesive used to attach the gages to the steel tabs was Vishay Precision Group M-Bond AE-15. This adhesive was chosen because of a more stable response under cyclic loads as compared with other adhesives as well as a resistance to thermal effects. With a curing temperature of 50 to 100 °C, this adhesive is less likely to slip at increased temperature than similar adhesives which cured at room temperature. The procedure for strain gage application used in this study followed the recommendations defined by Vishay Precision Group in Instruction Bulletin B-137. Once the adhesive had cured the strain gages and exposed contact points where coated with Micro-Measurements M-Coat J Protective coating. M-Coat J is a protective coating that protects against most fluids and mechanical damage during insulation. It is an ideal coating for this application because once fully-cured it hardens into a rubber-like consistency and guards against brittle fracture during

cyclic strain cycles. The procedure for application of M-Coat J followed the recommendations defined by Vishay Precision Group in Instruction Bulletin B-147-5.

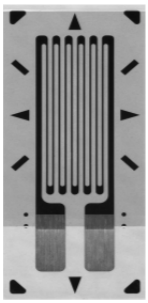

Figure 3.5: Typical linear pattern stress analysis strain gage

Figure 3.6: Strain gage attached to steel tab and covered with epoxy

A total of 10 strain gages were attached the reinforcement cage in this manner, with two gages being present at each depth. The locations of the strain gages for both end-bearing and semi-floating models are presented in Table 3.2. Initial tests indicated that the red/white/black strain gage wire was not adequate for blocking electronic noise associated with the motor and the readouts for the strain gages often had error larger than the strains being measured. To overcome this issue, cables with shielded, twisted pairs were used as the strain gage leads. This cable had four wires twisted in two pairs along with a grounding wire. The use of these cables minimized the noise in the strain gage to a point that the signal was at least an order of magnitude greater than the electromagnetic noise.

Table 3.2: Model-scale depths from top of foundation of strain gages and thermocouples in the end-bearing (length of 533.4 mm) and semi-floating (length of 381.0 mm) model foundations

		Depth (mm)
End-bearing	Strain Gage 1	508.0
	Strain Gage 2	387.4
	Strain Gage 3	266.7
	Strain Gage 4	146.0
	Strain Gage 5	25.4
Semi-floating	Strain Gage 1	355.6
	Strain Gage 2	273.1
	Strain Gage 3	191.0
	Strain Gage 4	108.0
	Strain Gage 5	25.4

In addition to the strain gages, miniature thermocouples were embedded within the foundation at the same depths as the strain gages. The thermocouples used were Omega fine wire Type K thermocouples, Model STC-TT-K-36 3C. Once the strain gages were attached to the reinforcement cage the thermocouples were taped to the back of strain gages on one side of the foundation, for a total of five locations. The range of temperature which can be measured by this model of thermocouple is -270 to 400 °C.

3.5 Heat Control System

In the centrifuge testing performed in this study, the temperature of the model foundation is controlled by circulating fluid with a known temperature through the heat exchanger tubing embedded in the foundation. The temperature of the fluid is controlled by a heat pump located outside of the centrifuge, which contains a bath of heat exchanger fluid. The rate of flow through the foundation is controlled with a system of 2 valves that can be opened and closed remotely through the LabView program to change the rate of flow through the foundation as compared with the rate of flow allowed to bypass the foundation system. For example, before any heat is applied to the foundation the valve controlling flow to the foundation is completely closed and

the valve controlling the flow that bypasses the system is completely open. If heat flow through foundation is to be maximized, then the bypass valve is closed and the inlet valve into the foundation is opened. To hold a steady temperature each valve is opened partially depending on the desired temperature. The heat pump used was a Julabo F25-ME, shown in Figure 3.7, which can control the temperature of the 4.5 liter bath to temperatures ranging from -28 to 200 °C and can supply flow rates ranging from 11 to 16 liters/minute. The heat exchange fluid used in this experiment was ProTek EG^{TM} Heat Transfer Fluid, which is an ethylene glycol fluid manufactured by Specialty Chemical Manufacturing, Inc. of Quincy, FL.

Figure 3.7: Julabo F25-ME heat pump

The fluid with a known temperature is then circulated through the hydraulic slip rings in the arm and then through insulated tubing down to the model foundation at the end of the arm (approximately 4.5 meters from the center of the arm to the top of the model). One of the reasons for using ethylene glycol is that it is compatible with the seals in the slip rings, which normally

are used to transport hydraulic oil. Because of the long length of tubing required, there were significant head losses in the tubing, which were greater than the capacity of the circulating pump within the heat pump. Accordingly, an auxiliary centrifugal pump was added in-series to increase head required to overcome these losses and have adequate flow of fluid through the system. This auxiliary pump was a Taco Model 009-F5 High Velocity Cartridge Circulator with a working fluid temperature range of 4 – 110 °C and a maximum flow rate of 30 L/min. A photograph of the auxiliary pump is presented in Figure 3.8. With the heat pump and auxiliary pump working together the total flow rate through the system was approximately 240 ml/min. Swagelok fittings were used throughout the hydraulic system, and 9.525 mm diameter high-temperature PFA tubing was used to minimize head losses through the tubing. A schematic of the overall heat control system is shown in Figure 3.9.

Figure 3.8: Taco Model 009-F5 high velocity centrifugal pump (cartridge circulator) used in-series with Julabo heat pump to increase flow through system

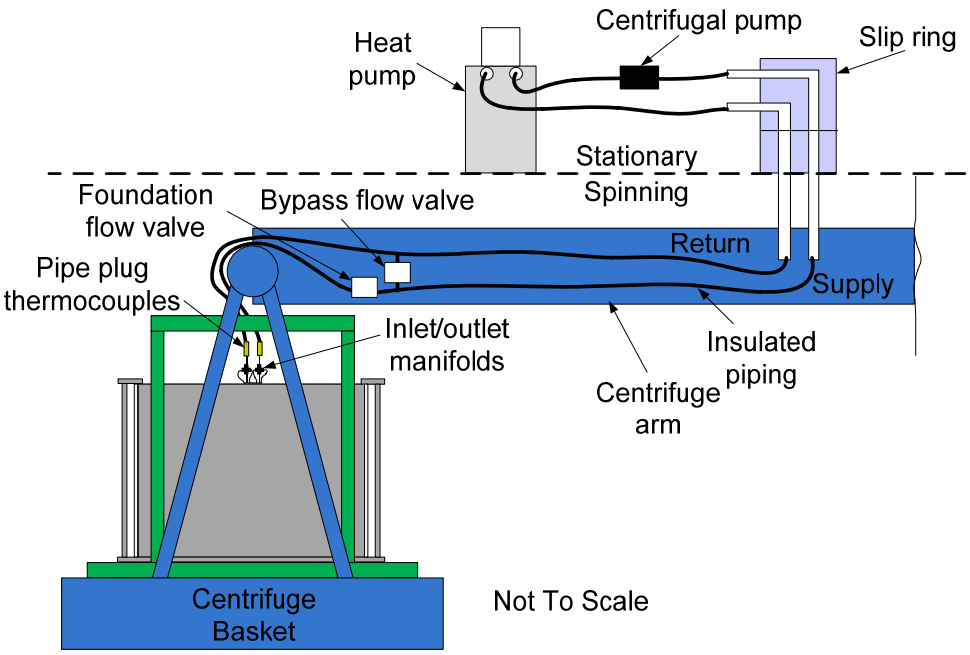

Figure 3.9: Schematic of overall temperature control system, including heat pump, auxiliary pump and fluid transition into experimental setup

3.6 Temperature Control of Foundation

The temperature in the foundation was controlled using the 2 valves set up along the fluid exchange system prior to the fluid reaching the foundation. These valves were referred to as the bypass valve, which created a loop which did not include the foundation and the foundation flow valve, which could be opened to allow fluid to flow into the foundation. These valves are included in the schematic presented in Figure 3.9. This valve system allowed for a single target temperature to be entered into the heat pump which allowed for remote control of the temperature system. By opening and closing the valves, a target temperature could be maintained in the foundation. In addition, keeping the bypass valve partially opened allowed heated fluid to pass back through into the heat pump, which reduced the demand on the system and allowed for higher temperatures to be maintained in the foundation for a longer time period.

3.7 Testing Frame and Container

The frame used in this study was constructed specifically to house the container for the scale-model, which was sized to ensure adequate horizontal distance to develop measurable heat flow and adequate vertical height to ensure semi-floating model conditions could be simulated with clearance between bottom of foundation and container greater than or equal to three times the foundation diameter to ensure no bottom-boundary effects during testing. The loading frame is shown in Figure 3.10. This figure shows a rotating table at the bottom which permits the specimen to be rotated during testing. This rotating table was removed for this study to provide additional clearance above the top of the container and the frame.

Figure 3.10: Loading frame for the 400 g-ton geotechnical centrifuge

A brushed-DC electric motor with a worm-drive gearbox, attached to the top of the frame, is used to apply loads to the head of the foundation and capable of applying forces as large as 2000

kN at rates from 0.001 to 1 mm/min. A picture of the motor mounted atop the frame is presented in Fig. 3.11. The motor was controlled using feedback from the measured using the motor control software within National Instruments LabView 2011 version 11.0 software. The applied load was measured using a Futek LSB350 load cell having a capacity of 8896 N.

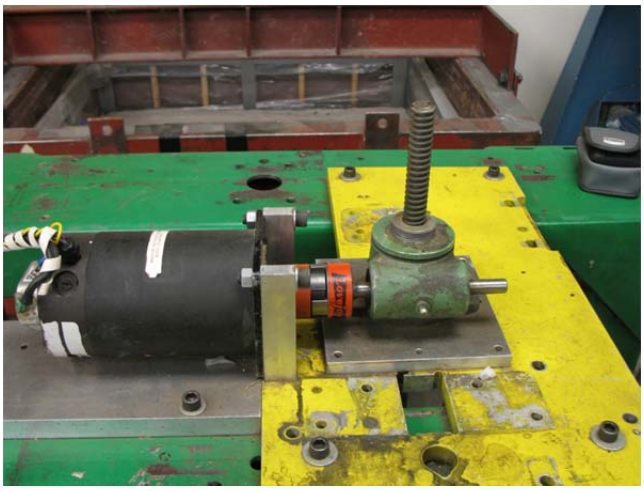

Figure 3.11: Brushed DC motor used to apply building load to model foundation

The container itself has an inside diameter of 605 mm and an inside height of 537 mm. The thickness of the walls is 13 mm and the outside of the cylindrical section was wrapped with 13 mm-thick insulation layer to avoid temperature loss from the sides of the container during centrifugation. This helps to maintain a constant temperature boundary condition for the foundation-soil system. The container is shown in Figure 3.12.

Figure 3.12 Soil container within the load frame

3.8 Soil Instrumentation

In order to define the behavior of the soil-foundation system a variety of instrumentation was used to measure the conditions in the soil surrounding the foundation. In general, there were three different processes being monitored during a test: water flow, heat flow and soil settlement (due to consolidation or thermally-induced volume change).

Thermally-induced water flow was monitored by tracking changes in volumetric water content using EC-TM® dielectric sensors manufactured by Decagon Devices. The three-pronged sensor measures both temperature and volumetric water content. Five of these sensors were placed in the soil during the compaction stage. The sensors were placed such that both vertical and horizontal variations in volumetric water content could be recorded. A photograph of placement of the dielectric sensors during specimen preparation is presented in Figure 3.13. Table 3.3 contains the depths from the surface and radial locations away from the foundation of the dielectric sensors for the tests on the end-bearing and semi-floating model foundations. A schematic of the general locations and layout of these sensors is shown in Figure 3.14.

Table 3.3: Locations of EC-TM® dielectric sensors in the tests on end-bearing and semi-floating model foundations

		Depth (mm)	Radial Distance (mm)
End-bearing	Dielectric Sensor 1	38.1	50.8
	Dielectric Sensor 2	164.3	50.8
	Dielectric Sensor 3	266.7	50.8
	Dielectric Sensor 4	266.7	139.7
	Dielectric Sensor 5	266.7	215.9
Semi-floating	Dielectric Sensor 1	38.1	50.8
	Dielectric Sensor 2	114.3	50.8
	Dielectric Sensor 3	190.5	50.8
	Dielectric Sensor 4	190.5	139.7
	Dielectric Sensor 5	190.5	215.9

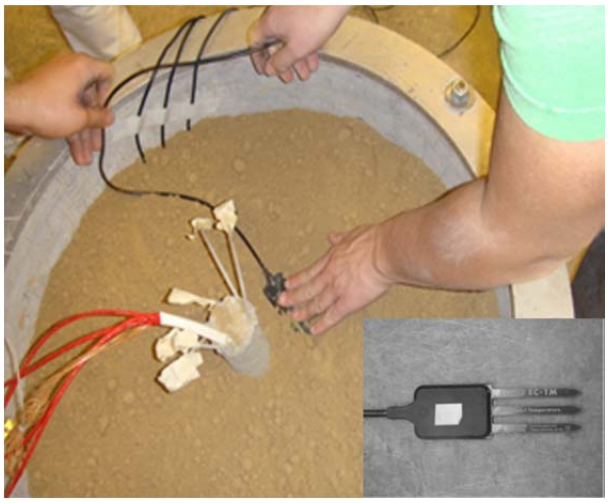

Figure 3.13: Photograph of an EC-TM® dielectric sensor being placed during specimen compaction

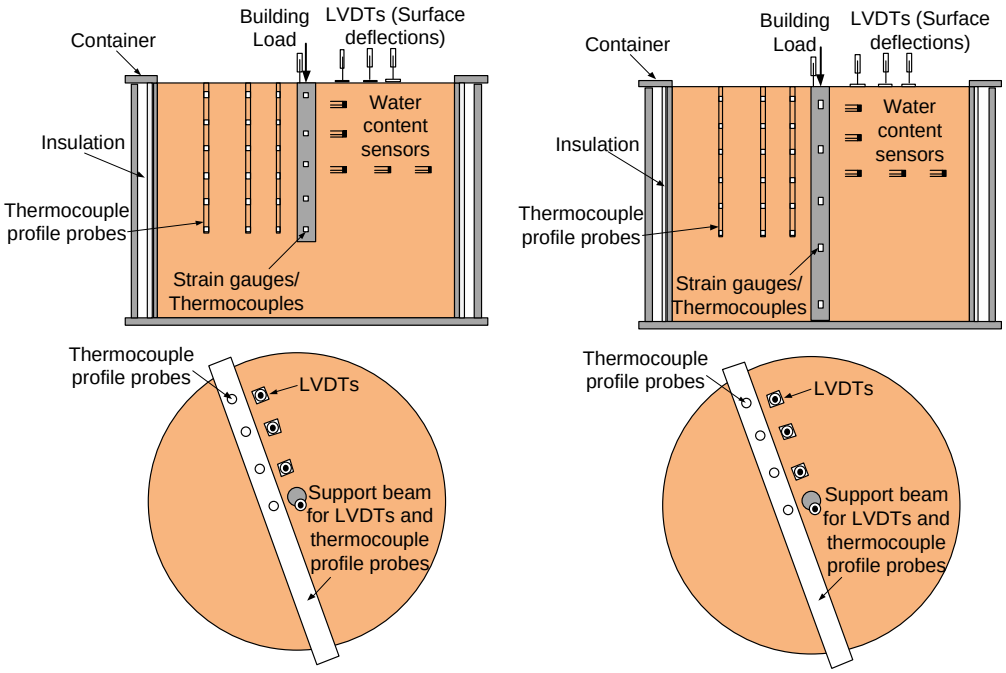

Figure 3.14: Schematic showing approximate locations of instrumentation

In the case of end-bearing boundary conditions heat flow through the soil was measured using four thermocouple profiles probes inserted into the soil at radial distances from the foundation of 76.0, 140.0, 216.0 and 292.0 mm. The thermocouple profile probes used in this study were manufactured by Omega Engineering (model PP6-36-K-U-18) and include 6 type K thermocouples at spaced at 50 mm from the tip. The thermocouples have a linear range in temperature response between -200 and 650 °C. Each thermocouple profile probe was inserted into the soil through a bar to ensure proper placement such that the depths of each thermocouple from the surface was 114.3, 152.4, 190.5, 228.6, 266.7 and 304.8 mm. The general locations of these probes are shown in Fig. 3.14 and a photograph of the thermocouple profile probe is provided in Fig 3.15. For the case of the semi-floating model foundation test, the soil was compacted to a higher density than for the end-bearing condition and it was not possible to insert the probes into the soil, as will be discussed in Chapter 5.

Figure 3.15: Photograph of a thermocouple profile probe

Settlement of the foundation and the soil surrounding was monitored using linear variable deformation transformers (LVDTs). A photograph of a typical LVDT used in this study is presented in Fig 3.16 (inset). The first of the four LVDTs was mounted such that it rested on the top of the foundation. The remaining three were placed on top of the soil at radial distanced from the foundation of 76.2, 91.6 and 127.0 mm. In order to ensure consistency for different specimens, an LVDT mounting bracket was attached across the top of the container (see Fig. 3.16). The bracket consisted of a hollow square tube with plastic LVDT mounts permanently attached to it such that the LVDTs are in the same location for each test. In addition, this mounting bracket had holes drilled into it where the thermocouple profile probes were inserted to ensure proper location and vertical alignment for each test.

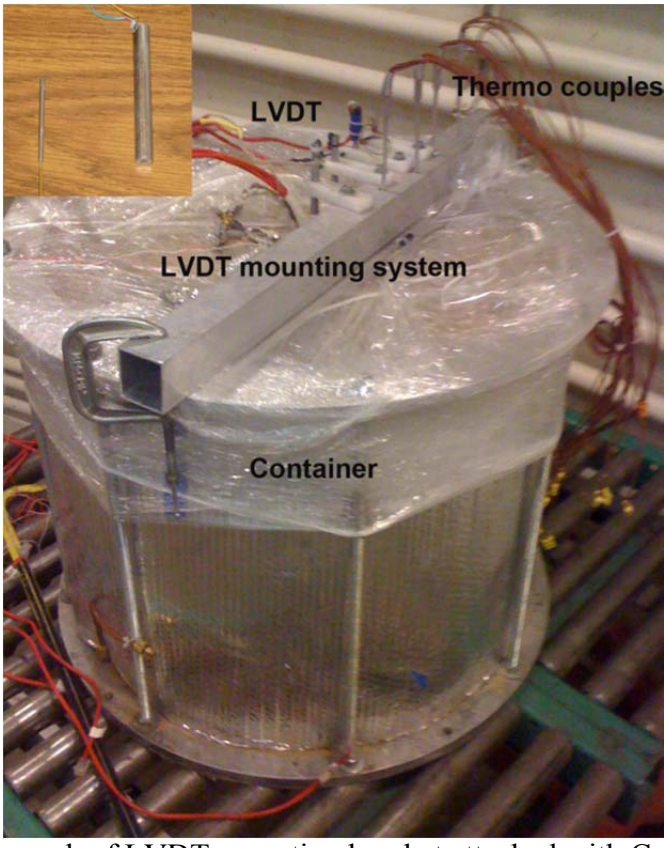

Figure 3.16: Photograph of LVDT mounting bracket attached with C-clamps to container before testing, as well as an inset photograph of a typical LVDT used in testing

CHAPTER IV
Material Properties

4.1 Soil Properties

4.1.1 Summary

Silt recovered from the Bonny dam near the Colorado-Kansas border (referred to as Bonny silt) was used as part of this study. The reasons for using this soil are that it has low plasticity so temperature is not expected to lead to changes in soil-pore water interactions (i.e., diffuse double layer effects) and it has a high fines content so the silt will behave like a low-permeability material (e.g., thermal consolidation can be observed). The silt in the physical modeling tests was prepared using compaction, which was found to fast preparation times. An extensive database of laboratory test results on the mechanical and thermal properties of this soil is also available.

4.1.2 Geotechnical Characteristics

The specific gravity of a soil (G_s) is defined as the ratio of a mass of a specific volume of the soils solids as compared with the mass of that same volume of water at 20°C. A value for G_s of 2.6 was used based on tests performed by El Tawati (2010). The Atterberg limits for Bonny silt are presented in Table 4.1. This data was obtained by following ASTM D4318.

Table 4.1: Atterberg limits for Bonny silt

Parameter	Value
Liquid limit	24
Plastic limit	21
Plasticity index	4

The grain size distribution analysis was performed following ASTM D422. A hydrometer was used to determine the distribution of particles passing No. 200 sieve, while a sieve analysis was used to determine the distribution of particles retained on the No. 200 sieve. The grain size distribution is shown in Figure 4.2 and characteristic grain size values are presented in Table 4.2.

Based on the grain size distribution data and the Atterberg limits, Bonny silt is classified as ML according to the Unified Soil Classification System (USCS).

Table 4.2: Grain size distribution data for Bonny Silt

Parameter	Value
D_{10}	<0.0013 mm
D_{30}	0.022 mm
D_{50}	0.039 mm
% Passing No. 200 Sieve	83.9%
% Clay Size	14.0%
% Silt Size	69.9%
% Sand Size	16.1%

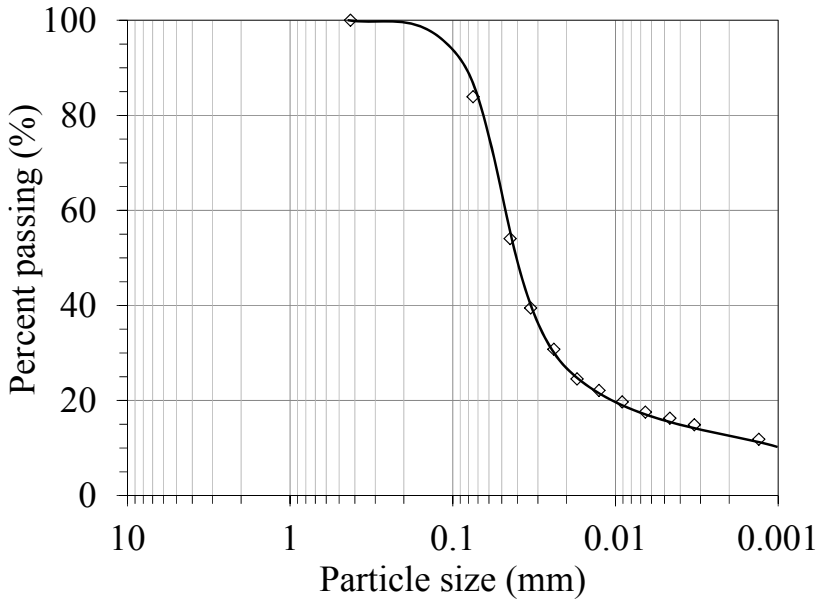

Figure 4.1: Grain size distribution curve for Bonny silt

The compaction curves were obtained for the silt using both the standard (ASTM D698) and modified (ASTM D1557) compaction techniques. The resultant curves from this testing are presented in Figure 4.2. The optimum water content for Bonny silt is 13.2% and the maximum dry density with respect to the standard Proctor compaction effort is 16.3 kN/m^3.

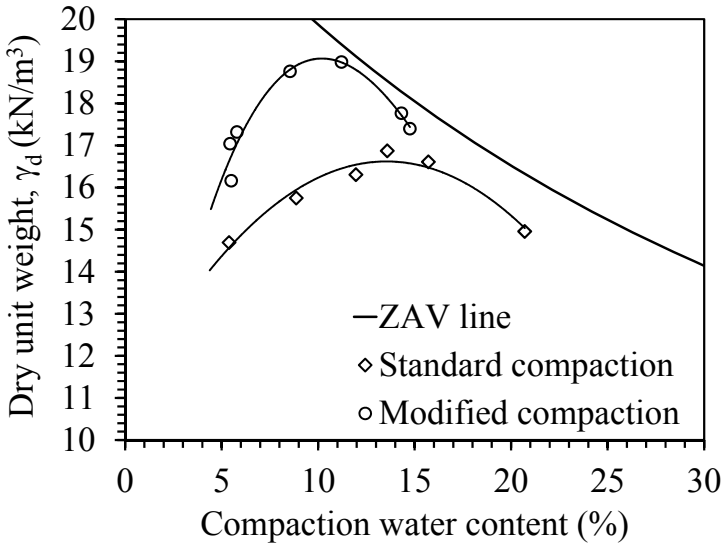

Figure 4.2: Compaction curves for Bonny silt obtained using both standard and modified Proctor compaction efforts, plotted with the zero air void (ZAV) line.

4.1.3 Mechanical Properties

The stress paths obtained from three consolidated undrained (CU) triaxial tests performed in accordance with ASTM standard D4767 on saturated Bonny silt specimens are shown in Figure 4.3. These stress paths indicate that for this range of mean effective stress, Bonny silt exhibited behavior similar to over-consolidated soils. Specifically, compacted Bonny silt exhibits a dilative soil behavior with negative excess pore water pressure generation during shearing. The slope of the critical state line is 1.305, corresponding to a drained friction angle of 32.4°.

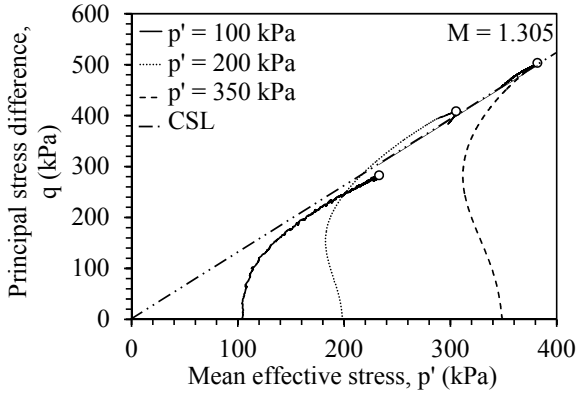

Figure 4.3: Effective stress paths for compacted Bonny silt plotted for initial consolidation effective stresses of 100, 200 and 350 kPa

The small-strain shear modulus (G_{max}) was measured for a variety of net stresses and plotted as a function of mean effective stress with the model (described below) in Figure 4.4. The small strain shear modulus can be represented according the following equation:

$$G_{max} = AP_a \log\left(\frac{p'}{P_a}\right)^n$$

where P_a is the atmospheric pressure used for normalization, and the fitting parameters A and n for this data set are 0.42 and 0.52, respectively.

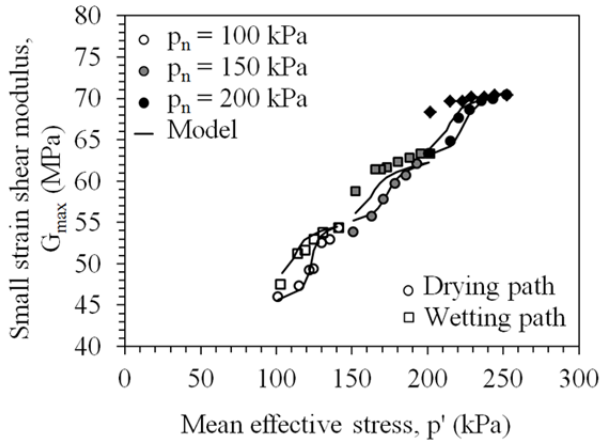

Figure 4.4: Changes in small-strain shear modulus with mean effective stress

4.1.4 Hydraulic Properties

The hydraulic properties of Bonny silt were measured using the flow pump technique developed by Aiban and Znidarcic (1989). This technique was used to define the saturated hydraulic conductivity using a constant flow rate approach, and was later combined with the axis-translation technique to measure the soil-water retention curve (SWRC) and hydraulic conductivity function (HCF) of unsaturated soils. A plot of saturated hydraulic conductivity for a variety of void ratios is presented in Figure 4.5. The data for this plot was taken from previous literature published using this technique. The hydraulic conductivity of saturated specimens having initial void ratios ranging from 0.5 to 0.8 ranges from $1x10^{-9}$ to $1x10^{-7}$ m/s. The SWRC

for Bonny silt specimen having an initial void ratio of 0.69 under a range of net stresses are shown in Figure 4.6.

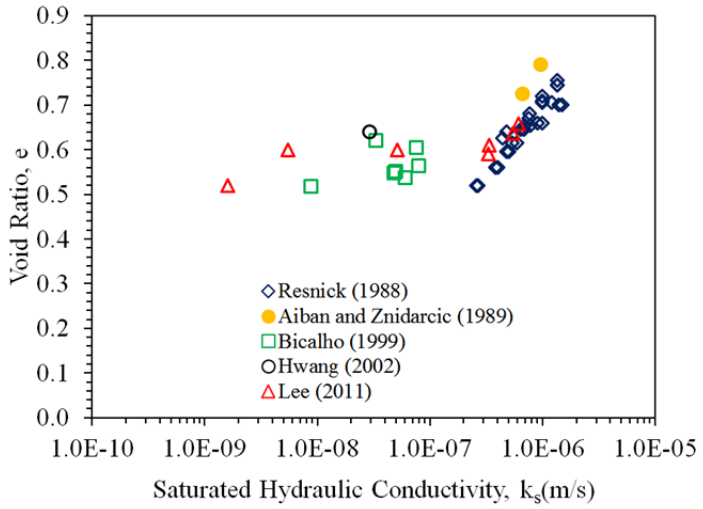

Figure 4.5: Hydraulic conductivity as a function of void ratio for a variety of tests performed on Bonny silt

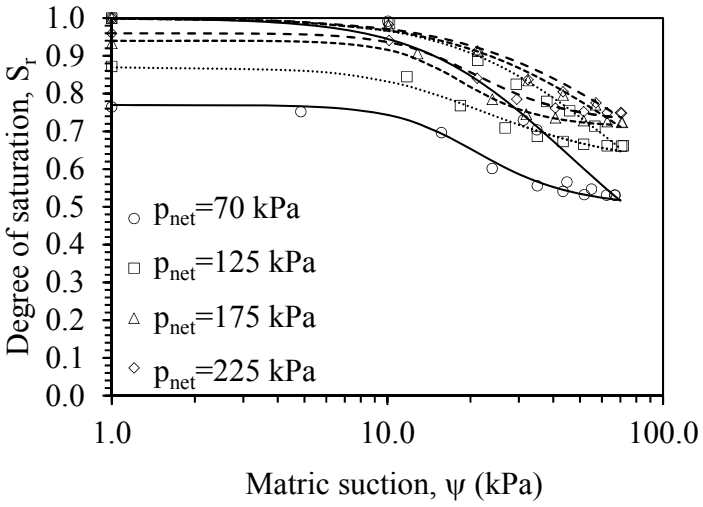

Figure 4.6: SWRCs for Bonny silt specimens having an initial void ratio of 0.69 under a range of net stresses

4.1.5 Thermal Properties

The thermal conductivity of Bonny silt as a function of void ratio was obtained using a triaxial cell adapted to accommodate a miniature thermal needle (70 mm length) probe in the top platen. The needle probe was used to infer the thermal conductivity of the soil specimen using

the line-source equation. The thermal conductivity of Bonny silt was measured after isotropic consolidation of a cylindrical specimen to different void ratios, with typical results from two tests shown in Figure 4.7. The thermal conductivity was also measured of the actual soil layers used in the centrifuge tests using a larger thermal needle (125 mm length), and the thermal conductivity values ranged from 1.47 to 1.98 W/mK for void ratios of 0.63 and 0.47, respectively (see soil specimen preparation results in Chapter 5). These measurements are consistent in the trend shown in Figure 4.7.

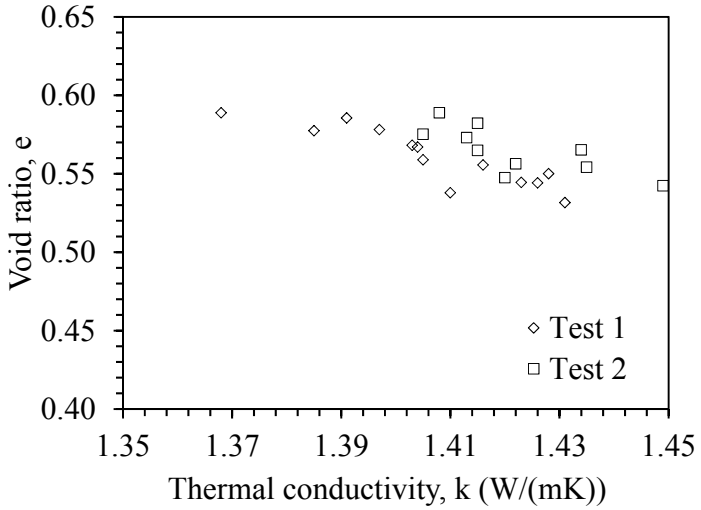

Figure 4.7: Relationship between thermal conductivity and void ratio for Bonny silt

4.2 Foundation Properties

4.2.1 Summary

The model foundations used in this study were 50.8 mm in diameter and 533 and 381 mm in length for end-bearing and semi-floating conditions, respectively. They were fabricated using a concrete mix design of 1:1.7:2.3:1 (water:cement:fine-aggregate:coarse-aggregate). The reinforcement cage was a wire mesh with uniform openings of 6.35 mm and a diameter of 40.4 mm. Additional details concerning model fabrication are presented in Chapter 3. The material

properties of the reinforced concrete in the model foundations were obtained through evaluation of the end-bearing foundation only.

4.2.2 Mechanical Properties

Pre-cast concrete foundations were used in this study to ensure consistency during foundation fabrication and ease specimen preparation. These foundations were fabricated using a higher fine to coarse aggregate ratio to increase the foundation thermal conductivity and to ensure adequate flow around the small openings created by the instrumentation and tubing. A 1g loading test was performed to determine the modulus of elasticity of the foundation system. Data for this test was recorded from strain gages embedded in the foundation as well as motor counts from the loading system converted to vertical movement at the top of the foundation during loading. The load applied to the foundation was applied in steps and recorded as sensors reached equilibrium, as shown in Figure 4.8(a). At the highest stress level, the LVDT slipped and recorded too high of a displacement. The hysteretic behavior noted in the LVDT and motor position is possibly due to crushing of a bead of concrete on the bottom of the foundation. The final load applied resulted in a maximum axial stress of approximately 1400 kPa. Since this foundation was loaded axially with no surrounding soil mass to offer side shear resistance it was expected that the foundation would respond as a rigid body and all strain gages would record similar deformations. The results from the strain gages are presented in Figure 4.8(b). During this 1g test there were only three of the ten gages provided a mechanical response consistent with the external strain measured from the motor position. It is possible that the embedment contact between the concrete and the steel tabs of some of the gages was not adequate, making them less sensitive to changes in stress in the foundation. Because some of the gages showed a slight tensile response, buckling could have been another possibility. However, there was no pattern with height in the

foundation (tension on one side and compression on the other) which would suggest that this is the case. The stress-strain data presented in Figure 4.9(a) was corrected based off of this assumption, assuming that the gage at the bottom of the foundation was providing the proper response, and the gages were corrected for mechanical response as shown in Figure 4.9(b). Correction factors for the functional strain gages are presented in Table 4.3. The slope of the corrected stress-strain curve indicates that the foundation has a Young's modulus E of 7.10 GPa. This is about 3 times less than that of the foundation of Stewart and McCartney (2012). This lower value can be explained by the greater amount of sand was used in the concrete mix design.

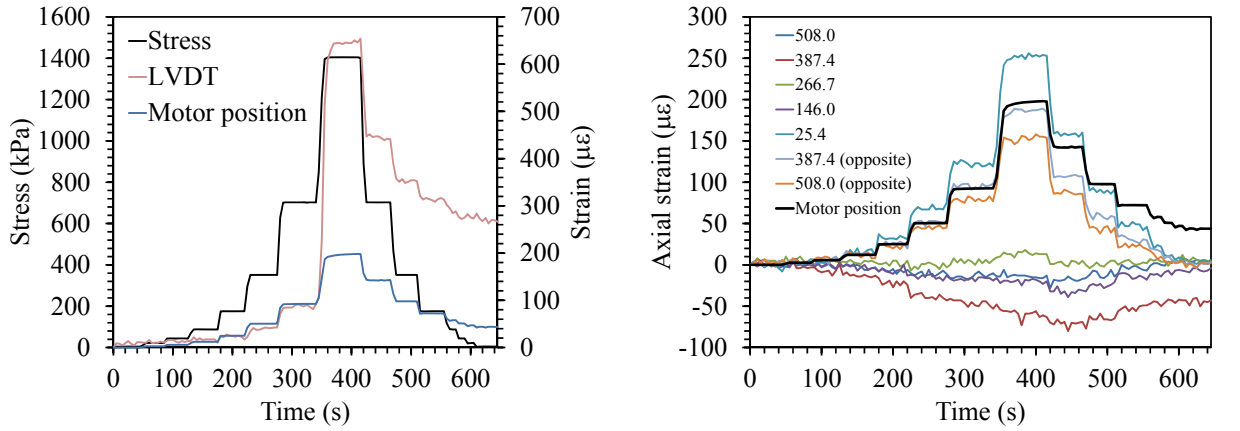

(a) (b)

Figure 4.8: Mechanical characterization results: (a) Load, LVDT and Motor position; (b) Motor position strain with strain gage readings

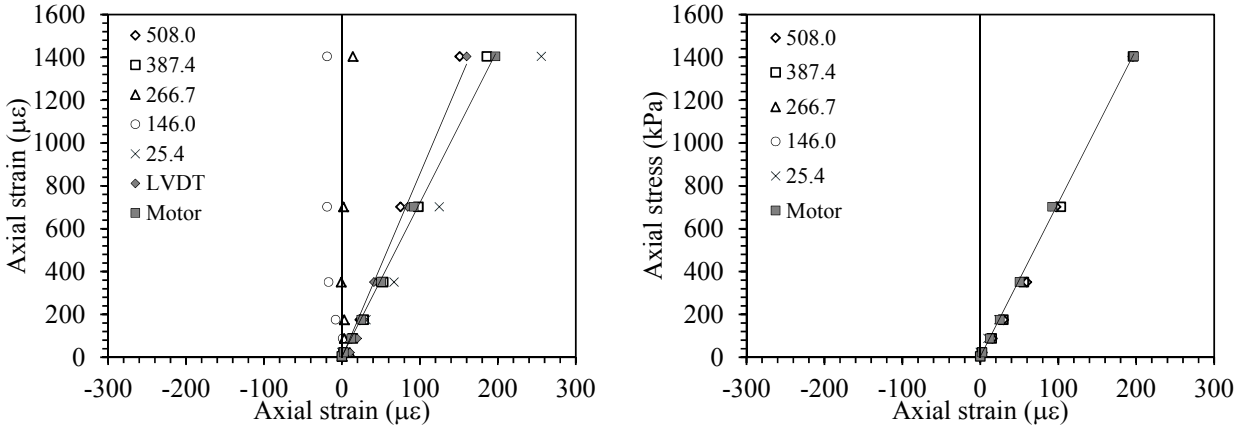

(a) (b)

Figure 4.9: Stress vs. strain diagram for model energy foundation indicating a total elastic modulus for foundation system of 7.17 GPa: (a) Uncorrected; (b) Corrected

Table 4.3: Mechanical correction factors for strain gages embedded in end-bearing model based on 1g loading test results

Depth from Ground Surface (mm)	Correction Factor
508.0	0.78
387.4	1.25
25.4	1.06

4.2.3 Thermal Properties

Before evaluating the thermal strains from the foundation, the response of the strain gage attached to the steel tab in Figure 3.6 was first evaluated. The measurements from the strain gage along with the temperature measured using a thermocouple attached to the steel tab during heating and cooling are shown in Figure 4.10(a). The sign of the strain value is switched from the structural engineering convention (tension is positive) used in LabView® to the geotechnical engineering convention (compression is positive). During heating, the strain gage shows compression, which is opposite from expected. This was verified by noting that heating leads to the same direction of change in strain as observed in the compression test shown in Figure 4.8. This may occur because the gage has a tendency to expand more than the steel tab, leading to a net compression in the strain gage. These results also permitted definition of the coefficient of thermal expansion of the steel tab, as shown in Figure 4.10(b).

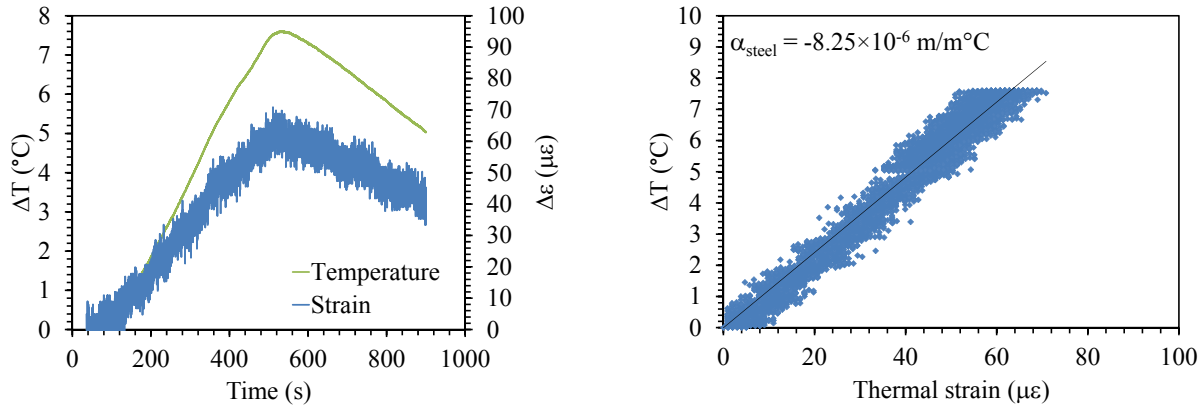

Figure 4.10: Response of strain gage attached to steel tab during heating (positive strain implies compression): (a) Time series; (b) Temperature vs. strain

During the 1g test to determine thermal properties of the foundation, the end-bearing foundation was placed upright on the load frame and an axial load of 890 N was applied to the head of the foundation (corresponding to an axial stress of 439 kPa). Once the embedded strain gages reached equilibrium, heat exchange fluid was circulated through the foundation. The inlet and outlet temperatures of the heat exchange fluid entering and exiting the foundation are shown in Figure 4.11. A constant ambient temperature was maintained during testing. The difference in inlet and outlet fluid temperatures of 7.0 °C reflects the heat energy loss through the foundation. The temperatures within the foundation measured using the embedded thermocouples are shown in Figure 4.12. The maximum temperature was held at a constant value for approximately 3000 seconds and then the system was permitted to cool down.

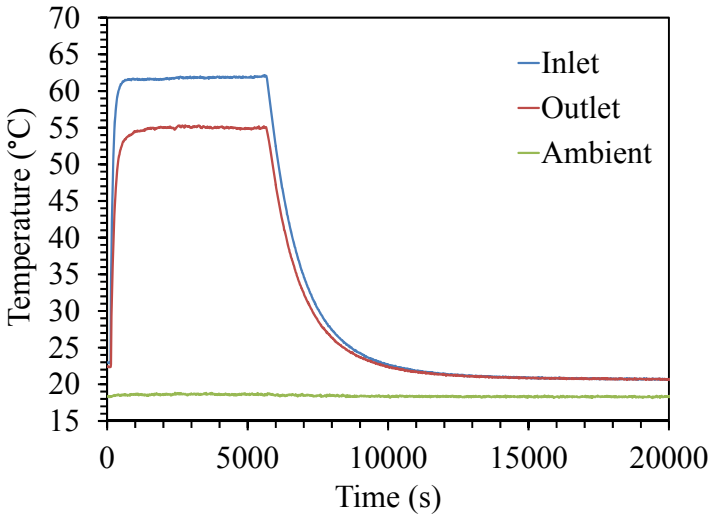

Figure 4.11: Time series of inlet, outlet and ambient temperatures during the 1g test

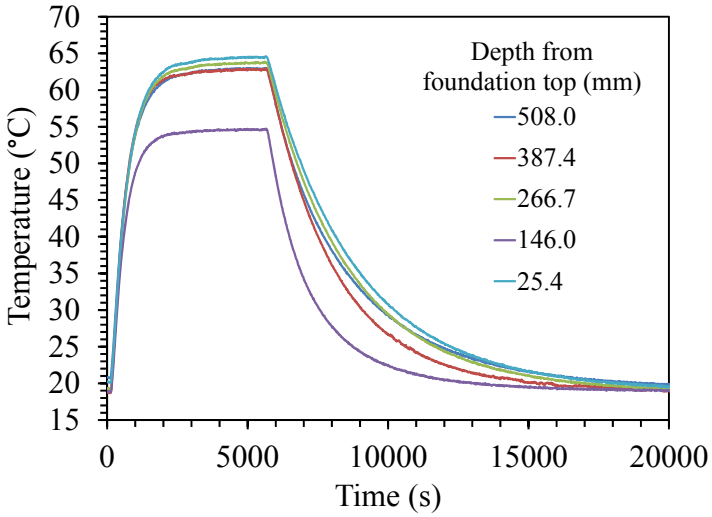

Figure 4.12: Time series of temperatures measured by thermocouples embedded in the model foundation during the 1g heating test

The displacement of the top of the foundation during both heating and cooling was also measured using the motor position encoder. The thermal strain values inferred from the motor position is shown in Figure 4.13(a). A negative axial strain implies expansion of the foundation, which is expected during heating. Because the motor was operated in load-controlled mode, the axial stress did not change, but the foundation was able to freely move. The results in Figure 4.13(a) indicate that the foundation expands nonlinearly with temperature, and that the coefficient of linear thermal expansion corresponding to the applied axial stress is approximately 7.5×10^{-6} m/m°C. The thermal axial stress can be calculated in the foundation as follows:

$$\frac{x}{l} = \alpha\Delta T + \frac{\sigma}{E} \tag{4.2}$$

where x/l is the measured strain, $\alpha\Delta T$ is the theoretical free thermal strain of the foundation, σ is the axial stress, and E is the Young's modulus. Because the foundation was free to expand, then x/l equals $\alpha\Delta T$ and the thermal axial stress is zero. The thermal stress along with the mechanical and total thermo-mechanical stresses are shown in Figure 4.13(b).

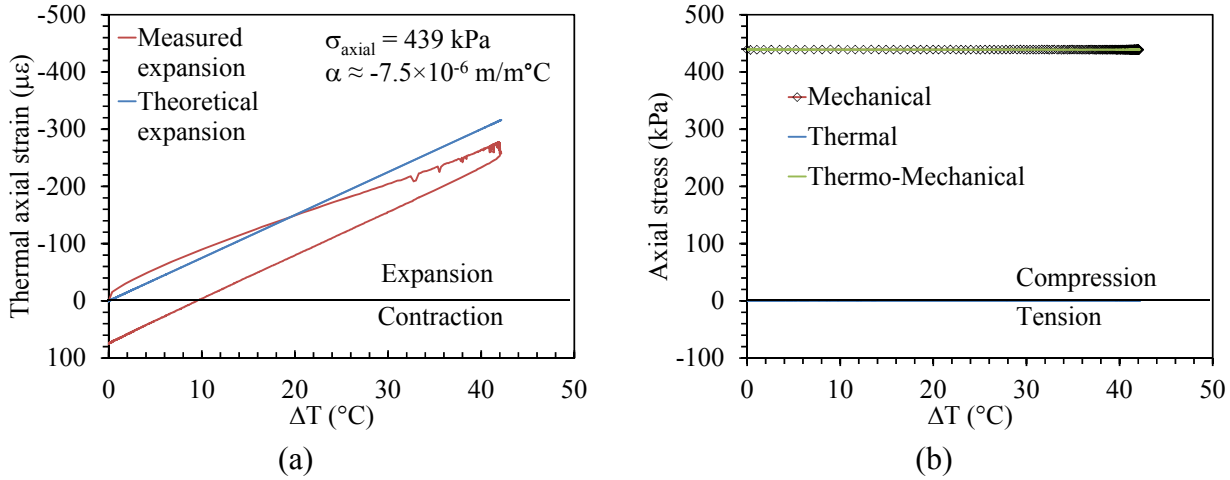

Figure 4.13: External measurements during heating for end-bearing model foundation under axial mechanical stress of 439 kPa: (a) Free (theory) and restrained (measured) thermal axial strains; (b) Thermal and mechanical stresses

The strains recorded as a result of thermal changes and mechanical load are shown in Figure 4.14(a), in addition to the movement of the foundation inferred from the motor counts of the brushed DC motor used to apply the axial loads. The different magnitudes of thermal strain are partially due to the differences in temperature and differences in thermal sensitivities of each of the gages. Comparison of the motor strain with the gage strain indicates that the gages provide the opposite response to that expected during heating. The strains were corrected by multiplying the time series by an empirical factor to match the motor strain data, as shown in Figure 4.14(b).

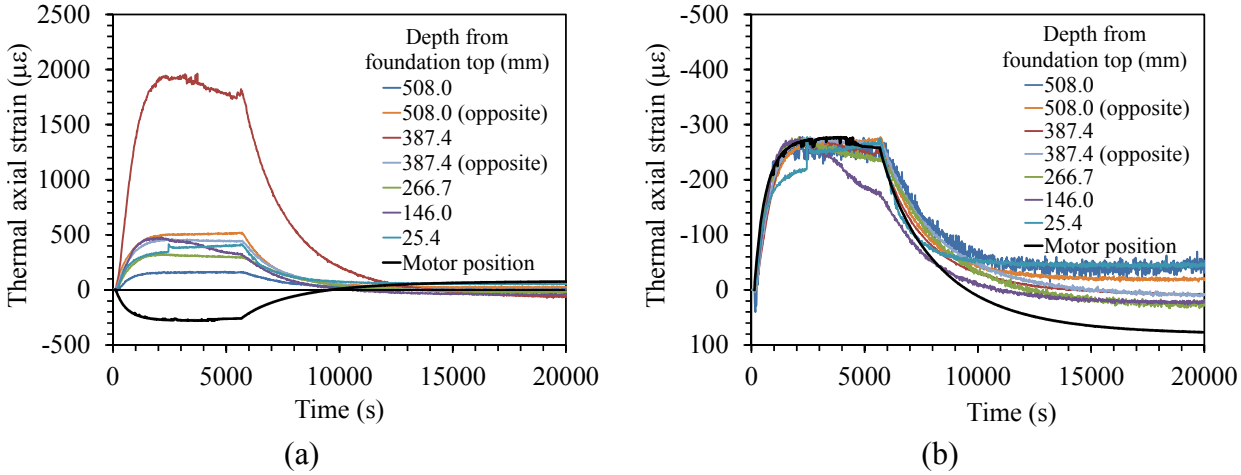

Figure 4.14: Strain measured during the 1g heating test: (a) Original; (b) Corrected

The thermal correction factors for the end bearing model obtained using this approach are listed in Table 4.4. A similar approach was used to define correction factors for the semi-floating foundation. These values are presented in Table 4.4 as well. The results in this table indicate that the strain gages require independent thermal calibration for reliable interpretation.

Table 4.4: Thermal correction factors for strain gages embedded in the foundation models

Depth from Ground Surface for End Bearing Foundation (mm)	Thermal Correction Factor for End Bearing Foundation	Depth from Ground Surface for Semi-Floating Foundation (mm)	Thermal Correction Factor for Semi-Floating Foundation
508.0	-3.22	355.6	-0.40
387.4	-0.15	273.1	-0.10
266.7	-1.14	190.5	-0.15
146.0	-0.65	108.0	-0.40
25.4	-0.84	25.4	-0.20
508.0 (opposite)	-0.20	355.6	-1.00
387.4 (opposite)	-0.75	273.1	-1.00
266.7 (opposite)	-0.10	190.5	-0.32
146.0 (opposite)	Not functioning	108.0	-0.40
25.4 (opposite)	Not functioning	25.4	-0.80

The solution to the heat equation for a line source was used to infer the thermal conductivity of the concrete foundation from the temperature measurements during heating, as follows (Campbell et al. 1991):

$$\lambda = \frac{Q}{4\pi}\left(\frac{dT}{d(\ln(t))}\right)^{-1} \tag{4.3}$$

where λ is the thermal conductivity (W/m°C), Q is internal energy (W), T is the temperature (°C) and t is time (s). The temperature time series measured at mid-point of the foundation in Figure 4.12 was interpreted using Equation 4.2, using the value of Q calculated from the energy input reflected by the difference in inlet and outlet temperatures in Figure 4.13. The thermal conductivity of the reinforced concrete was calculated to be 1.191 W/m°C.

Table 4.5: Calculation of thermal conductivity using the line source equation

Ethylene Glycol Properties		
Molar Heat Capacity	149	J/(molK)
Molecular Weight	62	g/mol
Specific Heat Capacity	2394	J/(kgK)
Density	1.113	g/ml
Test details		
T_{in}	61.9	°C
T_{out}	54.9	°C
ΔT	7.0	°C
Flow rate	5	ml/s
Mass flow	0.0056	kg/s
Entropy drift	13.32	J/(sK)
Q	93.3	W
Time-Temperature slope		
Point	Time	Temperature
1	105	5.2
2	375	20.1
dT/d(lnt)	11.7	
L	0.5334	m
Q/L	174.85	W/m
λ	**1.191**	W/(m°C)

CHAPTER V

Experimental Procedures

5.1 Specimen Preparation

5.1.1 Specimen Preparation Details

The soil specimen preparation approach used in this study was compaction. Although drilled shaft foundations are rarely installed in compacted fills, compaction is a straightforward approach to create a soil layer with a consistent density. The main advantages of using compaction to prepare the specimen are that minimal soil settlement is expected during centrifugation, which is important for minimizing testing duration, and that the soil layer may be constructed around the scale model foundation, avoiding the need to core a hole through a sedimented specimen and insert the precast foundation. The main shortcomings of compaction are that it induces higher lateral stresses onto the foundation than present in drilled shafts foundations, the stress history is not known precisely without the use of other tests, and the soil is initially unsaturated.

To start, two 55-gallon drums of Bonny silt were conditioned to a gravimetric water content of approximately 14%. This water content is approximately equal to the optimal water content for the standard Proctor compaction conditions, as shown in Figure 5.1. Water was added to the dry silt using a pressurized spray bottle to avoid clumping and was covered and left overnight for homogenization. For the semi-floating foundation, the soil layer was compacted with rubber mallets having 63.5 mm-diameter heads in lifts having thicknesses of 76.2 mm. Two soil lifts were compacted in the container before the semi-floating foundation was placed into the container corresponding to a soil base of 152.4 mm, or three times the foundation diameter. In order to ensure proper alignment of the foundation in the center of

the container, a surveying string was stretched across the container in two orthogonal directions with the point where the two crossed being the geometric center. A level was used to ensure that the foundation remained vertical. Each soil lift was added and dispersed evenly throughout the container prior to compaction effort. Scarification was performed between lifts was performed to ensure good lift interface contact and minimize the formation of weak zones within the soil layer. This compaction effort led to a dry unit weight of 17.7 kN/m^3. This density was greater than the maximum standard Proctor dry unit weight, and was initially selected because of concerns of excessive settlement of the soil at the toe of the foundation. However, this high density prevented easy installation of the thermocouple profile probes.

For the end-bearing foundation, the end-bearing foundation was placed in the container prior to soil being added such that the toe of the foundation was resting directly on the container bottom. The soil layer was then compacted with rubber mallets. Due to variability in the effort, the soil layer reached a slightly lower dry unit weight of 15.7 kN/m^3. The compaction points are shown along with the standard and modified Proctor compaction curves in Figure 5.1. A summary of the compaction conditions for the tests on the two foundations having different boundary conditions is shown in Table 5.1, including placement gravimetric water content, dry unit weight, initial void ratio and degree of saturation. The thermal conductivity values obtained using a 125 mm-long thermal needle test with the KD2Pro system are also listed in this table.

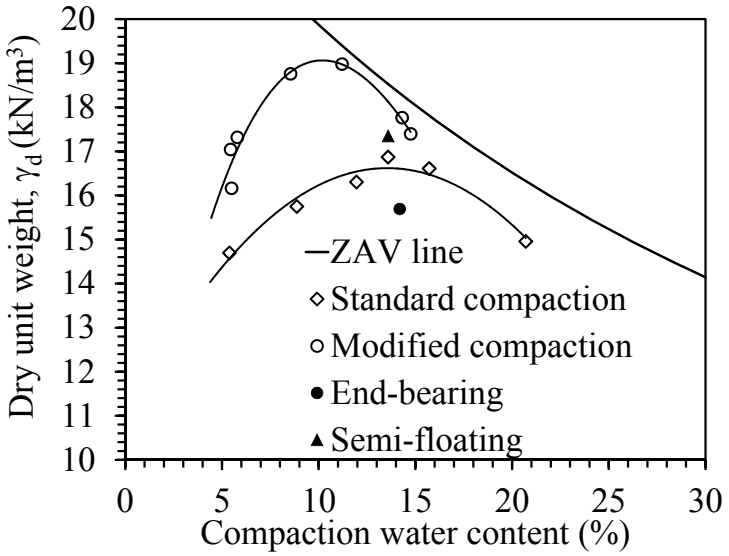

Figure 5.1: Compaction curves for Bonny Silt for standard and modified Proctor compaction, including the as-built compaction conditions for the soil in the tests on the end-bearing and semi-floating foundations

Table 5.1: As-built compaction conditions for soil specimens used to evaluate the effect of end-bearing and semi-floating foundation test

Foundation End Boundary Condition	w (%)	ρ_d (kg/m^3)	γ_d (kN/m^3)	$e_{initial}$	S	Thermal conductivity (W/mK)
End-Bearing	14.2	1599.8	15.7	0.63	0.59	1.47
Semi-Floating	13.6	1769.1	17.7	0.47	0.75	1.98

A photographic series of the soil compaction procedures is shown in Figure 5.2. A picture of the container with a loose soil lift is shown in Figure 5.2(a). A compacted soil layer showing scoring between layers is shown in Figure 5.2(b). Figure 5.2(c) shows the fourth lift pre-compaction, evenly distributed around the centered foundation. Also shown in Figure 5.2(c) are the cables from embedded dielectric sensors and the heat exchanger tubes, which are covered with masking tape to prevent clogging during specimen preparation.

(a)

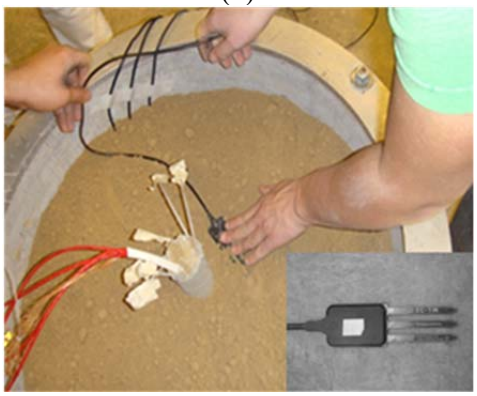

(b)

(c)

Figure 5.2: Photographic series depicting soil compaction procedures: (a) end-bearing foundation being centered pre-compaction; (b) placement of water content sensor during compaction (inset: dielectric sensor); (c) fourth loose lift distributed around centered foundation pre-compaction

5.1.2 Installation of Instrumentation

In addition to the instrumentation embedded in the model energy foundations, the instrumentation described in Chapter 3 was installed at different locations within the soil

mass. During compaction of the specimen, five EC-TM® dielectric sensors were placed in the soil at varying depths radial distances from the foundation and at different depths. The locations of these sensors are presented in a table in Chapter 3. The dielectric sensors were placed into two arrays: a radial array at approximately mid-height of the foundation and a vertical array above the sensor nearest to the foundation. These two arrays of dielectric sensors are shown in Figure 5.3.

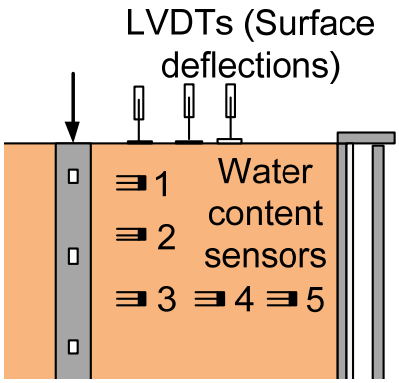

Figure 5.3: Schematic of the 5 dielectric sensors arranged in a vertical array (1-2-3) and a horizontal array (3-4-5)

The four thermocouple profile probes were inserted after compaction of the soil layer. After assembly of the instrumentation rack across the top of the container, holes were predrilled with a length of threaded rod to the final depth of the probes. The probes were then inserted in to the holes, a snug fit was ensured. The thermocouple profile probes showed good correspondence with the temperatures from the dielectric sensors, indicating that the soil and probes had adequate contact. The thermocouple profile probes were not installed in the soil layer around the semi-floating foundation due to the high density of the soil and time constraints on the day of testing, but they were installed in the soil around the end-bearing foundation. The lack of thermocouple profile probes in the test on the semi-floating foundation was not deemed to be an issue because the dielectric sensors were still available

to provide a quantification of the temperature in the soil, and the main focus of this research is on the thermo-mechanical response of the foundation. The radial locations of the four thermocouple profile probes as well as the depths from the ground surface of each of the embedded thermocouples is presented in Table 5.2 for the end-bearing foundation test.

Table 5.2: Locations of thermocouples in the thermocouple profile probes for the end-bearing foundation test

Radial Distance from Foundation (mm)	Depth from Ground Surface at each Location (mm)
76.0	114.3
140.0	152.4
216.0	190.5
292.0	228.6
[redacted]	266.7
[redacted]	304.8

The LVDT's used to measure vertical settlement at the soil surface and foundation were attached to the instrumentation rack secured across the top of the container, as observed in Figure 5.4. The LVDTs were zeroed at the beginning of the test (before centrifugation). These sensors were the last instruments to be mounted on the container prior to testing. The radial locations of the LVDTs were the same for both the end-bearing and semi-floating foundation tests. These locations are listed in Table 5.3.

Table 5.3: Radial locations of LVDTs on the soil surface for the tests on the end-bearing and semi-floating foundations

LVDT Label	Distance from Foundation (mm)
LVDT 1	0 (on foundation head)
LVDT 2	76.2
LVDT 3	91.6
LVDT 4	127.0

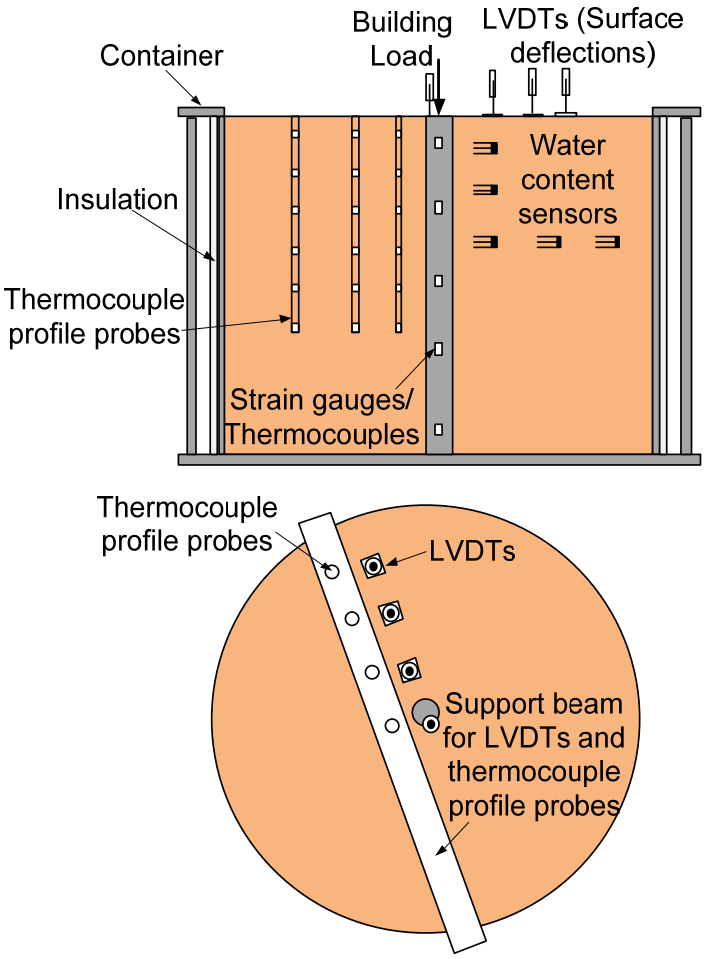

Figure 5.4: Schematic showing the approximate location of different instruments

5.2 Experimental Procedures

The section presents the testing procedures used for quantification of the strain distribution in energy foundations under a constant building load and cyclic thermal cycles. The same experimental testing program was repeated for the two model foundations (an end-bearing boundary condition and a semi-floating condition). Slight differences in testing procedures for the two different tests occurred due to problems with the LabView data acquisition program, instrumentation issues which had to be fixed in the middle of the test, and in the number of thermal cycles applied due to time restraints. These discrepancies are not shown in the schematics of the idealized experimental procedures.

A schematic of the procedures for the centrifuge tests on the semi-floating and end-bearing foundations is shown in Figure 5.5. The procedures follow five phases:

Phase 1: Spin-up and equilibration

Phase 2: Application of a building load and maintaining until strains and settlements of the foundation and soil surface to reach equilibrium

Phase 3: Heating of the foundation in increments, waiting for equilibration of strains and settlement to reach equilibrium after each change

Phase 4: Application of cooling-heating cycles to evaluate cyclic response.

Phase 5: Unloading, spin-down, and cool-down

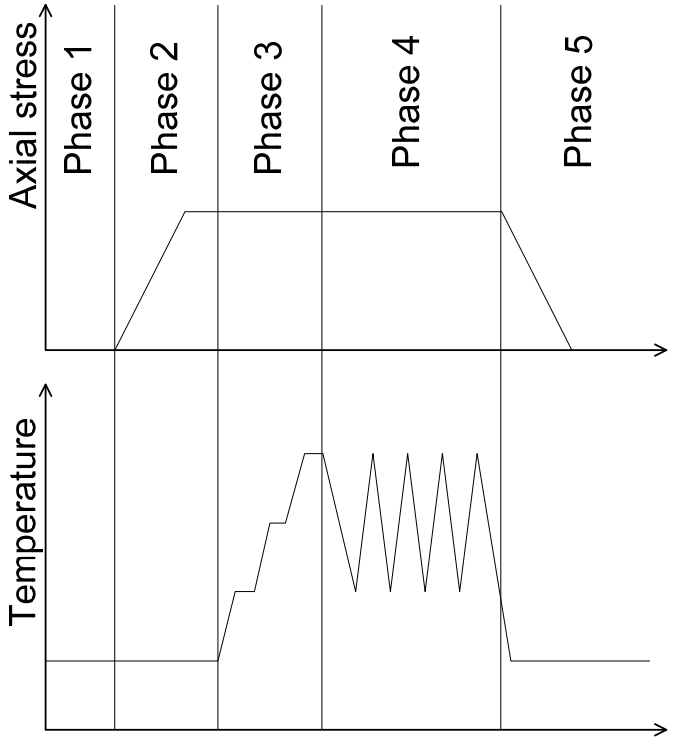

Figure 5.5: Schematic of testing procedures for the tests on the model foundations

In both tests, once the setup was placed on the centrifuge arm and the sensors were all attached to the data acquisition system, the centrifuge radial acceleration was ramped up at a until reaching a target g-level of 24 g's. Once the strain gages embedded in the foundation

reached equilibrium, model building loads of approximately 770 N for the end-bearing foundation and 330 N for the semi-floating foundation (corresponding to prototype axial stresses of 380 and 160 kPa, respectively) were applied to the heads of the foundations. Once the strain gages reached equilibrium under this axial load, heated fluid was circulated through the heat exchange tubes embedded in the foundation. The temperature at the center of the foundation was used as the representative temperature of the foundation as it is most affected by the insulating effects of the surrounding soil.

The temperature of the semi-floating foundation was increased in two increments up to approximately 40 °C. Each increment was maintained until the strain gages reached equilibrium. When the strain gages reached equilibrium under the maximum applied temperature of 40 °C, five cycles of passive cooling to 30 °C and reheating back to 40 °C were applied. The end-bearing foundation was heated to 42 °C in 6 °C increments. Once the thermocouple in the center of the foundation reached a temperature of 42 °C the center of the foundation was allowed to cool to 30 °C. The temperature was then applied again until a foundation temperature of 42 °C was obtained. After this, three more cycles of cooling to 30 °C and reheating to 42 °C were applied.

CHAPTER VI
Experimental Results

6.1 Calibration

6.1.1 Thermocouple Calibration

All thermocouples, including those embedded in the foundations, in the pipe-plug probes in the temperature control system, and in thermocouple profile probes, were calibrated by submerging them in a water bath of known temperature and fitting a line to actual vs. measured temperature data. The R^2 value for all corrections was 1.0. The equations obtained from these calibration tests showed a relatively small deviation of measures temperatures vs. actual temperature for all instrumentation. The calibration factors for the thermocouples in the foundation and in the thermocouple profile probes are presented in Appendix A.

6.1.2 Strain Gage Calibration

The measured strain values were first adjusted to compensate for the difference in coefficients of thermal expansion between the steel tabs the strain gages were attached to and the concrete surrounding the gages. This correction is applied as follows:

$$\varepsilon_{corrected} = (\alpha_c - \alpha_s) * \Delta T - \varepsilon_{uncorrected} \tag{6.1}$$

where $\varepsilon_{corrected}$ is the corrected strain, $\alpha_c = 7.5 \times 10^{-6}$ m/m°C and $\alpha_s = 8.25 \times 10^{-6}$ m/m°C are the coefficients of linear thermal expansion for concrete and steel, respectively, ΔT is the change in temperature and $\varepsilon_{uncorrected}$ is the raw measured strain. Application of Equation (6.1) also changes the sign of the strains to follow the geotechnical convention for strain magnitudes (positive strain is compression).

The corrected strain values were then adjusted to account for the thermal output error of the strain gage. This output strain occurs due to several changes that take place within the gage

during temperature changes. There is a tendency for the different components of the gage to expand/contract differentially, leading to a perceived strain. Further, the resistivity of the gage grid changes with temperature. The equation used to define the output strain error ε_{out} is unique for each batch of strain gages, and is defined as follows:

$$\varepsilon_{out} = a_0 + a_1 * T + a_2 * T^2 + a_3 * T^3 + a_4 * T^4 \quad (6.2)$$

where T represents the current temperature and a_0, a_1, a_2, a_3 and a_4 are unit-less thermal output coefficients supplied by the manufacturer, and the units of ε_{out} are microstrain (με). The values of these coefficients are summarized in Table 6.1, and a plot of the thermal output curve specific to the strain gages calculating these parameters and Equation 6.2 is presented in Figure 6.1. This plot indicates that the gage should give zero thermal output when it is used at an ambient temperature of 24.2 °C. The strain value used in analysis is obtained by subtracting Equation 6.2 from Equation 6.1.

Table 6.1: Thermal output coefficients for the strain gages used in this study

a_0	-24.2
a_1	2.37
a_2	-0.0654
a_3	0.000365
a_4	-0.000000412

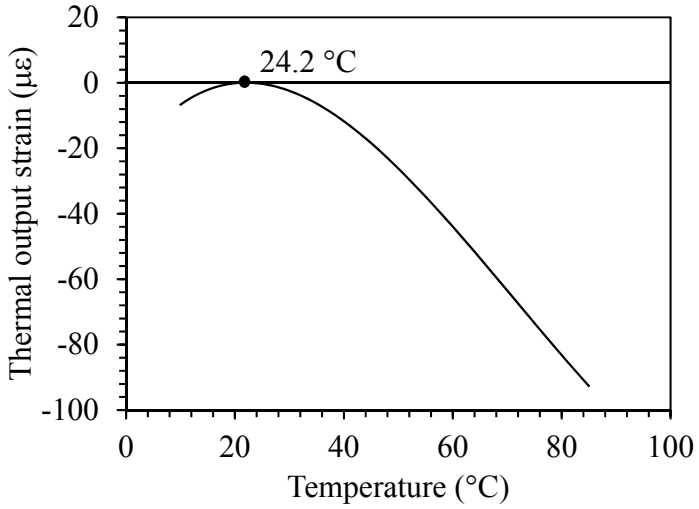

Figure 6.1: Thermal output curve specific to the strain gages used in this study

6.2 End-Bearing Foundation Data

This section presents the results from the tests performed on the end-bearing foundation. The definition of end-bearing in this case is a foundation which is allowed to expand axially only in the upper direction. The tip of the foundation is fully restrained as it is resting on a rigid substrate (the bottom of the container), while the top of the foundation is partially restrained by the loading system. All of the data time series are shown from the time shortly before starting the centrifuge. A breakdown of the times corresponding to each of the four phases is shown in Table 6.2. Centrifugation ended at a time of 18000 s, after which the foundation and soil was permitted to cool under ambient laboratory conditions.

Table 6.2: Timing of each of the phases in the test on the end-bearing foundation

Phase number	Ending time (s)
1	1875
2	2805
3	7700
4	18000

6.2.1 Temperature Data

The calibrated time-series data for the inlet, outlet and ambient temperatures is presented in Figure 6.2(a). The same data is shown in Figure 6.2(a) for the time during centrifugation. The changes in ambient temperature were caused by a warming of the air in the centrifuge chamber during spinning, with decreases in ambient temperature indicating a short period where the cooling system was utilized. Nonetheless, the variation in ambient temperature is relatively negligible. The inlet and outlet temperature depict a relatively constant difference of approximately 3 °C during testing. This difference reflects the heat loss into the foundation-soil system.

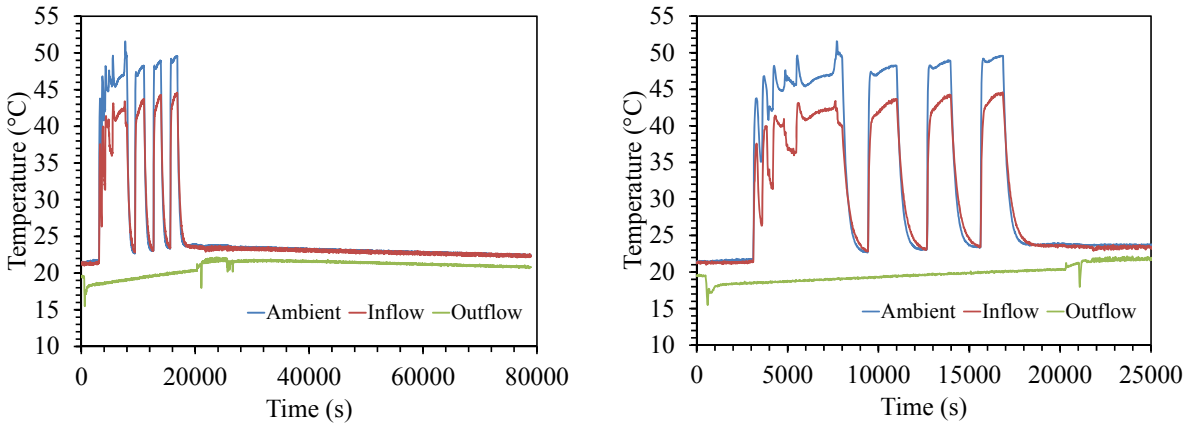

Figure 6.2: Inlet, outlet and ambient temperature data for the end-bearing foundation: (a) Entire testing sequence; (b) During centrifugation

The calibrated results from thermocouples embedded within the foundations are presenting in Figure 6.3(a) and 6.3(b), with the completely time series shown in Figure 6.3(a) and the data obtained during centrifugation only is shown in Figure 6.3(b). This data indicates consistency between thermocouples regarding time of response as well as magnitude.

There are some slight discrepancies between readings from the different thermocouples embedded in the end-bearing foundation. The thermocouple closest to the tip of the foundation showed a quicker cooling response when the heated fluid was not circulated through the foundation. This is likely due to the thermocouple's proximity to the bottom of the container where the heat transfer through the metal of the container base may lead to heat loss. The thermocouples in the middle of the foundation were affected by the insulation effect of the soil.

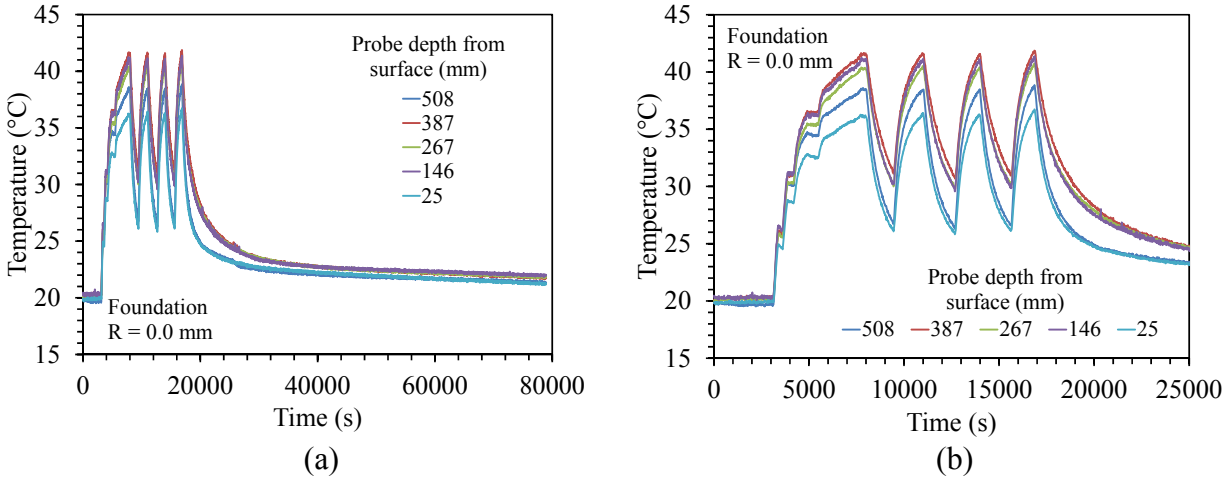

Figure 6.3: Temperature data from thermocouples embedded within the end-bearing foundation: (a) Entire testing sequence; (b) During centrifugation

The data from the thermocouple profile probes for the end-bearing foundation test are shown in Figures 6.4(a) through 6.4(d). A response to both stages of thermal changes can be observed in Figure 6.4(a), with a single wave of heat propagation noted in Figures 6.4(b) through 6.4(d). The difference between the 3 probes farthest from the foundation is noted in terms of both time of response and magnitude.

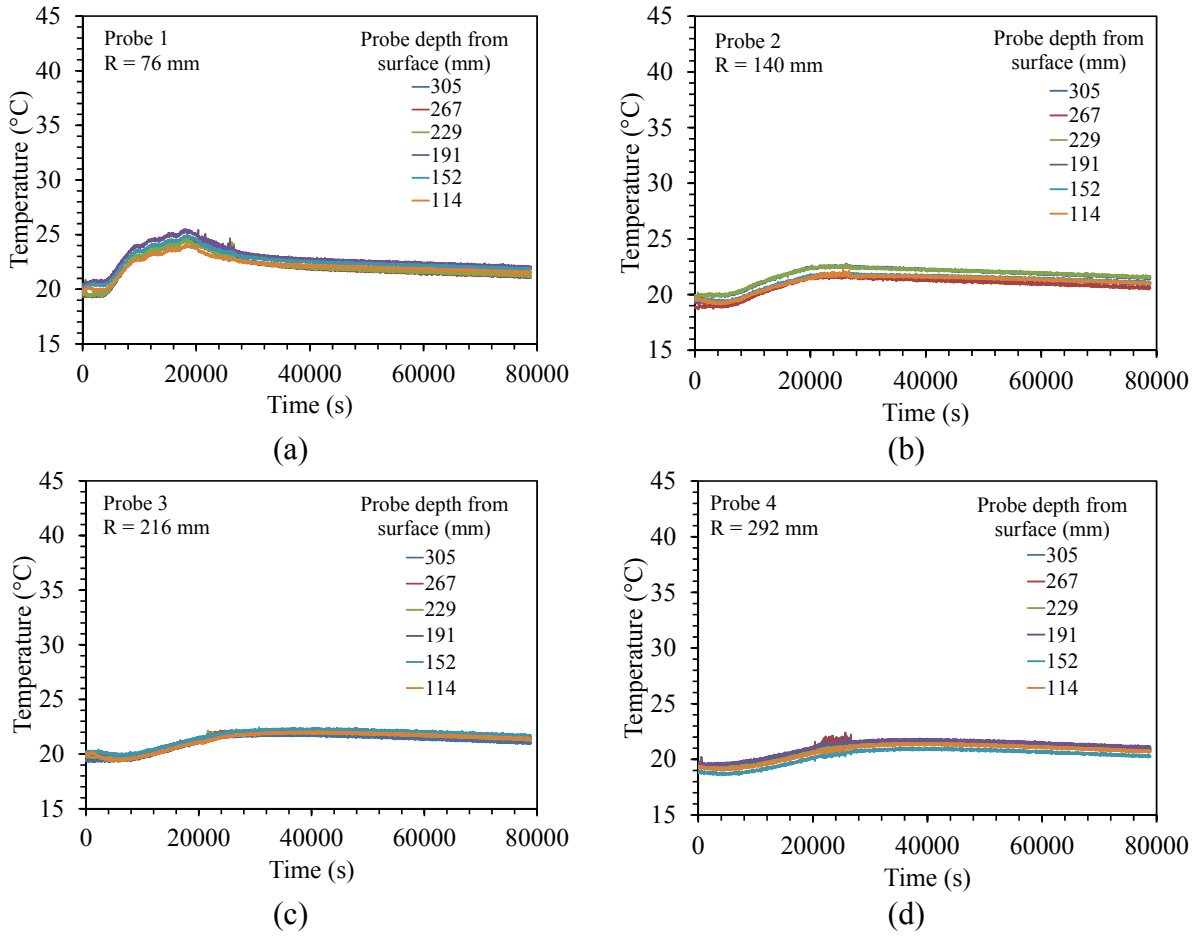

Figure 6.4: Temperature data in the soil at various radial locations from the end-bearing foundation: (a) 76 mm; (b) 140 mm; (c) 216 mm; (d) 292 mm

Temperature profiles for the end-bearing test are presented in Figure 6.5. These profiles indicate a relatively uniform change in temperature along the length of the foundation though lower temperatures are measure at the ends of the foundation. This slight difference is due to the lack of insulation at this point as opposed to the middle of the foundation where more soil cover is present. Profiles from the thermocouple probes are shown in Figures 6.6(a) through 6.6(d). This data indicates a relatively uniform soil heating response along the length of the probe at each radial location.

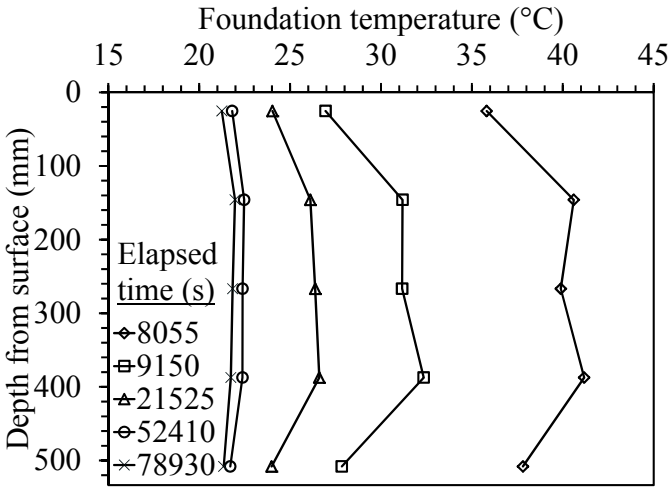

Figure 6.5: Temperature profiles for end-bearing foundation at different testing times

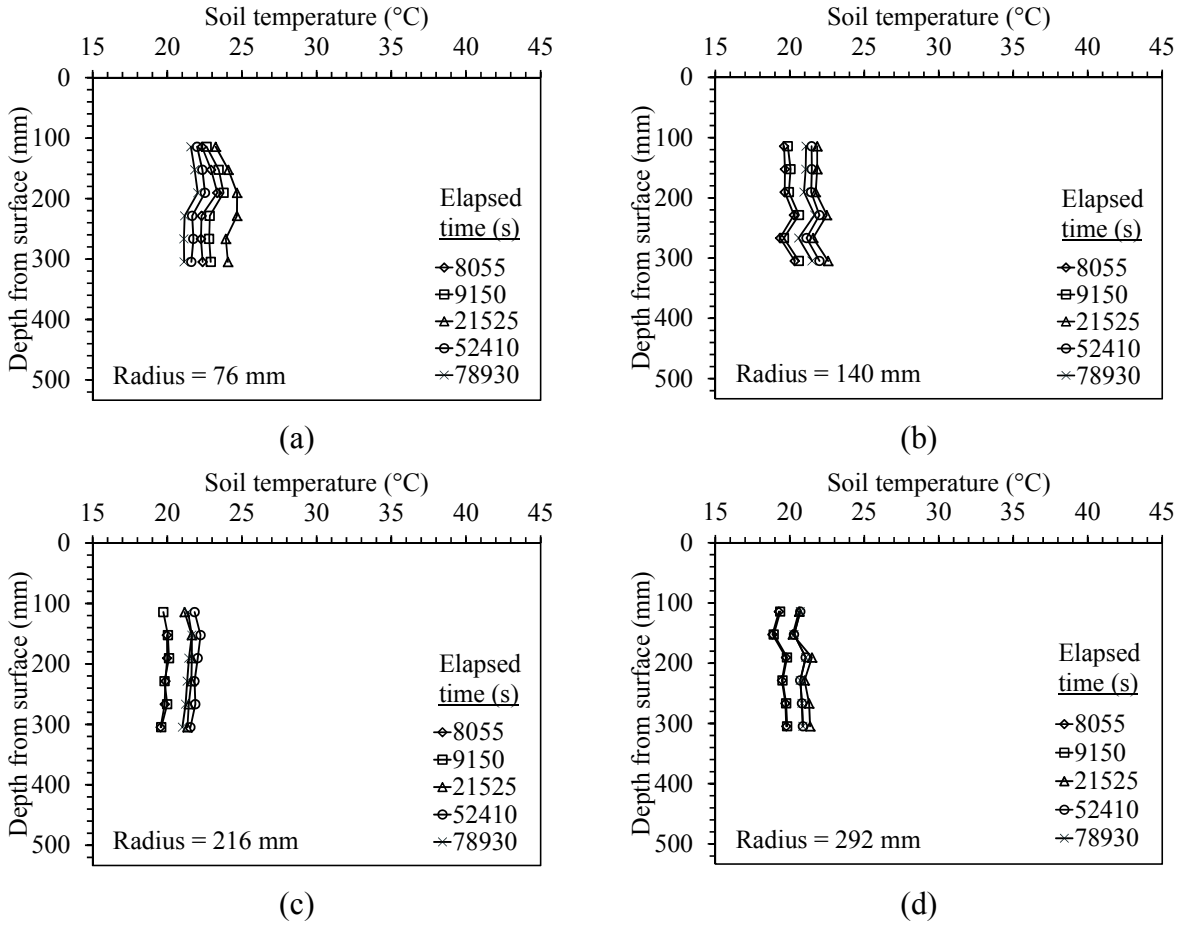

Figure 6.6: Temperature profiles in the soil at different radial locations from the end-bearing foundation: (a) 76 mm; (b) 140 mm; (c) 216 mm; (d) 292 mm

6.2.2 Results from Dielectric Sensors (Temperature and Volumetric Water Content)

Dielectric sensors were utilized in the soil mass surrounding the foundation to measure both changes in volumetric water content and changes in temperature at discrete location. Results from these sensors are shown in Figures 6.7(a) through 6.7(d). The change in volumetric water content in the vertical direction is shown in Figure 6.7(a). Although the dielectric sensor nearest the surface indicates that the soil remains at a lower water content throughout the test, the trend in volumetric water content observed by all 3 sensors is the same. An increase in volumetric water content is noted during the heating process, after which it decreases. A time-series plot of the variation in temperature at these locations is shown in Figure 6.7(b), and indicates that the temperature variation follows the same behavior as noted in the thermocouple profile probe data. Specifically, the soil changed in temperature uniformly with depth away from the foundation. A time-series plot of the variation in volumetric water content at varying distances from the foundation is shown in Figure 6.7(c). Although all three sensors respond, only the sensor closest to the foundation shows a significant change in water content. The change in temperature at each of the different radial locations is shown in Figure 6.7(d). The most sensitive response to temperature change in the foundation was noted closest to the heat source with changes beyond that being fairly uniform.

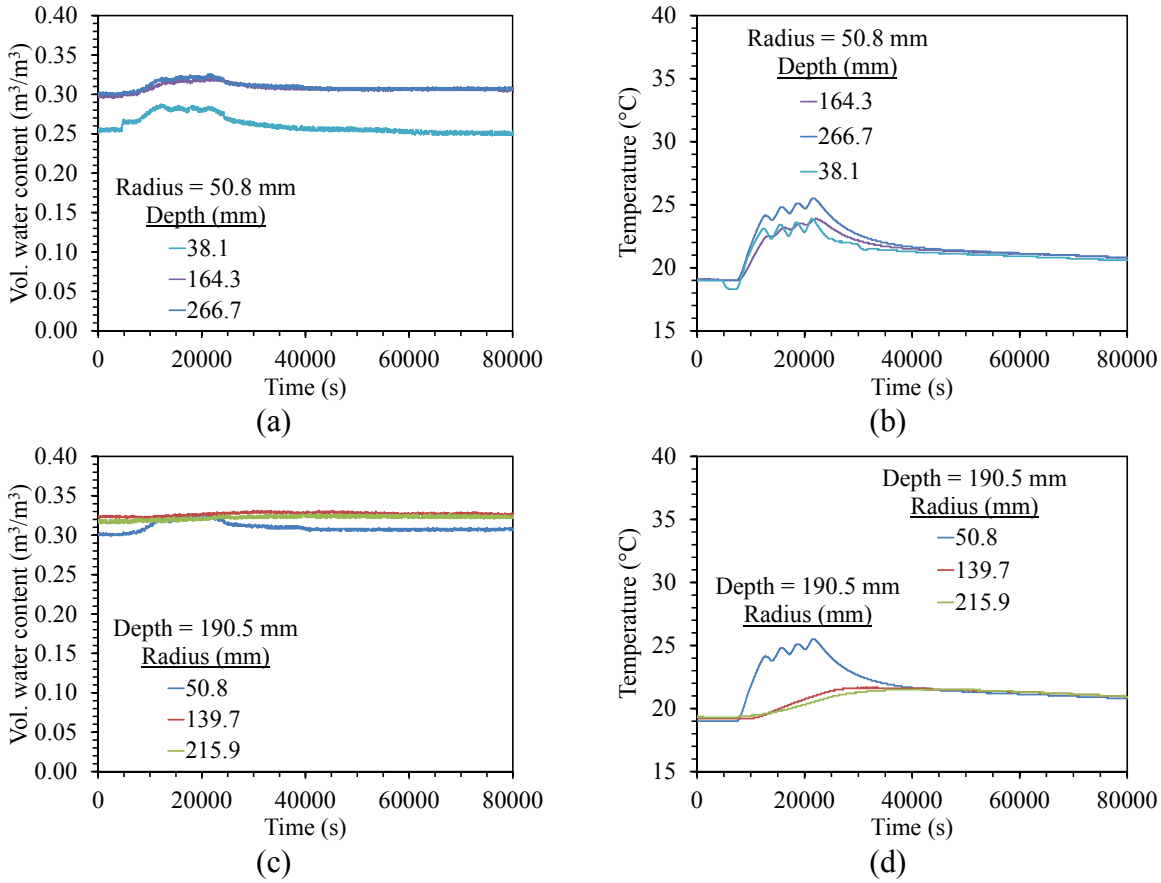

Figure 6.7: Data from the EC-TM dielectric sensors embedded in the soil layer for the end-bearing foundation test: (a) Volumetric water content varation from the sensors in the vertical array; (b) Temperature variation from the sensors in the vertical array; (c) Volumetric water content varation from the sensors in the horizontal array; (d) Temperature variation from the sensors in the horizontal array

6.2.3 Load and LVDT Response

A time-series plot of temperature changes and mechanical stresses applied to the foundation is shown in Figure 6.8. These values are shown together to display the two mechanisms by which displacements in the foundation could occur. The results from the LVDTs placed at the soil surface as well as the single LVDT placed directly onto the foundation head are shown in Figure 6.9. The LVDTs on the soil surface show a slight settlement throughout the test, which indicates that the soil layer may not have been in complete equilibrium. However, the majority of the settlement occurs after spin-up and the amount of consolidation is not significant.

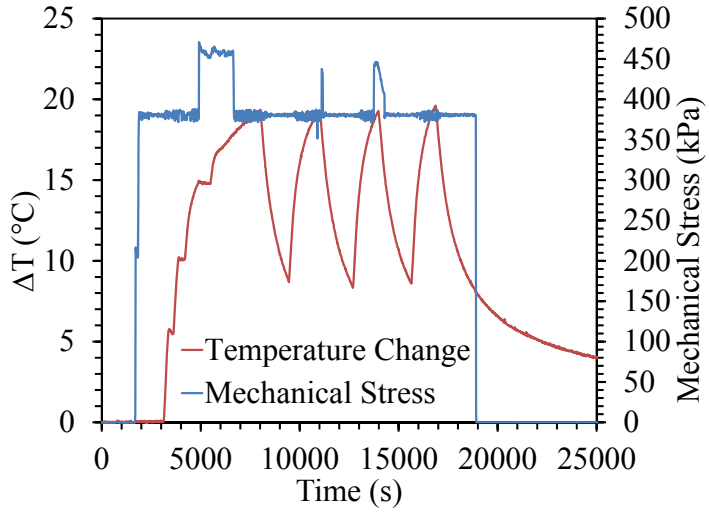

Figure 6.8: Time series of temperature change and mechanical loading for the end-bearing foundation during centrifugation

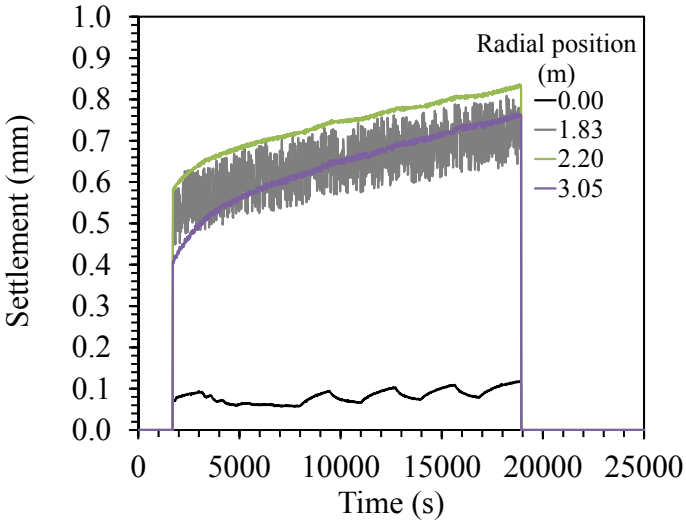

Figure 6.9: Time series of settlement at various radial distances from the end-bearing foundation during centrifugation

A comparison of the LVDT displacement at the foundation head and the applied mechanical axial stress is shown in Figure 6.10(a). A positive LVDT reading indicates downward movement of the foundation head. The LVDT shows a slight downward movement (compression) during spin-up of the centrifuge and mechanical loading. Similarly, a comparison of the response of the LVDT with the temperature of the middle of the foundation is shown in Figure 6.10(b). This

figure indicates that the foundation moved upward (expansion) during heating, which is expected. The movement of the foundation head was also evaluated by converting motor position in the loading system into vertical displacement, which is shown in Figure 6.11 with the LVDT data. The motor position data confirms the observations obtained from the LVDT.

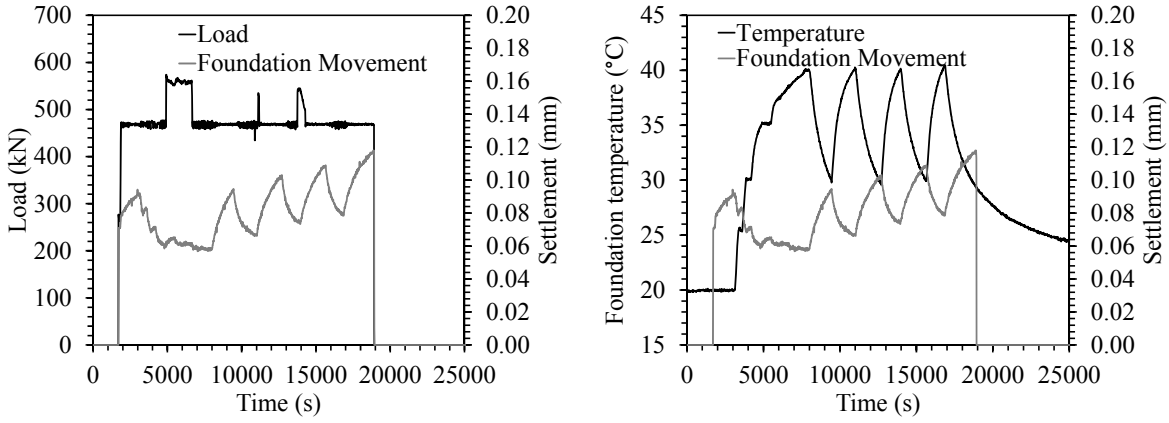

Figure 6.10: Prototype-scale time series of vertical position inferred from the LVDT on the foundation head with: (a) Axial load; (b) Temperature at center of foundation

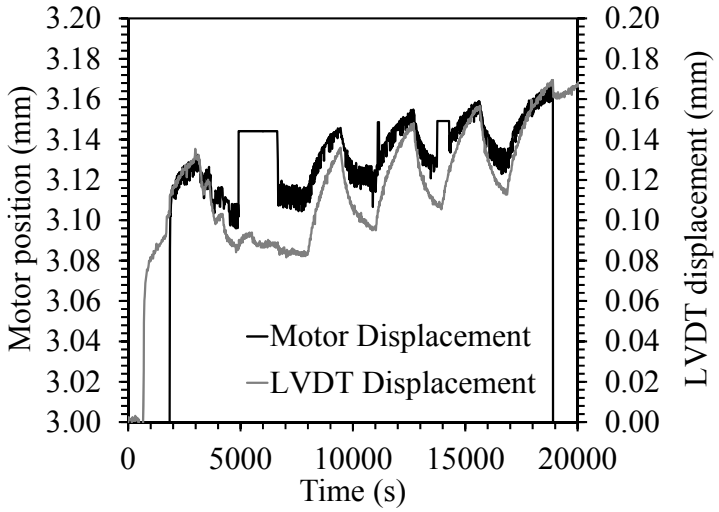

Figure 6.11: Comparison of motor position with LVDT measurement

6.2.4 Strain Gages

There were a total of ten strain gages embedded in the end-bearing foundation, with two strain gages at each depth. The strains measured at each of these locations with both gages are shown in Figure 6.12. This data was used to identify which strain gages were responding

correctly and ultimately was used to determine which gage data would be included in the analysis. Some of the strain gages showed a drastically different response that those on the other side of the foundation, which may have been due to poor bonding with the metal tab, or eccentric thermo-mechanical loading of the foundation. The strain data for the gages embedded at a depth of 508 mm is shown in Figure 6.12(a). For this depth it was determined that Gage 1 would be used in the analysis since Gage 1t did not respond as expected under the initial mechanical load (tensile strains measured when compressive axial loads applied). For the strains measured at a depth of 387.4 mm it was determined that the response of Gage 2 was well outside of the magnitude expected based on the coefficient of thermal expansion of the foundation and therefore data from Gage 2t was used. The same logic was applied to the gages embedded at a depth of 266.7 mm [Figure 6.12(c)], where only the data collected from Gage 3 was used. The data shown in Figure 6.12(d) suggests that Gage 4 responded opposite what was physically probable for this test, possibly due to being wired in an opposite convention than other strain gages. Therefore only the data for Gage 4t was used in the analysis for the embedment depth of 146 mm and its sign was reversed. At a depth of 25.4 mm from the ground surface only Gage 5t responded as expected until the initial axial load so only the data from this gage were utilized in the analysis of the foundation at that depth.

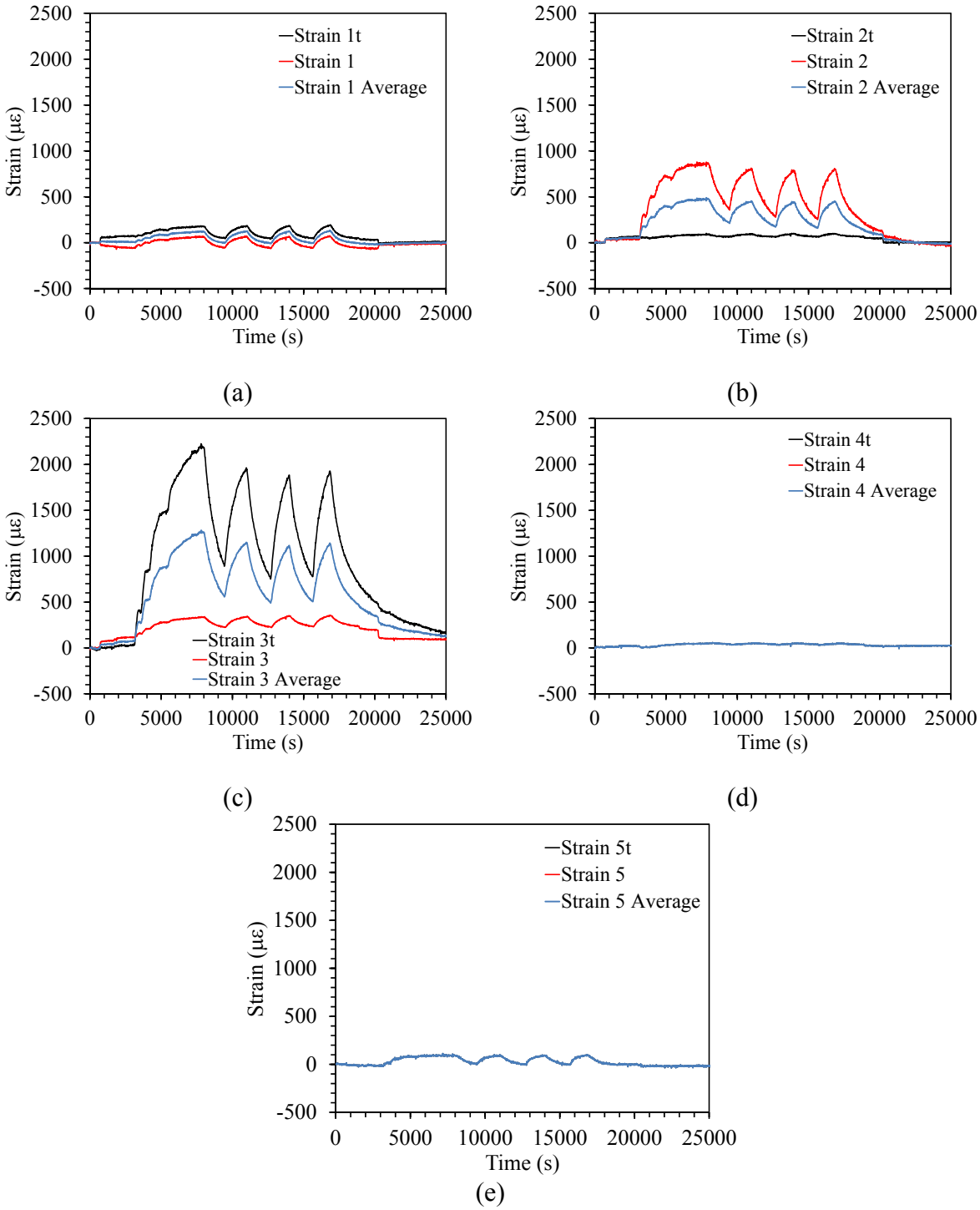

Figure 6.12: All strain gage data for the pair of strain gages embedded at each depth: (a) 508 mm; (b) 387.4 mm; (c) 266.7 mm; (d) 146 mm; (e) 25.4 mm (Note: "t" designates that a thermocouple is next to the strain gage)

The total uncorrected time series for all working strain gages are presented in Figure 6.13(a) while the corrected data is shown in Figure 6.13(b). The corrections applied to this data was discussed in earlier sections of this chapter and includes mechanical corrections based on 1g tests, differential correction to account for a different in thermal conductivity within the system and corrections applied to remove thermal output error associated with the gages from the data. Some of the gages do not provide a reasonable reading under low mechanical stresses (i.e., negative strain response during compression). However, the thermal strain is a more important variable than the mechanical strain for this study. It can be defined after zeroing the strain gages at the moment when temperature changes are applied. The adjustment factors in Table 4.3 were applied to the strain time series. The thermal strains are shown in Figure 6.13(c), indicating a consistent compressive response during heating. The top of the foundation was found to show the greatest strains in the foundation, which is expected at the top of the foundation was permitted to move freely while maintaining a constant stress at the top.

Comparison of the strains measured during mechanical loading with those measured during thermal loading indicates that the results are representative of field measurements. Specifically, Bourne-Webb et al. (2009) found that a full-scale energy foundation which was in effect restricted at both ends showed a maximum axial stress during heating which was 70% greater than that observed due to mechanical loading. Because the strains are not constant with length along the foundation, soil-structure interaction can be attributed to be the cause of the non-uniform distribution in strain with depth. The strain profiles with depth will be discussed in the next chapter.

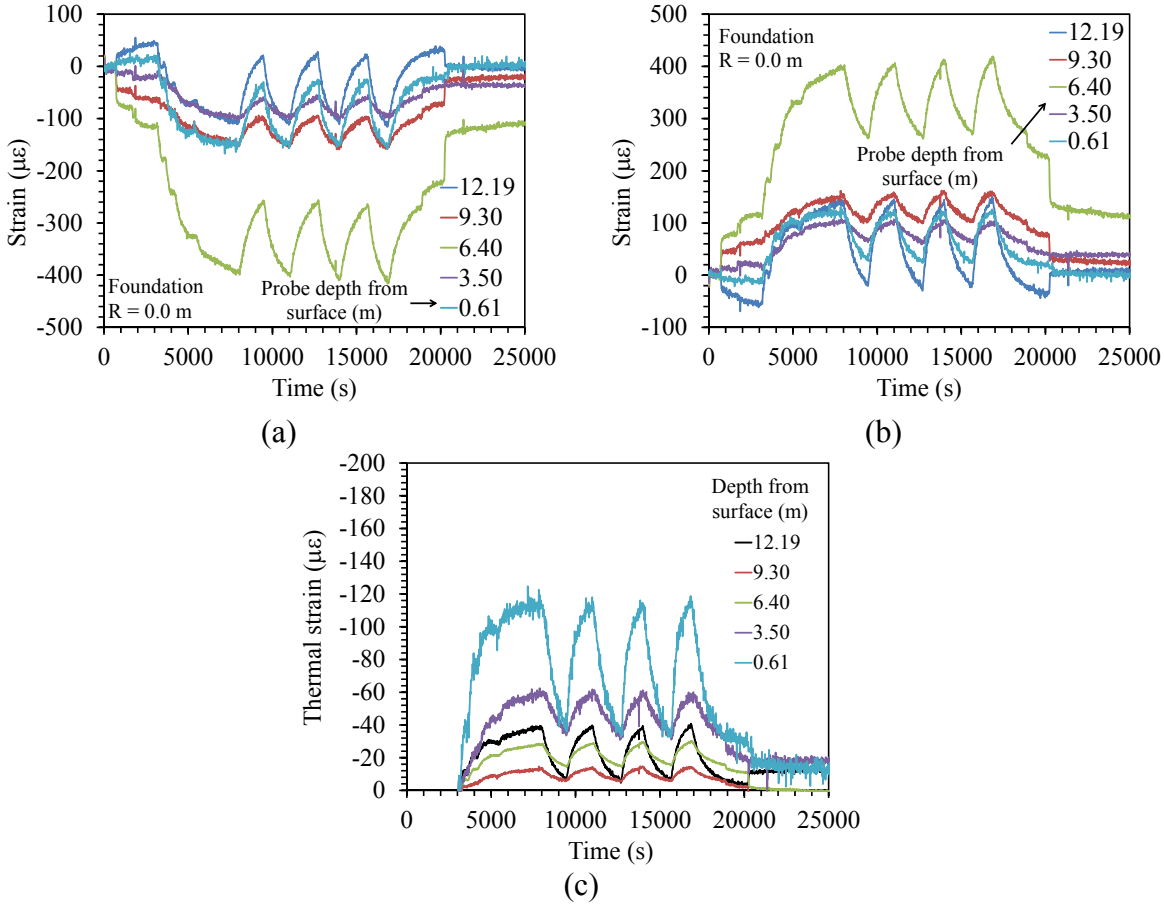

Figure 6.13: Strain data for end-bearing foundation collected from strain gauges embedded in model foundation (dimensions in prototype scale): (a) Raw measurements (tensile = positive); (b) Corrected thermo-mechanical strains; (c) Corrected thermal strains

6.3 Semi-floating Foundation

This section presents all data recorded for the centrifuge test involving the semi-floating model foundation. The definition of semi-floating in this case is a foundation which is allowed to expand axially in both directions. The bottom of the foundation is partially restrained by the compacted Bonny silt below the tip of the foundation, while the top of the foundation is partially restrained by the loading system at the head of the foundation. All of the data time series are shown from the time shortly before starting the centrifuge. A breakdown of the times corresponding to each of the four phases is shown in Table 6.3. In this test centrifugation ended after 17000 s, after which the foundation

Table 6.3: Timing of each of the phases in the test on the semi-floating foundation

Phase number	Ending time (s)
1	1920
2	5220
3	8415
4	17000

6.3.1 Temperature Data

During the specimen preparation phase of the semi-floating test, the intention was to compact the Bonny silt as dense as possible to result in maximized degree of saturation, water flow and temperature flow through the specimen. Unfortunately, the soil was compacted so dense that thermocouple profile probes could not be inserted into the soil surrounding the foundation. Nonetheless, the trends are expected to be similar to the thermocouple profile probes installed in the end-bearing test, and the embedded EC-TM dielectric sensors provided a backup measurement of temperature changes in the soil.

The calibrated time-series data from the thermocouples used to measure the inlet, outlet and ambient temperatures is shown in in Figure 6.14(a) with an accompanying plot of the more relevant time period during centrifugation is presented in Figure 6.14(b). The slight changes in ambient temperature were caused by a warming of the air in the centrifuge chamber during spinning. Nonetheless, the changes in ambient temperature are negligible. The inlet and outlet temperature differences indicate that approximately 4 °C of temperature change was lost through the foundation-soil system during testing.

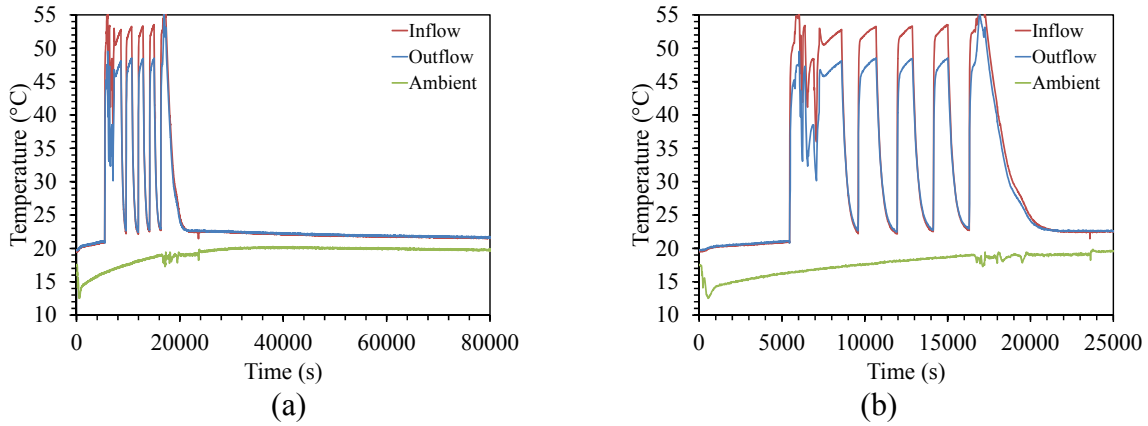

Figure 6.14: Inlet, outlet and ambient temperature data from semi-floating foundation test: (a) Entire testing sequence; (b) During centrifugation

The calibrated results from thermocouples embedded within the foundation are shown in Figures 6.15(a) and 6.15(b), with the complete time series shown in Figure 6.15(a) and an accompanying plot of the time period during centrifugation are presented in Figure 6.15(b). The data indicates a relatively consistent response of the embedded thermocouples regarding both time of response and magnitude.

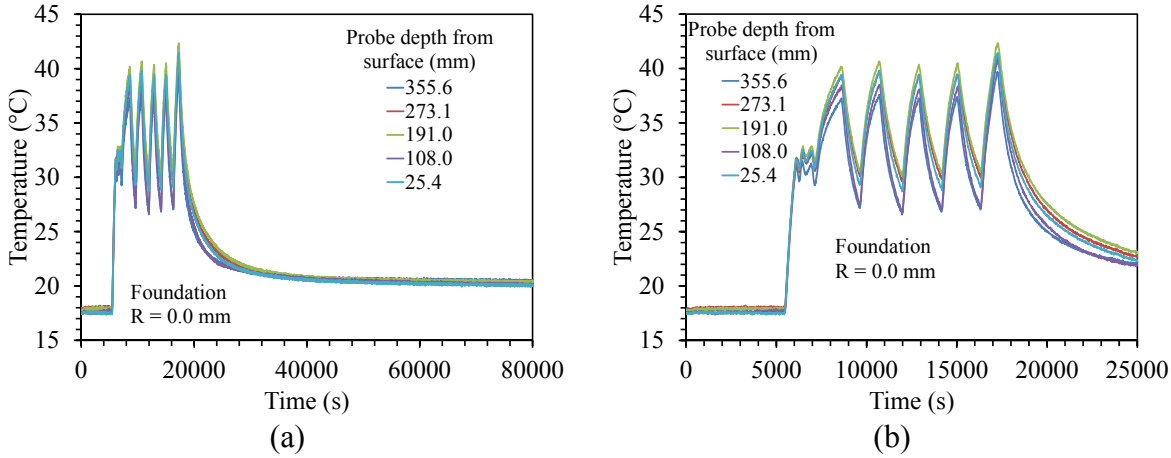

Figure 6.15: Temperature data for end-bearing foundation collected from thermocouples embedded in model: (a) Entire testing sequence; (b) During centrifugation

Foundation temperature profiles for different times throughout the test are presented in Figure 6.16. These profiles indicate uniform heating of the foundation during the test with slight variation that could be due to the U-tube location relative to the embedded thermocouples.

These results indicate that the foundation should have a relatively uniform tendency to expand or contract during heating or cooling.

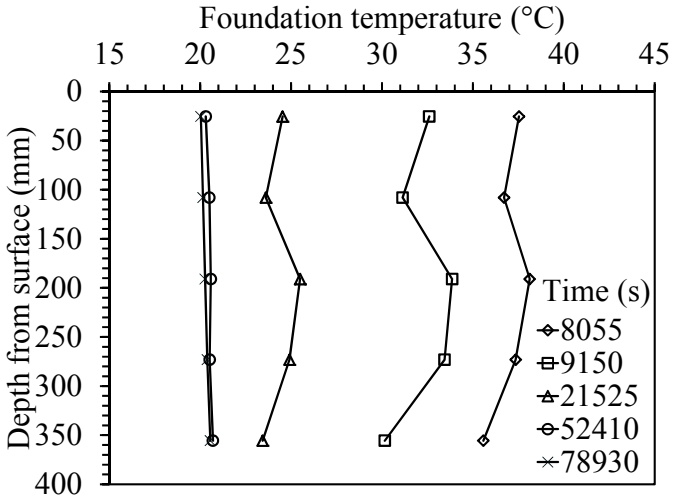

Figure 6.16: Temperature profiles for semi-floating foundation collected from thermocouples embedded in model foundation

6.3.2 Dielectric Sensor Results (Temperature and Vol. Water Content)

Similar to the end-bearing foundation, dielectric sensors were placed in the soil mass surrounding the semi-floating foundation to quantify the water flow and temperature changes at discrete locations. Results from these sensors are shown in Figures 6.17(a) through 6.17(d). Time series of the changes in volumetric water content for sensors at three different depths are shown in Figure 6.17(a). The 2 dielectric sensors nearest the ground surface maintain lower water content values throughout the test. The sensor placed at the center of the foundation exhibits in increase in water content as the topmost sensors are beginning to dry. A time-series plot of changes in temperature as measured by the dielectric sensors for the same three depths is shown in Figure 6.17(b). The horizontal changes in water content and temperature were measured by dielectric sensors at different radial locations away from the foundation. The results from these sensors are presented in Figures 6.17(c) and 6.17(d). A movement of water away from the foundation can be observed in Figure 6.17(d), where the dielectric sensor closest

to the foundation indicates in increase in water content, followed by a drying period with the other two sensors following in suit after a slightly delayed response. The thermal response of the soil at varying radial location exhibits the same trends at the water content changes and is presented in Figure 6.17(d). The sensor closest to the foundation exhibited the most notable temperature increase and subsequent decrease while the sensors farther out from the heat source showed a delayed increase in temperature and a much slower rate of cooling.

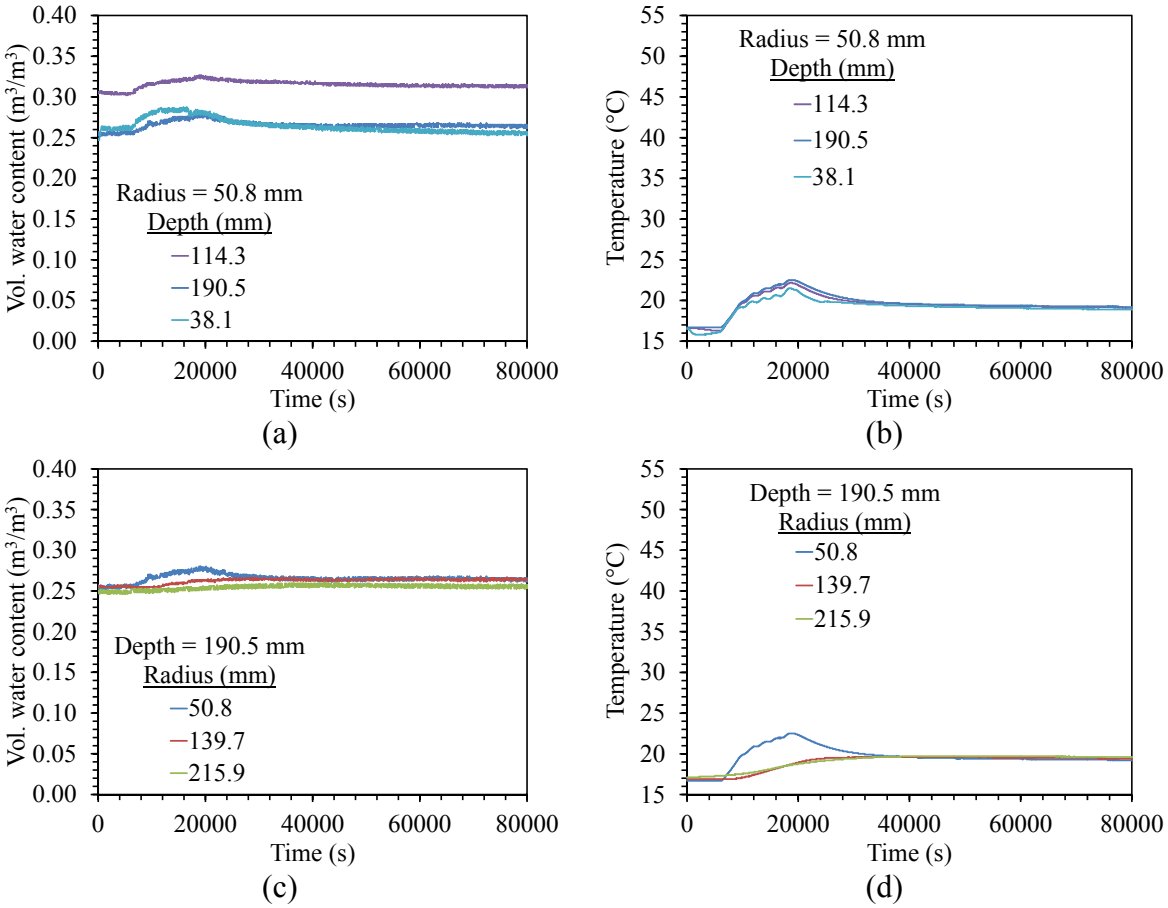

Figure 6.17: Data from the EC-TM dielectric sensors embedded in the soil layer for the semi-floating foundation test: (a) Volumetric water content varation from the sensors in the vertical array; (b) Temperature variation from the sensors in the vertical array; (c) Volumetric water content varation from the sensors in the horizontal array; (d) Temperature variation from the sensors in the horizontal array

6.3.3 Mechanical Axial Stress and LVDT Response

Time-series of temperature change and mechanical axial stress are shown in Figure 6.18(a), including cool-down data when load was removed and centrifuge spin-down occurred. An accompanying plot showing only the data during centrifugation is presented in Figure 6.18(b). The large spike in mechanical stress was due to a brief shutdown in the load control system. The problem was fixed and testing was continued at the previous mechanical axial stress. This increase in stress was found to lead to a recoverable strain in the foundation, without a permanent effect. This spike occurred during the first temperature increment, and the strains in the foundation were allowed to re-equilibrate before moving to the second temperature increment.

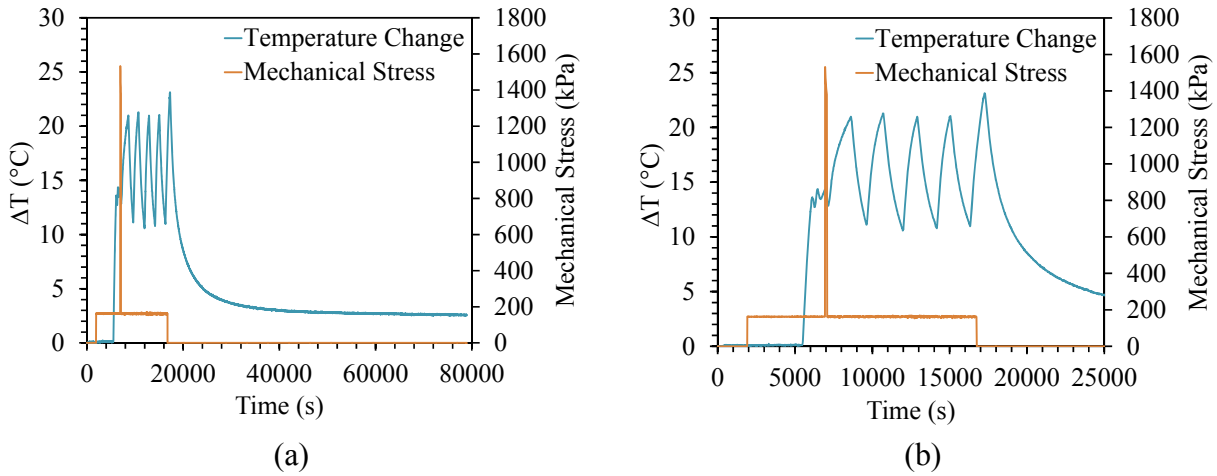

Figure 6.18: Time series of temperature change and mechanical axial loading for semi-floating foundation: (a) Entire testing sequence; (b) During centrifugation

LVDTs were placed at the soil surface as well as directly on the foundation head to measure thermo-mechanical axial displacements. Time series of the four LVDTs readings for the semi-floating foundation test during centrifugation are shown in Figure 6.19. LVDT 1 is on the foundation, and the other three LVDTs are on the soil surface at increasing radial distances from the foundation. All four LVDTs were affected by the spike in the mechanical load after 7500 s,

possibly because the load cell brushed against the support beam for the LVDTs. The foundation LVDT shows the least amount of settlement of the four LVDTs, even though the greatest settlement was expected. The other three LVDTs showed a distinct settlement throughout the test, which may indicate that there was either continued consolidation of the soil, or that the gripping mechanisms for these LVDTs were creeping throughout the test. The foundation LVDT was secured with a clamp, so this may explain the difference in behavior between the four foundation and soil LVDTs.

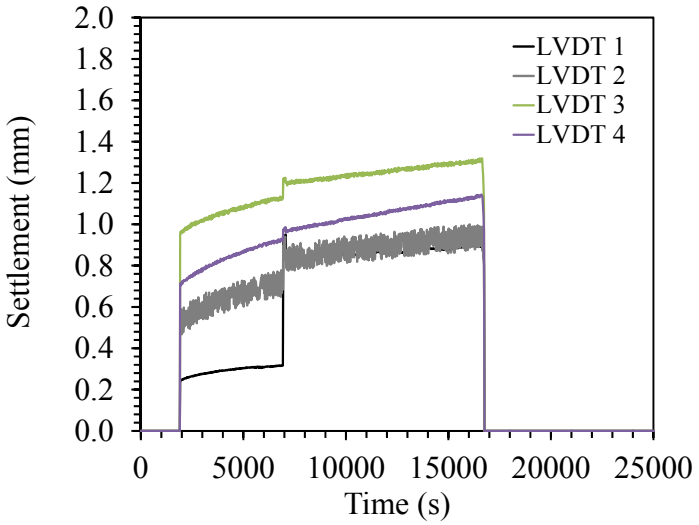

Figure 6.19: Time series of settlement for various radial distances from semi-floating foundation during centrifugation

A time-series plot of foundation head position as measured by the LVDT and mechanical stress is presented in Figures 6.20(a). The unexpected spike in the building load appeared to have caused the foundation to displace into the soil almost $1/10^{th}$ of a cm. Although this displacement of the foundation into the soil could have caused the soil under the foundation to become denser, the mechanical strains were found to be much smaller than the thermal strains. A time-series plot of the vertical position of the foundation head during varying thermal load plotted with the change in temperature of the foundation is shown in Figure 6.20(b).

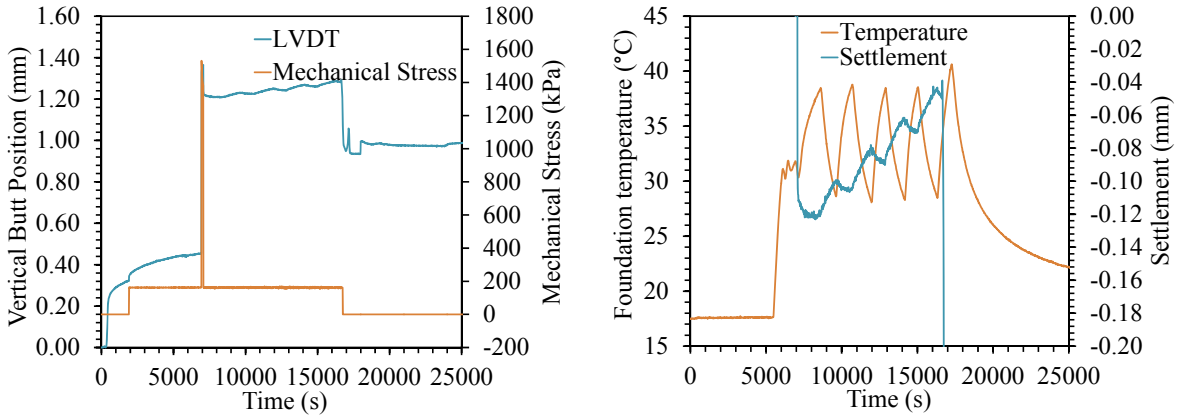

Figure 6.20: Time series of vertical displacement from the LVDT on the semi-floating foundation head: (a) With mechanical stress; (b) With temperature change

6.3.4 Strain Gages

As with the end-bearing foundation, a total of 10 strain gages were embedded in the semi-floating foundation, with two independent measurements of strain at each of 5 discrete depths in the foundation. Time series of the strains for each location are shown in Figures 6.21(a) through 6.21(e). This uncorrected data was used to determine which strain gage responded correctly and would be used in the analysis. The strain gage data for the depth of 355.6 mm is shown in Figure 6.21(a). The response of Gage 1 was much lower than is reasonable for the thermal changes and therefore the data collected from Gage 1t is used in this analysis. Gage 2 faded in and out of functionality throughout the test therefore Gage 2t was used for analysis at a depth of 273.1 mm. The data recorded at a depth of 190.5 mm from the top of the foundation is presented in Figure 6.21(c). The response of Gage 3 at a depth of 108 mm was lower than expected for the thermal changes applied to the foundation, therefore Gage 3t was considered for the analysis at this depth.

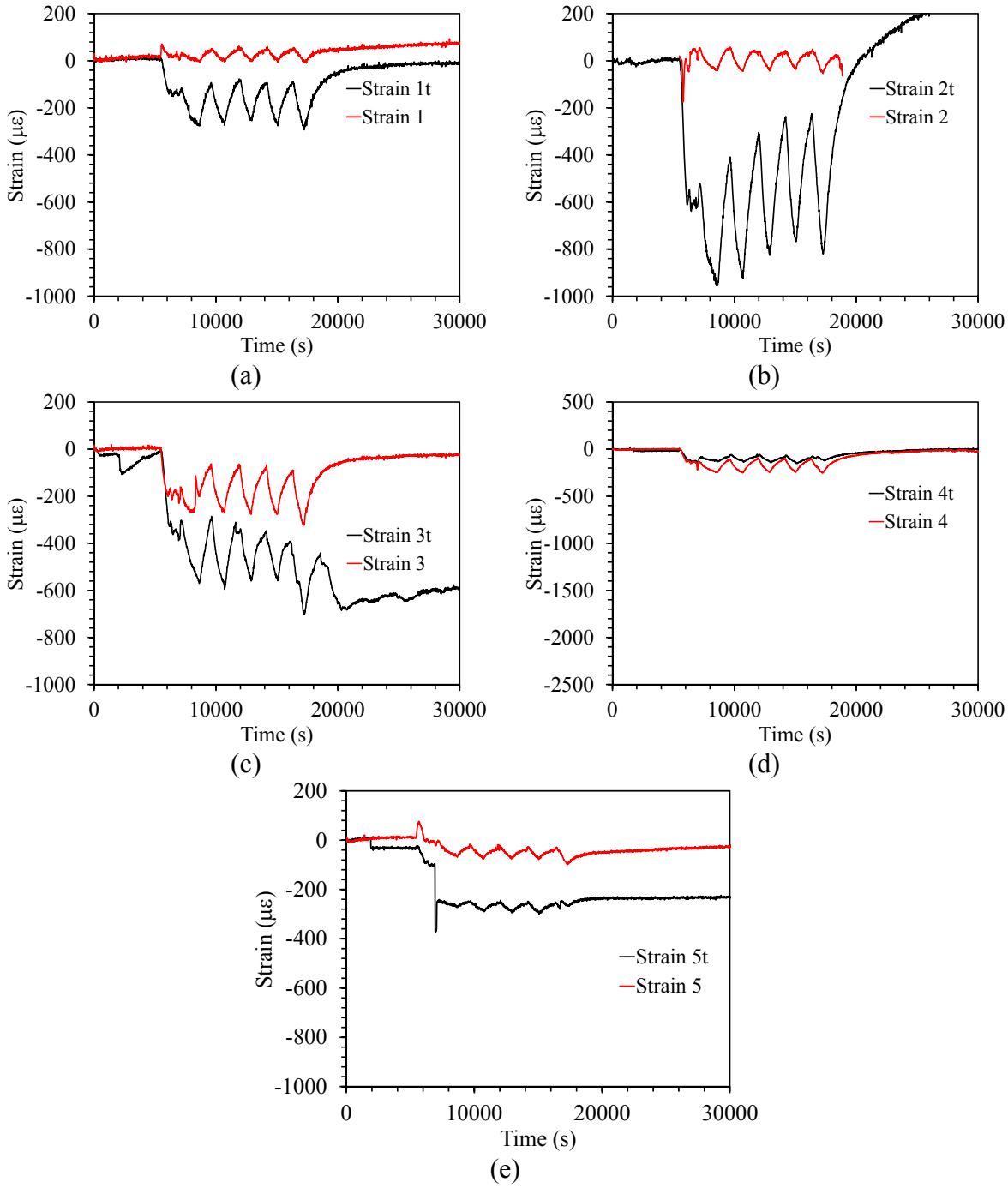

Figure 6.21: All strain gage data for the pairs of strain gages embedded at each depth: (a) 355.6 mm; (b) 273.1 mm; (c) 190.5 mm; (d) 108.0 mm; (e) 25.4 mm (Note: "t" designates that a thermocouple is next to the strain gage)

Data collected for a depth of 108.0 mm is presented in Figure 6.21(d). The magnitude of response of Gage 4t is well below what would be expected for the thermal load being applied

and therefore the data from Gage 4 was used for analysis at this depth. Data for a depth of 25.4 mm is presented in Figure 6.21(e). The results indicate that Gage 5t stopped responding at the beginning of temperature changes in the foundation. Although the gage appears to have recovered by the second heating cycle, it was decided that Gage 5 would be used in the analysis.

The uncorrected time-series plot for all working gages is presented in Figure 6.22(a), while the corrected time-series data is shown in Figure 6.22(b). As with the end-bearing condition, this data was corrected for the differential expansion error due to the difference in the coefficient of thermal expansion for the strain gages and the foundation and for the thermal output error unique to each batch of gages and supplied by the manufacturer. The thermal strains presented in Figure 6.22(c) were zeroed once temperature changes were applied to the system to define the thermal strains without the mechanical strains included.

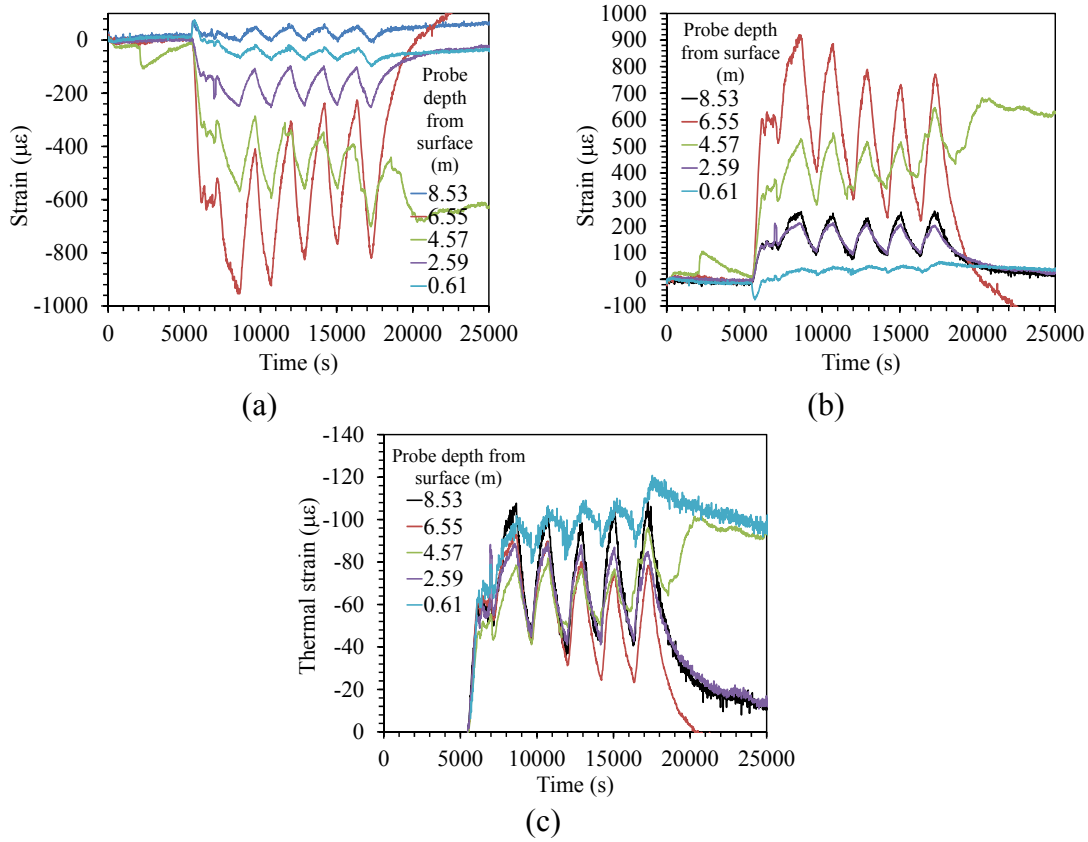

Figure 6.22: Strain data for the semi-floating foundation collected from strain gages embedded in model foundation: (a) Uncorrected; (b) Corrected; (c) Corrected thermal strains

CHAPTER VII
Analysis

7.1 Thermal Strains for Different Boundary Conditions

Time series of thermal strains for both foundation boundary conditions are shown in Figure 7.1, with data from the end-bearing foundation shown in Figure 7.1(a) and data from the semi-floating foundation shown in Figure 7.1(b). The temperature changes and mechanical stresses for these two foundations are shown in Figures 7.1(c) and 7.1(b) for reference. The movement of the foundation head inferred from the LVDT and motor position are shown in Figures 7.1(d) and 7.1(e) to highlight the external movement of the foundations.

An interesting aspect of the strain data is that the measured thermal strains are compressive during heating. It is expected that during heating of the foundation, it would tend to expand. To confirm this expectation, the LVDTs on top of the foundation indicate that the foundation expands during heating. However, the strain gages, which are supposed to show a physical movement, do not show expansion. This observation was also observed in the strain gage data reported by Bourne-Webb et al. (2009) and Laloui et al. (2006). This observation is possibly due to relative expansion of the different materials in the strain gage, including the gage itself, the steel tab, and the concrete. It is possible that the steel tab wanted to expand slightly more than the concrete, and this put the steel tab into compression. Alternatively, if the steel is constrained from moving by the differential expansion of the concrete, the strain gage may have still wanted to move, leading to a compressive strain reading. Although the author believes that the measurements from this study are correct and were carefully obtained, the conversion of these strains into stresses is not simple. Further research into the differential expansion of the different components is necessary to understand the conversion of thermal strains to thermal stresses.

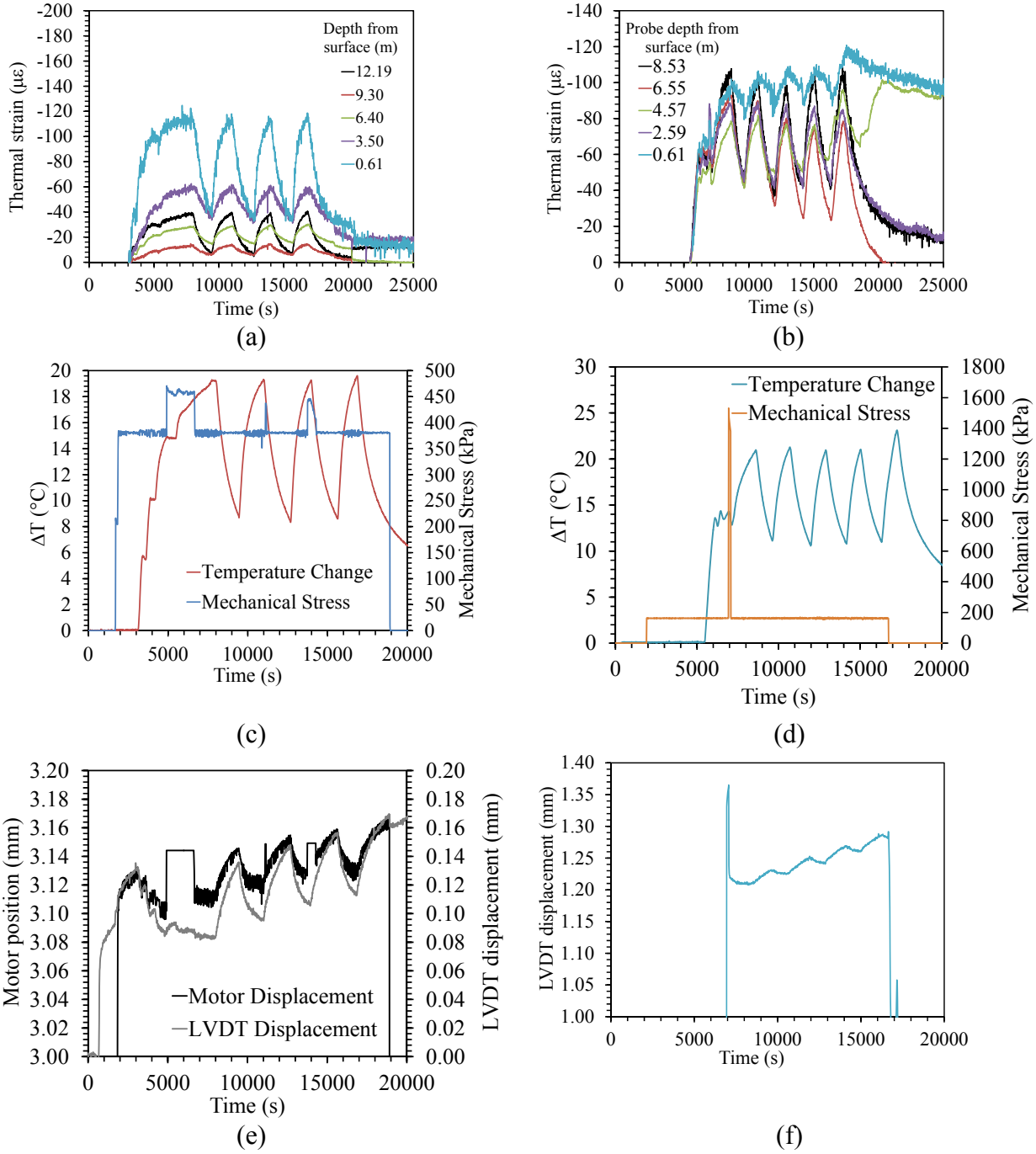

Figure 7.1: Time-series for energy foundations with different boundary conditions: (a) thermal strains for the end-bearing foundation; (b) thermal strains for the semi-floating foundation; (c) temperature change and mechanical stress for the end-bearing foundation; (d) temperature change and mechanical stress for the semi-floating foundation; (e) head displacement for the end-bearing foundation; (f) head displacement for the semi-floating foundation

When evaluating the strain measurements in Figures 7.1(a) and 7.1(b), it is useful to evaluate the maximum and minimum thermal strains expected in a test. At most, the foundation is expected to expand by an amount equal to:

$$\varepsilon_{T,free} = \alpha \Delta T \tag{7.1}$$

where α is the coefficient of thermal expansion of the foundation. If the foundation expands freely, no thermal stresses are expected to be generated in the foundation. If the foundation is fully constrained by the boundaries, it would be expected that the thermally induced stress would be equal to:

$$\sigma_{T,constrained} = E\alpha\Delta T \tag{7.2}$$

Because the foundations in this study were neither freely restrained nor fully constrained, it is likely that the strains measured and the stresses induced during heating are a mix of these two limit states. The thermal axial stress can be defined as follows for this case:

$$\sigma_T = E(\alpha\Delta T - \varepsilon_{T,corrected}) \tag{7.3}$$

Thermal strain profiles for the end-bearing foundation are presented in Figure 7.2(a), while the thermal stress profiles calculated using Equation 7.3 are shown in Figure 7.2(b). Similar profiles for the semi-floating foundation are presented in Figures 7.2(c) and 7.2(d). If the side shear resistance was constant with depth and the foundation were allowed to expand freely axially, then compressive stresses would be expected at the center of the foundation, with the largest magnitude at the center of the foundation (the null point) (Bourne-Webb et al. 2009). Although the soil was compacted into a relatively dense and uniform state, which would indicate that the soil should provide constant side shear resistance with depth (if thermal loading occurred in an undrained fashion), the ends of each foundation were not allowed to freely expand. At the top of each foundation a constant load applied offered some resistance to movement, even

though the loading system was programed to permit expansion and contraction to maintain a constant axial load. The tip of the end-bearing foundation was resting on the container bottom and was essentially fixed.

Different from the stress profiles predicted for floating boundary conditions, the strain profiles for the end-bearing foundation in Figure 7.2(a) indicate that the null point is closer to the bottom of the foundation. This indicates that the foundation has a stiffer resistance at the tip than the foundation head, which is expected at the loading system should provide a negligible resistance to movement (Plaseied 2012). The thermal stress profiles in Figure 7.2(b) indicate that heating leads to a doubling of the axial stress applied to the top of the foundation (439 kPa).

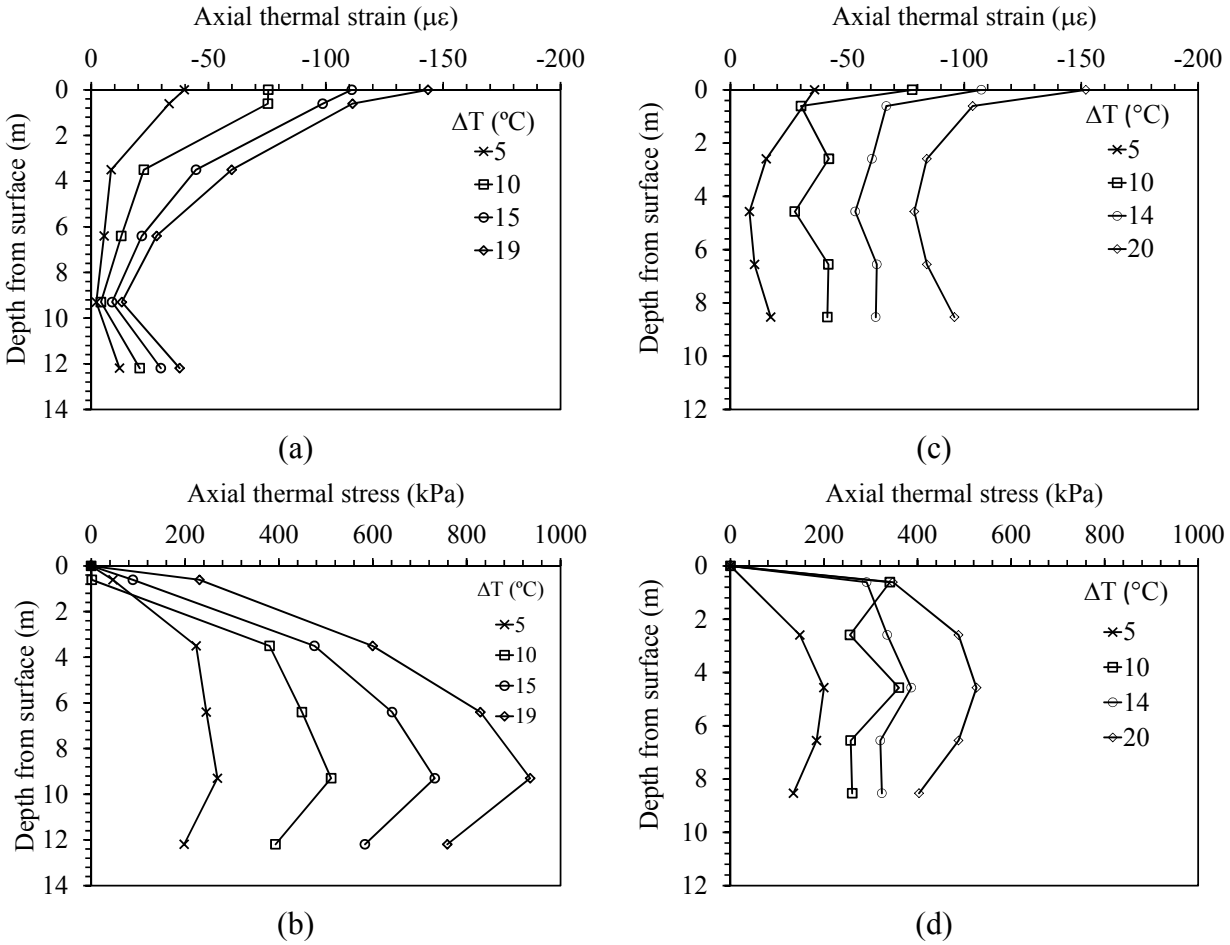

Figure 7.2: Thermal stress and strain profiles at different temperature increments (dimensions in prototype scale): (a) Strain in end-bearing foundation; (a) Stress in end-bearing foundation; (c) Strain in semi-floating foundation; (d) Stress in semi-floating foundation

Evaluation of the thermal strain profiles for the semi-floating foundation in Figure 7.2(c) indicates that the null point is above the center of the foundation. This suggests that the side shear resistance along the foundation provides a stiffer resistance that the soil near the tip of the foundation (Plaseied 2012). The axial thermal stresses in the semi-floating foundation are lower than those in the end-bearing foundation, likely because there is less restraint from the soil and end boundary condition.

7.2 Cyclic Heating and Cooling Effects

The maximum and minimum strain values for the strain gage closest to the null point in either foundation during 4 different cycles of heating-cooling for the end-bearing and semi-floating boundary conditions are shown in Figures 7.3(a) and 7.3(b), respectively. The data for the end-bearing foundation shown in Figure 7.3(a) indicates that a decrease in thermal strain with each cycle is observed, indicating some strain softening occurred. It is also possible that the heating-cooling cycles were applied quickly enough that the soil immediately surrounding the foundation had not completely recovered from the previous cycle when the proceeding cycle began. The cyclic strain data for the semi-floating foundation is shown in Figure 7.3(b), which indicates an increase in thermally induced strains for the same temperature during each cycle. Although the change in strain is small as compared with the end-bearing foundation, the trend is constant and implies a slight amount of strain softening behavior after each cycle of heating and cooling. The changes in axial displacement after heating and cooling cycles are shown in Figures 7.3(c) and 7.3(d) for the end-bearing and semi-floating foundations, respectively. The increasing values of displacement in both figures indicate an increase in expansion after each cycle. However, the magnitude of expansion is relatively minor (less than $1/10^{th}$ of a millimeter).

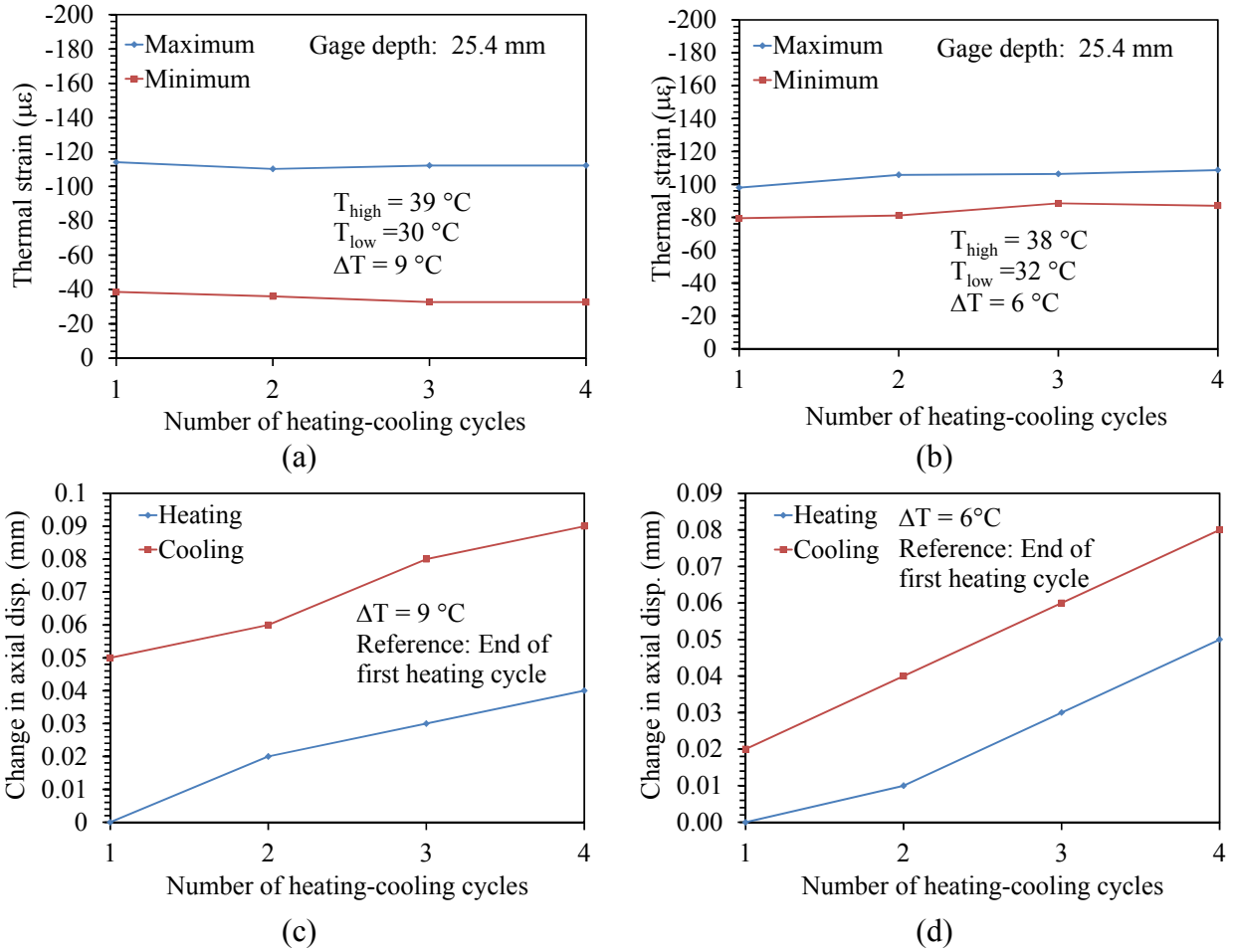

Figure 7.3: Cyclic heating and cooling effects: (a) Change in thermal strains in the end-bearing foundation; (b) Change in thermal strains in the semi-floating foundation; (c) Change in axial displacement in the end-bearing foundation; (d) Change in axial displacement in the semi-floating foundation

One of the potential causes of the change in behavior during cyclic heating and cooling is thermally induced water flow in the soil surrounding the foundation, leading to changes in soil-structure interaction. As heat moves through the foundation into the soil, a vapor gradient establishes, leading to drying of the soil closest to the foundation. This drying leads to changes to suction and corresponding increases in effective stress. An increase in effective stress would lead to a stronger interaction between the soil and foundation. The volumetric water content data obtained from the dielectric probes at varying depths and at a radial distance of 50.8 mm from the foundation for both conditions are shown in Figure 7.4. The initial volumetric water content

for each test is indicative of the placement conditions of the soil, with the potential for some drying of the soil at the depth of the most shallow sensor. In the case of the end-bearing foundation the dielectric sensors all recorded in increase in volumetric water content once foundation started, as shown in Figure 7.4(a) followed by a decrease at the end of the thermal cycles. The sensor at the most shallow depth displayed the response most sensitive to changes in the foundation temperature. Although the bottom two sensors recorded mostly a consistent increase in volumetric water content throughout the thermal cycles, the sensor closest to the ground surface fluctuated with each thermal cycle which implies dynamically changing soil-structure interaction during this part of the test.

Similar behavior was observed for the semi-floating condition in Figure 7.4(b). Although the dielectric sensor nearest the surface for the semi-floating foundation does not react with the same sensitivity to temperature change as in the end-bearing foundation, there are measurable increases and decreases in water content for this test.

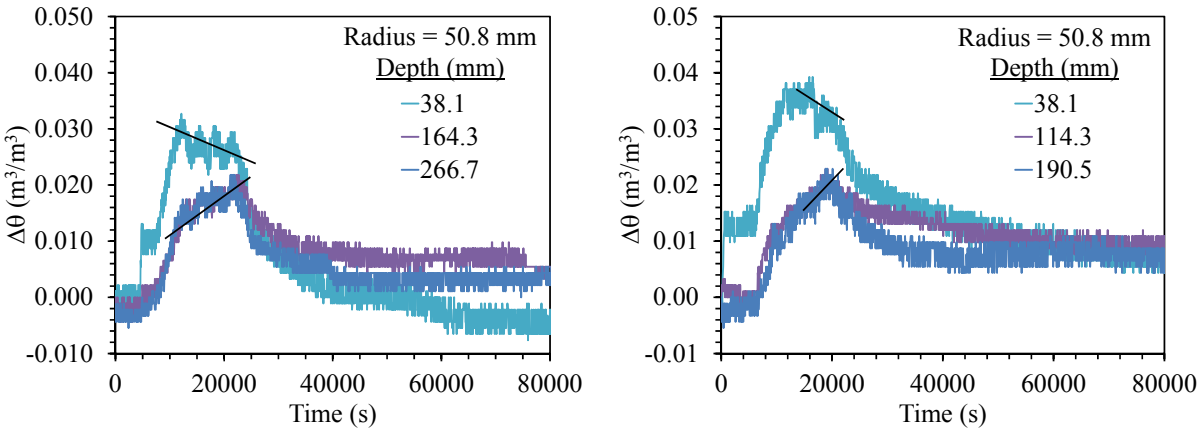

Figure 7.4: Thermally driven water content changes observed using dielectric sensors installed at varying depths (model scale): (a) End-bearing foundation; (b) Semi-floating foundation

Thermally driven water flow in the horizontal direction is presented for both end-bearing and semi-floating foundation in Figures 7.5(a) and 7.5(b), respectively. The results shown at 50.8 mm away from the foundation for each test are the same data points as shown in Figures

7.4(a) and 7.4(b) at the deepest location. For both tests this is the location with the largest change in volumetric water content, as expected. The other two locations for both tests indicate that a change in volumetric water content propagated through the soil surrounding the foundation, although the effect diminished greatly between 50.8 and 139.7 mm from the foundation.

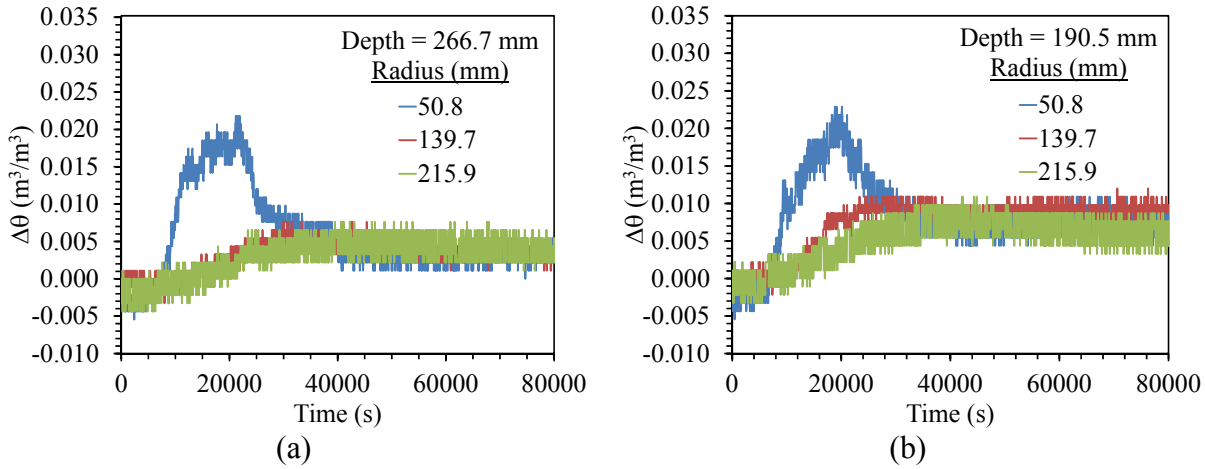

Figure 7.5: Thermally driven water flow collected from dielectric sensors at varying radial distances from foundations: (a) end-bearing foundation; (b) semi-floating foundation

CHAPTER VIII
Conclusions

The strain distributions in the scale-model energy foundations evaluated in this study agree well with strain distribution data collected from full-scale energy foundations. The foundation boundary conditions were found to have a substantial impact on the magnitude of strains measured in the foundations, with a change in strain observed for the end-bearing foundation than for the semi-floating foundation. In addition, the location of the maximum strain was found to depend on the foundation boundary conditions. The maximum strain values were located near the top and bottom of the foundation for the semi-floating foundation and near the top of the foundation for the end-bearing foundation. The maximum stress values were located at the opposite locations from the locations of maximum strain, and reveal the location of the null point. These observations are consistent with predictions from thermo-mechanical soil-structure interaction analyses. Heating and cooling cycles were found to lead to cumulative decreases in compressive strains in both foundations, which can be attributed to thermally induced water flow away from the foundation in the surrounding unsaturated soil. Because the soil dried further upon each cycle of heating and cooling, the corresponding change in soil-foundation friction caused a cumulative change in the thermo-mechanical strains within the foundation, leading to a cumulative movement of the foundation.

The data from this study is presented in terms of strains measured during mechanical loading and temperature changes. An issue which was not resolved at the end of this thesis is the conversion of the measured strain values into thermo-mechanical stresses. Converting the measured strains to stresses is more difficult than simply multiplying the strains measured by the stiffness of the foundation. First of all, the strains induced by applying heat to the foundation are in the form of both physical movement of the foundation as well as internal strains which

develop as a function of the resistance to movement due to the surrounding soil mass. In addition, the recorded data from the strain gages can be affected by thermal changes in a manner that is often not considered during traditional strain measurements. Much of this uncertainty can be corrected, but the compressive strains measured during heating for both this study and full-scale test data presented in previous literature suggests that further centrifuge modeling research is needed to fully interpret the thermal strains measured in energy foundations.

REFERENCES

Adam, D. and Markiewicz, R. (2009). "Energy from earth-coupled structures, foundations, tunnels and sewers." Géotechnique. 59(3), 229–236.

Aiban, S.A. and Znidarcic, D., (1989). "Evaluation of the flow pump and constant head techniques for permeability measurements." Géotechnique 39, 655-666.

Baldi, G., Hueckel, T., and Pelegrini, R. (1988). "Thermal volume changes of the mineral-water system in low-porosity clay soils." Canadian Geotechnical Journal. (25): 807-825.

Boennec, O. (2008). "Shall ground energy systems." Proceedings of the Institution of Civil Engineers. (161), 57-61.

Bourne-Webb, P.J., Amatya, B., Soga, K., Amis, T., Davidson, C. and Payne, P. (2009). "Energy pile test at Lambeth College, London: Geotechnical and thermodynamic aspects of pile response to heat cycles." Geotechnique. 59(3), 237–248.

Brandl, H. (2006). "Energy foundations and other thermo-active ground structures." Géotechnique. 56(2), 81-122.

Campbell, G.S., Callissendorff, G.S., and Williams, J.H. (1991). "Probe for measuring soil specific heat using a heat pulse method." Soil Sci. Soc. Am. J. 55, 291-393

Cekerevac, C. and Laloui, L. (2004). "Experimental study of thermal effects on the mechanical behavior of a clay." International Journal for Numerical Analytical Methods Geomechanics. 28: 209–228.

Choi, J.H., and Chen, R.H.L. (2005). "Design of continuously reinforced concrete pavements using glass fiber reinforced polymer rebars." Publication No. FHWA-HRT-05-081. Washington, D.C.

Coccia, C.J.R. and McCartney, J.S. (2012). "A Thermo-hydro-mechanical true triaxial cell for evaluation of the impact of anisotropy on thermally-induced volume changes in soils." ASTM Geotechnical Testing Journal. 35(2). 11pg.

Cui, Y. J., Sultan, N. and Delage, P. (2000). "A thermomechanical model for clays." Canadian Geotechnical Journal. 37, No. 3, 607–620.

El Tawati, A.I. (2010). Impact of the Rate of Heating on the Thermal Consolidation of Compacted Silt. M.S. Thesis. University of Colorado Boulder.

Energy Information Agency (EIA). (2008). Annual Energy Review. Report No. DOE/EIA-0384(2008).

Ennigkeit, A. and Katzenbach, R. (2001). "The double use of piles as foundation and heat exchanging elements." Proceedings 15th International Conference on Soil Mechanics and Geotechnical Engineering. Istanbul, Turkey. p. 893-896.

Hueckel, T. and Borsetto, M. (1990). Thermoplasticity of saturated soils and shales: Constitutive equations. ASCE Journal of Geotechnical Engineering. 116, 1765-1777.

Kaltreider, C. (2011). Numerical Modeling of Heat Transfer in Thermo-Active Foundations. MS Project. University of Colorado Boulder.

Ko, H.Y. (1988). "Summary of the state-of-the-art in centrifuge model testing." Centrifuges in Soil Mechanics. eds. Craig, W., James, R. and Schofield, A. Balkema, Rotterdam, pp. 11-18.

Laloui, L. (2011). "In-situ testing of heat exchanger pile." Geo-Frontiers: Advances in Geotechnical Engineering. Proc. of the Geo-Frontiers 2011 Conference. Dallas, TX. 10 pg.

Laloui, L., Nuth, M., and Vulliet, L. (2006). "Experimental and numerical investigations of the behaviour of a heat exchanger pile." IJNAMG. 30, 763–781.

Laloui, N. and Nuth, M. (2006). “Numerical modeling of some features of heat exchanger pile.” Foundation Analysis and Design: Innovative Methods (GSP 153). ASCE. Reston, VA. pp. 189-195.

McCartney, J.S., LaHaise, D., LaHaise, T., and Rosenberg (2010). “Feasibility of incorporating geothermal heat sinks/sources into deep foundations.” ASCE Geotechnical Special Publication 198: The Art of Foundation Engineering Practice. Feb. 20-24, 2010.

McCartney, J.S. and Rosenberg, J.E. (2011). “Impact of heat exchange on the axial capacity of thermo-active foundations.” GeoFrontiers 2011. Dallas, TX. 10 pg.

Ooka, R., Sekine, K., Mutsumi, Y., Yoshiro, S. SuckHo, H. (2007). “Development of a ground source heat pump system with ground heat exchanger utilizing the cast-in place concrete pile foundations of a building.” EcoStock 2007. 8 pp.

Plaseied, N. (2011). Load-Transfer Analysis of Energy Foundations. M.S. Thesis. University of Colorado Boulder

Reese, L.C. and O’Neill, M. (1988). Drilled Shafts. Pub. FHWA-HI-88-042. USDOT.

Regueiro, R., Wang, W., Stewart, M.A., and McCartney, J.S. (2012). “Coupled thermo-poro-mechanical finite element analysis of a heated single pile centrifuge experiment in saturated silt.” ASCE GeoCongress 2012. Oakland, CA. March 25-29th 2012.

Rosenberg, J.E. (2010). Centrifuge Modeling of Soil Structure Interaction in Thermo-Active Foundation. M.S. Thesis. University of Colorado Boulder

Rouissi, K., Krarti, M., and McCartney, J.S. (2012). “Analysis of thermo-active foundations with U-tube heat exchangers.” ASME Journal of Solar Energy Engineering. In press.

Stewart, M.A. and McCartney, J.S. (2012). “Strain distributions in centrifuge model energy foundation.” GeoCongress 2012. Oakland, CA. March 28-30, 2012. 10 pg.

Wood, C.J., Liu, H. and Riffat, S.B. (2009). "Use of energy piles in a residential building, and effects on ground temperature." Geotechnique. 59(3), 287-290.

Zitz, W. and McCartney, J.S. (2011). "Issues in the installation of energy foundations." 2011 SME Annual Meeting. Denver, CO. March 1-3, 2011. 10 pg.

Appendix A

Thermocouple		Temperature (°C)			Calibration		
		Cold	Ambient	Hot	Slope	Y-Intercept	R^2
Reference		11.00	21.00	40.00			
Ambient		11.11	21.40	40.61	1.02	-0.02	1.00
Inlet		11.31	21.25	40.33	1.00	0.27	1.00
Outlet		11.16	21.18	40.24	1.00	0.13	1.00
Reference		11.00	21.00	40.00			
Foundation	1	11.11	21.22	40.55	1.02	-0.08	1.00
	2	11.14	21.25	40.31	1.01	0.10	1.00
	3	11.19	21.17	40.27	1.00	0.14	1.00
	4	11.21	21.20	41.15	1.03	-0.31	1.00
	5	11.08	21.04	40.09	1.00	0.05	1.00
Reference		11.00	21.00	40.00			
Probe 1	11	10.90	21.25	40.54	1.02	-0.28	1.00
	12	11.23	21.07	40.46	1.01	0.02	1.00
	13	11.25	21.14	40.57	1.01	0.02	1.00
	14	11.56	21.65	40.85	1.01	0.45	1.00
	15	11.30	21.58	41.37	1.04	-0.15	1.00
	16	11.90	21.44	40.98	1.01	0.63	1.00
Reference		12.00	21.50	39.50			
Probe 2	21	11.60	21.70	40.40	1.05	-0.89	1.00
	22	11.25	21.20	40.13	1.05	-1.37	1.00
	23	11.87	21.65	40.24	1.03	-0.52	1.00
	24	11.78	21.28	40.10	1.03	-0.72	1.00
	25	12.34	21.25	40.29	1.02	-0.24	1.00
	26	12.53	21.29	40.34	1.02	-0.04	1.00
Reference		12.50	21.25	39.25			
Probe 3	31	12.43	20.99	39.87	1.03	-0.61	1.00
	32	12.48	21.09	39.62	1.02	-0.35	1.00
	33	12.65	21.12	39.76	1.02	-0.23	1.00
	34	13.10	21.64	40.43	1.02	0.12	1.00
	35	13.07	21.59	40.30	1.02	0.14	1.00
	36	12.95	21.43	40.21	1.02	-0.02	1.00
Reference		13.00	21.50	39.00			
Probe 4	41	13.25	22.18	39.18	0.99	0.53	1.00
	42	13.27	21.99	39.16	0.99	0.46	1.00
	43	13.30	21.52	39.39	1.01	0.09	1.00
	44	13.51	21.61	39.83	1.02	0.08	1.00
	45	13.24	21.16	39.34	1.01	-0.14	1.00
	46	13.73	21.54	39.66	1.00	0.40	1.00